

Electronic Thesis and Dissertation Repository

6-28-2021 2:00 PM

A novel design methodology accounting for ramping and field inhomogeneities in dreMR imaging

Matthew A. McCready, *The University of Western Ontario*

Supervisor: Chronik, Blaine A., *The University of Western Ontario*

A thesis submitted in partial fulfillment of the requirements for the Master of Science degree in Physics

© Matthew A. McCready 2021

Follow this and additional works at: <https://ir.lib.uwo.ca/etd>

Recommended Citation

McCready, Matthew A., "A novel design methodology accounting for ramping and field inhomogeneities in dreMR imaging" (2021). *Electronic Thesis and Dissertation Repository*. 7896.
<https://ir.lib.uwo.ca/etd/7896>

This Dissertation/Thesis is brought to you for free and open access by Scholarship@Western. It has been accepted for inclusion in Electronic Thesis and Dissertation Repository by an authorized administrator of Scholarship@Western. For more information, please contact wlsadmin@uwo.ca.

Abstract

Delta relaxation enhanced magnetic resonance (dreMR) is a field cycled magnetic resonance imaging method for quantitative molecular imaging. DreMR uses an insertable field cycling coil to exploit longitudinal dispersion of contrast agents producing signal proportional to their concentration. Assumptions in the development of dreMR included instantaneous ramping of the insert coil and perfectly homogeneous field shifts. Here we discard these assumptions and show that finite ramping and field inhomogeneities can impair proportionality to agent concentration and produce significant signal from background tissues. To mitigate these effects, a novel dreMR coil design method is developed employing a boundary element method designed layer to the system which corrects field inhomogeneities, maximizing the usable dreMR imaging region. While a dreMR coil has not yet been constructed for use on humans, with these improvements it is expected that human designs will be much more feasible allowing the extension of this method to clinical studies.

Keywords

Magnetic resonance imaging; field-cycling; contrast agent; relaxivity; T1 dispersion; delta relaxation enhanced MRI; Bloch equation simulation; electromagnet design; boundary element method; magnetic field inhomogeneity; finite ramping periods

Summary for Lay Audience

Delta relaxation enhanced magnetic resonance (dreMR or “dreamer”) is an extension of magnetic resonance imaging (MRI) which allows the user to locate target molecules within the imaging subject. By use of an insertable electromagnetic coil and field dependent contrast agents, dreMR is able to produce images with signal proportional to local concentration of these agents. However, this is the idealized case where the coil is able to instantaneously produce a perfectly uniform magnetic field. In reality, this field contains imperfections and takes some finite period of time to produce. In this thesis we revisit the original derivations of dreMR with these parameters accounted for and find that they lead to a loss of proportionality to agent concentration and confound differentiation between background tissues and locations of agent. We discuss the feasibility of mitigating these effects and present an improved design method for dreMR coils which corrects field imperfections. Thus far a dreMR coil has not been constructed for use on humans. However, with these improvements it is expected that human designs will be much more feasible allowing the extension of this method to clinical studies.

Co-Authorship Statement

This thesis contains materials from the as yet unpublished manuscript:

M.A. McCready, W.B. Handler, B.A. Chronik, *An improved homogeneity design method for fast field-cycling coils in molecular MRI*.

As well as the peer-reviewed conference abstract:

M.A. McCready, W.B. Handler, B.A. Chronik, *Measuring induced heating of low-field superconducting system during field-cycling pulse sequences*, Proc. 29th Sci. Meet. Int. Soc. Magn. Reson. Med. (2021) 2483.

A version of the unpublished manuscript appears in Chapter 3, while the conference abstract appears in Appendix B and is reprinted with permission from the International Society of Magnetic Resonance in Medicine. All theoretical and experimental work presented within this thesis was carried out by Matthew McCready, with William Handler supervising and assisting in the experiments of Appendix B. The relaxivity data for T_1 dispersive agents Ablavar, VivoTrax, and Feraheme plotted in Figure 1.2 and used in simulations throughout Chapters 2 and 3 was provided by Tim Scholl and Francisco Martínez Santiesteban. Much of the underlying implementation of the boundary element method used throughout Chapter 3 relied on code developed by William Handler, Chad Harris, Geron Bindseil, and the other members of the xMR research group over the past decade.

Acknowledgements

Thank you to my supervisor Dr. Blaine Chronik for providing me with the freedom and opportunity to pursue this project.

I would like to thank Dr. Will Handler for his invaluable guidance over the last two years. This work has only come to fruition through a great many discussions with Will. Aside from providing me with the knowledge necessary for this thesis, Will has taught me a great deal about how to do proper science and acted as both mentor and supervisor too me.

To my fellow lab mates, thank you for the support and advice you've all provided me with over the course of this degree. I would like to especially thank Eric Lessard for letting me pester him with questions about the boundary element method at the start of this project and about a million other things since then. Amgad Louka, Arjama Halder, Colin Metrow, Diego Martinez, Kieffer Davieau, John Adams, and Eric, you've been an amazingly welcoming and fun group and I can only hope my future labs are half as great.

I would like to also thank Dr. Geron Bindseil and Dr. Chad Harris, who have offered a great deal of advice on this work through our bi-weekly design meetings over the course of the pandemic. These meetings (joined by Will Handler and Eric Lessard) have kept me on track through this chaotic period.

To Dr. Tim Scholl and Dr. Francisco Martínez Santiesteban who provided me with the relaxivity data without which much of the results of this thesis would not be possible; thank you for your time and patience answering my questions about dreMR and contrast agents up to the last minute of this project.

Thank you to the entire xMR research group for providing such a friendly workplace.

Finally, I would like to thank my family without whom I would quite literally not be here, know that everything I have accomplished is thanks to your support. Thank you also to my friends, both those in my field and those who don't know what MRI stands for. In particular, Xin Yue Wang, David Jung, and Sabaszan Jegenathan. Without all of you I would have cracked a month into this pandemic (or cracked more I should say).

Table of Contents

Abstract	ii
Keywords	ii
Summary for Lay Audience	iii
Co-Authorship Statement.....	iv
Acknowledgements.....	v
Table of Contents	vi
List of Tables	x
List of Tables	x
List of Figures	xi
List of Abbreviations	xiii
Chapter 1 Introduction	1
1.1 Introduction to magnetic resonance imaging	1
1.1.1 Magnetization and nuclear magnetic resonance	1
1.1.2 MRI hardware.....	3
1.1.2.1 Main magnet	4
1.1.2.2 Radiofrequency systems	4
1.1.2.3 Gradient systems	5
1.1.2.4 Shim systems	6
1.1.3 Relaxation and the Bloch equations	6
1.1.4 Contrast mechanisms	7
1.2 Introduction to the boundary element method	10
1.2.1 Boundary element method fundamentals	10
1.2.2 Minimum energy shielding.....	13
1.2.3 Wire spacing and field homogeneity control.....	15

1.3 Introduction to delta relaxation enhanced MR	16
1.3.1 The dreMR subtraction image	17
1.3.2 Existing dreMR hardware.....	19
1.4 Thesis overview.....	21
1.5 References	22
Chapter 2 Characterization of magnetic field inhomogeneity and finite ramping period effects in dreMR	28
2.1 Introduction	28
2.1.1 The theory and assumptions of dreMR.....	28
2.1.2 Removing the instantaneous ramping assumption	30
2.1.3 Removing the homogenous field shift assumption.....	31
2.2 Methods.....	32
2.2.1 Analytic finite ramping effects model	32
2.2.2 Analytic field inhomogeneity effects model.....	34
2.2.3 Bloch simulations of finite ramping effects.....	35
2.2.4 Bloch simulations of field inhomogeneity effects	38
2.3 Results	40
2.3.1 Finite Ramping Effects Results	40
2.3.2 Inhomogeneous Field Shift Effects Results.....	42
2.4 Discussion	45
2.4.1 Discussion of Finite Ramping Effects	45
2.4.2 Discussion of Inhomogeneous Field Shift Effects	47
2.5 Conclusions	48
2.6 References	49
Chapter 3 An improved homogeneity design method for dreMR systems.....	52

3.1 Introduction	52
3.2 Methods	54
3.2.1 Design overview	54
3.2.2 Boundary element method.....	55
3.2.3 Improving dreMR homogeneity	56
3.2.4 Evaluation of Selected Designs	59
3.2.5 Image Simulation.....	60
3.3 Results	62
3.3.1 Comparison with previously constructed design.....	62
3.3.2 Explicit control of imaging region.....	71
3.4 Discussion	73
3.5 Conclusions	74
3.6 References	74
Chapter 4 Conclusions and future work.....	78
4.1 Thesis summary.....	78
4.2 Future work	80
4.2.1 Additional post-processing dreMR methods	80
4.2.2 Asymmetric dreMR pulses	81
4.2.3 Extensions to design method	81
4.2.4 Design studies and construction of coils	83
4.3 References	84
Appendices.....	85
A. Derivations of dreMR	85
A.1. Derivation of dreMR with finite ramping periods.....	85
A.2. Derivation of dreMR with inhomogeneous field shifts.....	89

B. Operation of dreMR insert in compact low-field system.....	90
B.1. Measuring induced heating of low-field superconducting system during field-cycling pulse sequences	90
C. References for appendices.....	94
Curriculum Vitae	96

List of Tables

Table 2.1. Tissue longitudinal relaxation times	36
Table 3.1. Comparison of coil designs with new and old method	65
Table B.1. dreMR pulse sequence parameters	92

List of Figures

Figure 1.1. Precession about external magnetic field.	3
Figure 1.2. Relaxivity for T_1 dispersive contrast agents	9
Figure 1.3. Stages of the BEM.....	10
Figure 1.4. Pulse sequence for dreMR subtraction image	18
Figure 1.5. The dreMR insert coil.....	20
Figure 2.1. Finite ramping time simulation grid	37
Figure 2.2. dreMR pulses for finite ramping time grid simulations	38
Figure 2.3. Inhomogeneous field shift simulation grid	39
Figure 2.4. Finite ramp time grid simulations at $B_0 = 1.3T$	40
Figure 2.5. Finite ramp time grid simulation for Ablavar at $B_0 = 1.3T$	41
Figure 2.6. Finite ramp time simulation and model comparisons.....	42
Figure 2.7. Negative inhomogeneity grid simulations at $B_0 = 1.3T$	43
Figure 2.8. Positive inhomogeneity grid simulations at $B_0 = 1.3T$	43
Figure 2.9. Inhomogeneous field shift grid simulations for Ablavar at $B_0 = 0.3T$	44
Figure 2.10. Inhomogeneous field shift simulation and model comparisons	45
Figure 3.1. Cross sections of previous and new dreMR coil designs	55
Figure 3.2. Design flow chart for the improved homogeneity method.....	59
Figure 3.3. Domain for simulated dreMR subtraction imaging	61
Figure 3.4. Inhomogeneity contour maps for previous and new designs.....	63
Figure 3.5. Comparison of shielding in previous and new designs	64
Figure 3.6. Image error with coil designs on homogenous domain.....	66
Figure 3.7. Image error with coil designs on VivoTrax domain at $B_0 = 0.5T$	67

Figure 3.8. Image error with coil designs on Ablavar domain at $B_0 = 0.3\text{T}$	69
Figure 3.9. Image error with coil designs on Ablavar domain at $B_0 = 0.5\text{T}$	70
Figure 3.10. Inhomogeneity contour maps for ROI-shifted design	72
Figure 4.1. Gradient assisted pre-polarization dreMR pulse sequence	83
Figure B.1. Induced heating experimental set up.....	93
Figure B.2. Temperature measurements of main magnet and dreMR coil	93
Figure B.3. dreMR insert fields at main magnet bore radius	94

List of Abbreviations

B_0	Static main field strength
BEM	Boundary element method
CSF	Cerebral spinal fluid
dreMR	Delta relaxation enhanced magnetic resonance
FFC	Fast field cycling
GM	Grey matter
H	Inhomogeneity
M_0	Equilibrium magnetization
MRI	Magnetic resonance imaging
NMR	Nuclear magnetic resonance
ODE	Ordinary differential equation
PET	Positron emission tomography
PNS	Peripheral nerve stimulation
R_1	Longitudinal relaxation rate
r_1	Longitudinal relaxivity
RF	Radiofrequency
ROI	Region of interest
RSA	Rabbit serum albumin
SNR	Signal to noise ratio
SPION	Superparamagnetic iron oxide nanoparticle
SSE	Sum squared error
T_1	Longitudinal relaxation time constant
T_2	Transverse relaxation time constant
WM	White matter
ΔB	Magnetic field shift
η	Field efficiency
ξ	Slew rate

Chapter 1

Introduction

This work focuses on the improvement of a quantitative molecular imaging modality developed by previous group members and referred to as “delta relaxation enhanced magnetic resonance” (dreMR or “dreamer”). In this chapter we will introduce the necessary background in dreMR’s parent imaging modality magnetic resonance imaging (MRI), the boundary element method (BEM) used in the improvement of dreMR hardware, and introduce the theory and hardware that enables dreMR itself.

1.1 Introduction to magnetic resonance imaging

MRI is an imaging modality relying on the principles of nuclear magnetic resonance (NMR) and the ability to produce a net magnetization within an imaging subject. This section will focus on the underlying physical phenomena that enable MRI and how they are manipulated using hardware and signal processing to produce three-dimensional images within the body. For an in-depth understanding of MRI, the reader is recommended to the textbooks “Magnetic Resonance Imaging: Physical Principles and Sequence Design” by E.M. Haacke et al [1] or “Principles of Magnetic Resonance Imaging” by D.G. Nishimura [2] for a more complete description.

1.1.1 Magnetization and nuclear magnetic resonance

All particles with non-zero spin numbers have an intrinsic angular momentum. If these particles also carry an electric charge, then they will have an intrinsic magnetic dipole moment μ . When subjected to a sufficiently strong external magnetic field, this moment will tend to align parallel to the field, in order to minimize its potential energy. Any subject to be imaged by MRI will contain large quantities of these magnetic moments. While a given moment may not fully reach alignment with the external field due to thermal energy, the aggregate of these moments produce a net magnetization, $\mathbf{M}(\mathbf{r}, t)$, in the direction of the field. This magnetization at thermal equilibrium, \mathbf{M}_0 , for a given particle is proportional to

particle number density, ρ , the external magnetic field, \mathbf{B}_0 , the square of the particle's gyromagnetic ratio, γ , and inversely proportional to the average thermal energy, kT , where k is Boltzmann's constant and T is the absolute temperature.

$$\mathbf{M}_0 = \frac{\rho\gamma^2\hbar^2\mathbf{B}_0}{4kT} \quad 1.1$$

This relation is referred to as Curie's Law, where \hbar is Plank's constant divided by 2π . This equilibrium magnetization is one of two key physical phenomena which make MRI possible.

The second physical mechanism which MRI exploits is nuclear magnetic resonance (NMR). When a magnetic moment is subjected to an external magnetic field, that field applies a torque to the moment normal to their plane. This torque causes the spin to precess about the external field vector (**Figure 1.1**). The frequency at which the spins precess is called the Larmor frequency and is determined by the magnitude of the external magnetic field, B_0 , and the gyromagnetic ratio of the particle.

$$f = \frac{\gamma}{2\pi}B_0 \quad 1.2$$

The net magnetization of a given type of particle will also then precess at this frequency. As we will see, this frequency is important for the detection of signal from the sample being imaged, so it is necessary to determine what type of particle we want to detect. Hydrogen nuclei (protons) are highly abundant in the human body and are the standard choice to image for MRI. Hydrogen has a gyromagnetic ratio such that $\gamma/2\pi = 42.577$ MHz/T resulting in Larmor frequencies in the radiofrequency (RF) range for typical MRI field strengths of 1.0 – 7.0T.

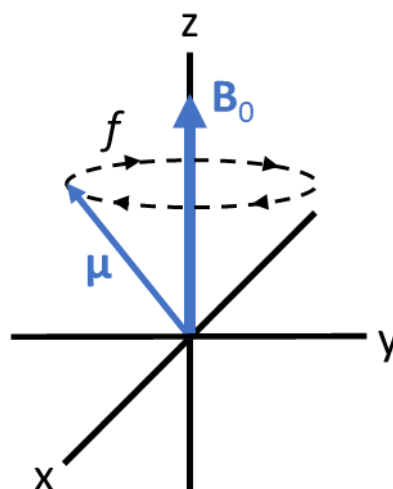


Figure 1.1. Precession of the magnetic moment μ about the external magnetic field \mathbf{B}_0 at the Larmor frequency f .

For this detectable precession to occur, the magnetization needs to be out of alignment from the external field by some angle. By applying a circularly polarized RF magnetic pulse at the Larmor frequency, the magnetization can be rotated out of alignment from the external field with the angle of rotation determined by the pulse strength and duration. As the magnetization then precesses about \mathbf{B}_0 , a receive coil oriented perpendicular to the plane will experience a time varying magnetic flux, inducing an electromotive force according to Faraday's Law of induction. This process of exciting spins with a resonant RF pulse and detecting precession with a receive coil is referred to as NMR. While NMR can be used for spectroscopy purposes, it is not on its own an imaging modality and offers no spatial information about the source of the signal.

1.1.2 MRI hardware

Exploiting net magnetization and NMR to enable imaging in a sample requires a complex system with many components. Here we will explore the subsystems which account for the three main fields used in MRI. While this thesis does not place particular focus on some of these systems, they will be mentioned throughout, and the reader will benefit from some brief background.

1.1.2.1 Main magnet

Responsible for providing a strong static external magnetic field (\mathbf{B}_0) to the imaging subject, the main magnet polarizes the subject to achieve a net magnetization and provides the external field about which the spins precess. The main magnet typically consists of cylindrically wound elements of wire cooled, often cryogenically by liquid helium, to superconducting conditions.

The field produced is the strongest of the fields within an MRI commonly with a field strength of 1.5T or 3.0T. Some high-field scanners achieve strengths of 7.0T to greater than 10T as the signal-to-noise ratio (SNR) increases with field strength. While high field scanners provide the benefit of improved SNR, the field strength also sets the bulk of the system's cost with scanners running at around \$1M per tesla [3]. There is now a movement towards improving low-field scanners as they offer lower price tags, reduced safety concerns, reduced inhomogeneity effects, less acoustic noise, and less stringent siting requirements allowing for point-of-care scanner designs [4–8]. Low-field scanners are commonly cryogen-free and require shorter cooling and ramping periods. This makes them ideal for regions where power grids are unstable, and prolonged power outages would cause sudden increase in temperature leading to the magnet becoming resistive in a process called a quench. These quenches lose hundreds of thousands of dollars in liquid helium from cryogenic systems, and result in far more down time for mid to high-field scanners than low-field.

1.1.2.2 Radiofrequency systems

The RF system refers to the transmit and receive RF coils for the scanner. These coils apply the resonant RF magnetic pulse (\mathbf{B}_1) to excite the spins, tipping the magnetization out of alignment with the main magnetic field, and receive the MR signal through an induced EMF respectively. These functions can also be carried out by the same coil with some designs. The RF coils form an LC or 'resonant' circuit, with capacitance chosen to tune the coil to the necessary Larmor frequency, making RF coils specific to the nucleus you wish to image and the \mathbf{B}_0 field strength. RF coils produce the lowest strength fields on the order

of μT and are the innermost piece of MRI hardware, placed as close to the subject as possible to maximize SNR.

1.1.2.3 Gradient systems

The hardware discussed thus far enables NMR to be performed; the main magnet polarizes the subject and provides the external field for the spins to precess about, and the RF coils excite the magnetization from alignment and detect the NMR signal. The gradient coils now provide the spatial encoding required to move from NMR spectroscopy to MRI. The gradient fields (\mathbf{G}_x , \mathbf{G}_y , \mathbf{G}_z) are oriented in the z direction and made to vary in strength linearly with position. That is:

$$\mathbf{G}_x = \frac{\partial \mathbf{B}_z}{\partial x} \quad 1.3$$

$$\mathbf{G}_y = \frac{\partial \mathbf{B}_z}{\partial y} \quad 1.4$$

$$\mathbf{G}_z = \frac{\partial \mathbf{B}_z}{\partial z} \quad 1.5$$

These fields are produced by separate coils within the gradient subsystem and are dynamically controlled, with typical field strengths on the order of mT.

A typical MRI pulse sequence will apply one gradient field during RF excitation, one during the relaxation period (see section 1.1.3), and one during the acquisition period. The gradient applied during excitation is referred to as the “slice-select” gradient and varies the external field strength for slices across the subject. This way when the RF pulse is applied, the frequency will only be resonant for one slice thus exciting that single slice from alignment. During relaxation a “phase-encode” gradient will be applied to change the Larmor frequency in lines across the slice. When this gradient pulse ends, the local magnetizations will have spatially dependent phases. Finally, during acquisition, the “frequency-encode” gradient will be applied. This gradient will again vary the Larmor frequency across lines perpendicular to the phase encoding as the receive RF coil detects the signal. The resulting signal can then be reconstructed into a 2D image by use of inverse

Fourier transforms, and the process is repeated with a new slice excited to extend to volumetric images.

1.1.2.4 Shim systems

Homogeneity of the main magnetic field is extremely important in MRI as distortions will cause changes in Larmour frequencies of the protons. This in turn creates errors in the spatial encoding of signal and issues with signal reception if the frequency is outside of the RF receive system range. In order to maintain high homogeneity in the region of interest (ROI) “shims” are used to correct the field. Shims can be categorized as passive shims which account for inherent inhomogeneities of the system and environment after installation, or active shims which account for inhomogeneities produced by the imaging subject. Typically, passive shims are ferromagnetic material placed within the bore while active shims are resistive electromagnetic coils.

1.1.3 Relaxation and the Bloch equations

After excitation by an RF pulse, the spins, and therefore net magnetization, will begin to realign with the main field through a process called relaxation. Relaxation is categorized by two main mechanisms; longitudinal relaxation which occurs parallel to \mathbf{B}_0 and transverse relaxation which occurs perpendicular to \mathbf{B}_0 . The longitudinal or “spin-lattice” relaxation occurs due to interactions between the spins and the lattice of neighboring atoms. As parallel alignment of the magnetic moments with the external field minimizes potential energy, the excited spins will transfer quanta of energy with nearby atoms and thus regrow the longitudinal component of magnetization to M_0 . This relaxation is characterized by the time constant T_1 or inversely the relaxation rate R_1 which are specific to the tissue or material.

The transverse or “spin-spin” relaxation occurs due to local field inhomogeneities produced by a combination of neighboring atoms and the inhomogeneity of external fields. These local inhomogeneities mean that the spins experience slight variation in field strength and therefore Larmor frequency, causing dephasing. This loss of coherent phase results in a

decay of transverse magnetization towards the equilibrium value of zero. This relaxation is characterized by the time constant T_2 or inversely the relaxation rate R_2 which are specific to the tissue or material.

The phenomena of precession, longitudinal, and transverse relaxation give rise to the empirical Bloch equation (Eq. (1.6)) describing the behavior of magnetization in the presence of a magnetic field.

$$\frac{d\mathbf{M}}{dt} = \gamma\mathbf{M} \times \mathbf{B}_{ext} + \frac{1}{T_1}(M_0 - M_z)\hat{\mathbf{e}}_z - \frac{1}{T_2}\mathbf{M}_\perp \quad 1.6$$

Where \mathbf{M}_\perp refers to the transverse magnetization and it is assumed that relaxation occurs for a field directed along the z-axis. For the relaxation period where the only external field is the static main field, $\mathbf{B}_{ext} = B_0\hat{\mathbf{e}}_z$, the vector component solutions to this differential equation become:

$$M_x(t) = e^{-t/T_2}(M_x(0) \cos \omega_0 t + M_y(0) \sin \omega_0 t) \quad 1.7$$

$$M_y(t) = e^{-t/T_2}(M_y(0) \cos \omega_0 t - M_x(0) \sin \omega_0 t) \quad 1.8$$

$$M_z(t) = M_z(0)e^{-t/T_1} + M_0(1 - e^{-t/T_1}) \quad 1.9$$

The last of these equations describes the relaxation of longitudinal magnetization towards the equilibrium value M_0 and will be used extensively in the following chapter. The transverse magnetization is detected by the RF receive system while the longitudinal is not. As we will see, transverse relaxation is of little importance for dreMR imaging and will not be discussed in further detail.

1.1.4 Contrast mechanisms

While we have discussed the mechanisms by which a signal is obtained and an image formed, we have not yet described the appearance of, or information held in such images. This is determined by the choices of acquisition or “echo” time (T_E), and the time between repeated pulse sequences or “repetition” time (T_R), relative to the values of T_1 and T_2 . Three standard forms of contrast exist in MRI determined solely by these choices; proton density, T_1 weighted, and T_2 weighted.

Proton density images seek to image local values of equilibrium magnetization, which is proportional to proton density (Eq (1.1)). This is accomplished with a short T_E relative to both T_1 and T_2 , and a T_R far greater than T_1 and T_2 . This allows the magnetization to recover fully to its equilibrium value M_0 after each pulse sequence and acquires the image before significant relaxation can occur. T_2 weighting can be achieved with a T_R far greater than T_1 to allow full longitudinal relaxation between sequences, and a T_E on the order of T_2 to allow some transverse relaxation before acquisition. T_1 weighting uses a T_R on the order of T_1 to allow partial longitudinal relaxation between sequences, and a T_E far shorter than T_2 to prevent any transverse relaxation before acquisition.

Additional forms of contrast can be obtained by use of contrast agents. These agents, when introduced into the subject, can be used to enhance contrast between normal tissue and a target or diseased tissue by shortening T_1 and T_2 relaxation times of surrounding hydrogen nuclei. Superparamagnetic iron oxide nanoparticles (SPIONs) are typically T_2 shortening agents which decrease local signal intensity [9,10]. Paramagnetic gadolinium chelates are often T_1 shortening agents which increase local signal intensity in T_1 -weighted images [9,10]. The chelate in these agents, which is primarily used to reduce toxicity of the Gd, can be modified to target specific molecules for binding [10]. The ability to locate such agents can facilitate molecular imaging and can be used to evaluate disease, to inform and monitor treatment, and to assess response.

When discussing the effect of contrast agents on tissue relaxation, it is convenient to speak in terms of relaxation rates R . The effect an agent has on this rate will be proportional to its concentration, with the proportionality coefficient termed the “relaxivity” (r) of the agent [11].

$$R_{total} = R_{tissue} + r[CA] \quad 1.10$$

Where $[CA]$ refers to the contrast agent concentration. The relaxivity of some agents can be enhanced when bound to a target molecule to produce additional contrast between bound and unbound agent. Some agents will also exhibit longitudinal relaxivity (r_1) with strong field dependence. This dependence of relaxation rates or time constants on field strength is referred to as a “dispersion relation”. Longitudinal dispersion can be exploited to provide an additional form of contrast between dispersive and non-dispersive agents or tissues.

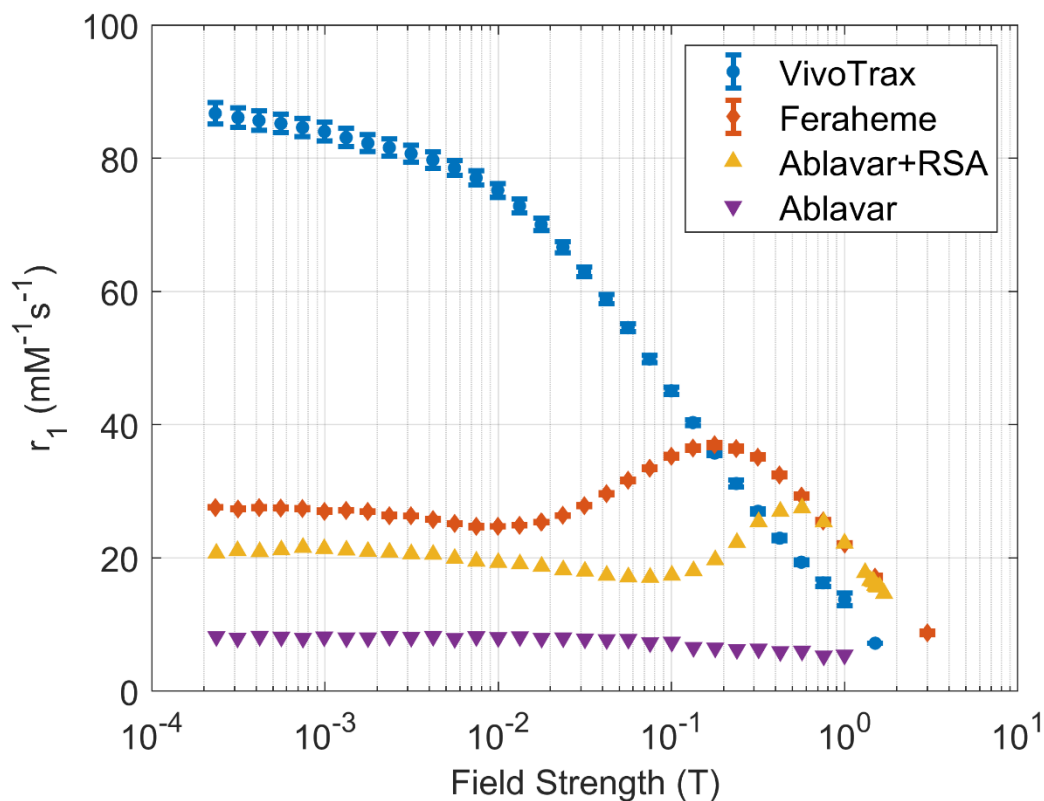


Figure 1.2. Relaxivity as a function of field strength for T_1 dispersive contrast agents VivoTrax, Feraheme, Ablavar bound to rabbit serum albumin (RSA), and unbound Ablavar. Data supplied by Dr. Tim Scholl at Robarts Research Institute.

In this thesis we will focus on two types of dispersive agents; SPIONs and Gd(III) chelates. The SPIONs ferumoxytol (FerahemeTM, AMAG Pharmaceuticals) and ferucarbotran (VivoTraxTM, Magnetic Insight Inc, Alameda, CA) are blood pool agents which are taken up by macrophages and carried to locations of inflammation such as tumors and infections [12–14]. These agents exhibit strong T_1 dispersion as can be seen in **Figure 1.2**, particularly at low field strengths. Some Gd(III) chelates such as gadofosveset trisodium (AblavarTM, Lantheus Medical Imaging, Inc. N. Billerica, MA) exhibit strong dispersion relations only when bound to the target molecule [15,16] (Figure 1.2). Ablavar is also a blood pool agent, but rather than being uptaken by macrophages it binds to the protein serum albumin within blood. These are called “activateable MR probes” and can be exploited with a field-cycling coil to produce highly specific molecular images. One method for producing longitudinal dispersion contrast in images is dreMR, the improvement of which will be the focus of this thesis.

1.2 Introduction to the boundary element method

The BEM is a finite element method which is used to design electromagnets of arbitrary surface geometry with specific properties [17–19]. The BEM solution gives current densities constrained to the given surfaces which produce a desired field in some volume, and can conform to minimum power deposition, inductance, or force and torque requirements. This current density can then be approximated with a finite distribution of discretized current elements, or a “wire-pattern” which is constructed to produce the physical coil. This method will be used extensively in Chapter 3 of this thesis to improve the design of dreMR coils. For an in-depth explanation of the underlying math for the BEM, our group’s implementation, and its variety of applications, the reader is recommended to the PhD thesis “Optimization of a boundary element approach to electromagnet design with application to a host of current problems in magnetic resonance imaging” by C.T. Harris [20].

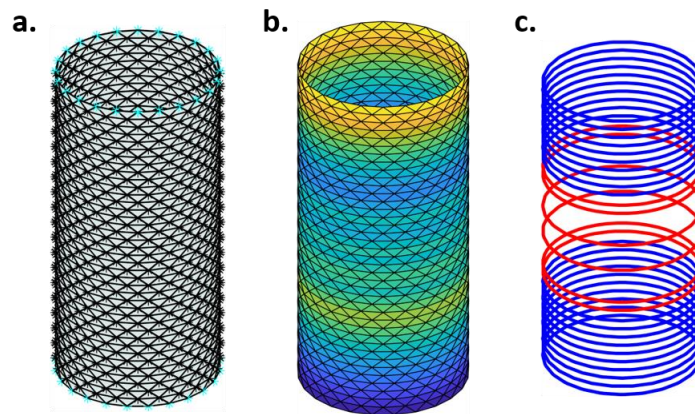


Figure 1.3. Stages of the BEM. **(a)** The user supplied surface mesh where edge nodes are denoted in blue, **(b)** the stream function solution on the surface, **(c)** the resulting wire pattern where red and blue windings represent positive and negative current flow with respect to the x-axis.

1.2.1 Boundary element method fundamentals

The BEM is a finite element method and so begins with the discretization of the problem’s surface geometry into a mesh of elements (**Figure 1.3 (a)**). For the implementation discussed here these elements are triangular. As the BEM seeks to find a current density

producing the desired field, the current density ($\mathbf{J}(\mathbf{r})$) must also be discretized with the problem domain. It is convenient to define a scalar stream function ($\psi(\mathbf{r})$) to solve for with this method and from which $\mathbf{J}(\mathbf{r})$ can be calculated via:

$$\mathbf{J}(\mathbf{r}) = \nabla \times [\psi(\mathbf{r})\mathbf{n}(\mathbf{r})] \quad 1.11$$

where $\mathbf{n}(\mathbf{r})$ is the outward directed normal vector to the surface at position \mathbf{r} .

It is standard for finite element methods to solve for specific values at the nodes of the problem mesh and define a set of shape functions to interpolate between such values across mesh elements. Here, a set of linear shape functions, $N_{nk}(\tilde{x}, \tilde{y})$, are used when solving for stream function node values, I_n :

$$\psi(\mathbf{r}) = \sum_{n=1}^N I_n \psi_n(\mathbf{r}) \quad 1.12$$

$$\psi_n(\mathbf{r}) = \begin{cases} N_{nk}(\tilde{x}, \tilde{y}); & \text{for } \mathbf{r} \text{ inside element } k \\ 0; & \text{for } \mathbf{r} \text{ outside element } k \end{cases} \quad 1.13$$

where $\psi_n(\mathbf{r})$ are the set of basis functions formed by the linear shape functions, and (\tilde{x}, \tilde{y}) is \mathbf{r} in the local coordinates of element k . The discretization of the stream function leads to the subsequent discretization of the current density:

$$\mathbf{J}(\mathbf{r}) \approx \sum_{n=1}^N I_n \nabla \times [\psi_n(\mathbf{r})\mathbf{n}(\mathbf{r})] = \sum_{n=1}^N I_n \sum_{k=1}^K \frac{\mathbf{e}_{nk}}{2A_k} \quad 1.14$$

where K is the total number of mesh elements, A_k is the area of element k , and \mathbf{e}_{nk} is the edge vector opposite of node n within element k .

By representing $\mathbf{J}(\mathbf{r})$ entirely in terms of the stream function values and mesh geometry any property calculable using current density can be found using the stream function. These can be included in a design functional which will be minimized to obtain the desired stream function. Common properties to design for include field uniformity, power deposition, self-inductance, and force and torque constraints. A simple design functional used extensively in Chapter 3 consists of a term for field uniformity and a term for power deposition.

$$U = \frac{1}{2K} \sum_{k=1}^K [B_z(\mathbf{r}_k) - B_z^{tar}(\mathbf{r}_k)]^2 + \frac{\beta}{2} P \quad 1.15$$

Here, field uniformity is controlled through the first term where the sum of squared errors (SSE) is taken between the field produced by the stream function, $B_z(\mathbf{r}_k)$, and the target field values, $B_z^{tar}(\mathbf{r}_k)$, at a set of K user supplied target field points, \mathbf{r}_k . The second term provides control of power deposition, where P represents the power deposited in the surface by the stream function, and β provides a weighting between the field uniformity and power deposition terms.

Since magnetic field and power deposition can be calculated from current density, the design functional (Eq. (1.15)) can be expressed entirely in terms of the stream function values I_n using (Eq. (1.14)). The field at point \mathbf{r}_k due to the stream function is given to be $B_z(\mathbf{r}_k) = I_n c_n(\mathbf{r}_k)$ where $c_n(\mathbf{r}_k)$ is the field matrix defined in [18] for the z-component of the magnetic field at point \mathbf{r}_k . The power deposited in the surface is determined by the stream function values and the resistance matrix of the mesh surface, R_{nm} , as defined in [18]. As a result of these substitutions the design functional (Eq. (1.15)) becomes:

$$U = \frac{1}{2K} \sum_{k=1}^K [I_n c_n(\mathbf{r}_k) - B_z^{tar}(\mathbf{r}_k)]^2 + \frac{\beta}{2} I_n I_m R_{nm} \quad 1.16$$

To ensure closed shape designs will be produced, the stream function values for all nodes of a given edge (**Figure 1.3 (a)**) are constrained to have the same value. This is accomplished by condensing the field and resistance matrices such that the summation of each edge node row for each edge is reduced to a single entry in a new column, and the summation of each edge node column for each edge is reduced to a single entry in a new row. A more detailed description of the condensing process can be found in Appendix A.10.1 of [20].

Minimizing the design functional for I_n will result in the stream function which minimizes the SSE with the desired field values and minimizes power deposition. After taking the derivative of (Eq. (1.16)) with respect to I_n and equating to zero, the resulting linear system of equations is solved to find the stream function values:

$$I_n = \left[\frac{1}{K} c_{nk} c_{mk} + \beta R_{nm} \right]^{-1} \frac{1}{K} c_{nk} B_k^{tar} \quad 1.17$$

where the subscript k refers to evaluation at the target point \mathbf{r}_k , and the exponent -1 implies matrix inversion rather than a division.

When the stream function node values are obtained, the solution (**Figure 1.3 (b)**) is contoured over the surface to obtain a discretized wire pattern (**Figure 1.3 (c)**) approximating the current density [17,19]. Where the stream function has a steeper gradient, these wires will be more densely packed, increasing current density as can be expected from their relation (Eq. (1.11)). Choosing a constant value for contour spacing ensures that running the same current through all resulting wires will produce the approximation to the desired field.

1.2.2 Minimum energy shielding

Any electromagnetic coil which is pulsed on and off will have a time dependent magnetic field (dB/dt). While the fields inside these coils are useful for imaging, strong fields are also produced outside and can interact with other system components. In the case of the time varying field, the coil will produce a time varying flux through any conductors nearby, inducing eddy currents by Faraday's law of induction. These eddy currents can lead to forces and torques acting upon the MRI systems leading to serious safety issues, or joule heating of temperature sensitive systems such as the cryogenic main magnet. It is therefore desirable to include in such coils a shielding layer at an outer radius which mitigates the outside field.

One design method for shields which employs the BEM is the minimum energy method [21]. A minimum energy shield works by supplying an additional wire pattern at a radius outside the primary coil, which is designed to minimize the total magnetic energy of the system. The shield surface is meshed into triangular elements along with the primary, and its stream function values coupled with those of the primary. The total magnetic energy functional introduced for the shield is given by:

$$E = \frac{1}{2} I_{pn} I_{pm} L_{pnm} + \frac{1}{2} I_{sq} I_{sk} L_{sqk} + I_{pn} I_{sk} M_{psnk} \quad 1.18$$

Where the non-italicized “p” and “s” subscripts indicate relation to primary and shield surfaces respectively. The first two of these terms represent the magnetic energy stored by the primary and shield coils with the self inductance matrices L_{nm} described in [18]. The final term gives the magnetic energy stored by the interaction of the two coils with the mutual inductance matrix M_{psnk} [21].

The shield desired will minimize the total magnetic energy of the system, and therefore can be found by minimizing the given functional (Eq. (1.18)) for the shield stream function values I_{sq} . After taking the derivative and equating to zero, the resulting linear set of equations can be solved to give:

$$I_{sq} = -[L_{sqk}]^{-1} M_{psnk} I_{pn} \quad 1.19$$

$$I_{sq} = D_{psnk} I_{pn} \quad 1.20$$

Where the matrix D_{psnk} is used for simplicity of notation in the following equations. This relation can be used to determine the shield stream function for a completed primary solution, or can be coupled with the primary calculation by inclusion in its design functional (Eq. (1.16)) giving:

$$U = \frac{1}{2K} \sum_{k=1}^K [I_{pn} c_{pn}(\mathbf{r}_k) + I_{sq} c_{sq}(\mathbf{r}_k) - B_z^{tar}(\mathbf{r}_k)]^2 + \frac{\beta}{2} [I_{pn} I_{pm} R_{pnm} + I_{sq} I_{sv} R_{sqv}] \quad 1.21$$

$$U = \frac{1}{2K} \sum_{k=1}^K [I_{pn} \tilde{c}_{pn}(\mathbf{r}_k) - B_z^{tar}(\mathbf{r}_k)]^2 + \frac{\beta}{2} I_{pn} I_{pm} \tilde{R}_{pnm} \quad 1.22$$

Where $\tilde{c}_{pn}(\mathbf{r}_k) = c_{pn}(\mathbf{r}_k) + D_{psnk} c_{sq}(\mathbf{r}_k)$ and $\tilde{R}_{pnm} = R_{pnm} + D_{psnq} D_{psmv} R_{sqv}$. By minimizing this functional for the primary stream function values, the field produced at the target points by the shield values will also be included and power deposited in the shield minimized. Simultaneously, the shield stream function values minimize the magnetic energy of the system and the field outside the coil. The shield and primary stream functions are then contoured with the same contour spacing, calculated as before.

1.2.3 Wire spacing and field homogeneity control

When designing electromagnetic coils, it is important to consider resistive heating of the magnet. This is determined at the design stage by the resistance of the coil, and therefore the cross-sectional area of the wire used. Thus far the BEM as discussed determines spacing between wires by the gradient of the stream function and the necessary contour spacing [17,19]. In order to simultaneously control the wire spacing and field uniformity of designs an iterative weighting calculation is implemented [22]. To designate a specific wire gauge for use in construction, the stream function must be restricted to have a maximum gradient for the required contour spacing given as:

$$\|\nabla\psi\|_{\max} = \left| \frac{\text{contour spacing}}{\text{maximum wire gauge}} \right| \quad 1.23$$

After calculation of the stream function following the methods of section 1.2.1 and 1.2.2, if the local stream function gradient across any mesh element j is found to exceed the maximum allowable value, the power deposition weights are updated following (Eq. (1.24)) and the stream function recalculated.

$$\beta_j^{i+1} = \beta_j^i \left(\frac{\|\nabla\psi\|_j^i}{\|\nabla\psi\|_{\max}} \right) \quad 1.24$$

Here, $\|\nabla\psi\|_j^i$ refers to the stream function gradient on the j th mesh element and i th iteration, β_j^i is the element's weighting from the previous calculation and β_j^{i+1} is the element's updated weighting for the next iteration. The minimum value of β_j^i is restricted to its initial value and does not decrease if the local element gradient is less than the maximum allowable value.

It is also desirable to further control the field uniformity over a given region, especially as updating wire spacing may worsen uniformity. A maximum allowable error, Err_{\max} , can be implemented with an iterative calculation for another set of weights W_k^i . These are applied to the SSE between stream function field and the desired field at each of the K target points. For the design of a general non-gradient coil, these weights are determined by the percent error between stream function field and the desired field at each point:

$$\text{Err}_k = 100 \times \frac{|B_z(\mathbf{r}_k) - B_z^{\text{tar}}(\mathbf{r}_k)|}{|B_z^{\text{tar}}(\mathbf{r}_k)|} \quad 1.25$$

$$W_k^{i+1} = W_k^i \left(\frac{\text{Err}_k^i}{\text{Err}_{\text{max}}} \right) \quad 1.26$$

Where the minimum value of W_k^i is restricted to 1. With the inclusion of all weights, the design functional (Eq. (1.15)) becomes:

$$U = \frac{1}{2K} \sum_{k=1}^K W_k^i [B_z(\mathbf{r}_k) - B_z^{\text{tar}}(\mathbf{r}_k)]^2 + \frac{\beta_j^i}{2} P \quad 1.27$$

After each iteration if the target field uniformity and wire spacing are not reached the necessary weights are updated and the stream function recalculated. This continues until the desired conditions are achieved or the maximum allowable number of iterations is reached.

1.3 Introduction to delta relaxation enhanced MR

Molecular imaging provides the ability to make *in vivo* measurement of molecular level biological processes. This ability can be used for evaluation of disease, for informing and monitoring treatment, and for assessing response. Currently, positron emission tomography (PET) is highly prevalent in clinical quantitative molecular imaging, with a favourable, high sensitivity [23]. However, PET is often used with other imaging modalities to provide reference anatomy, and carries with it an associated ionizing radiation dose which can be problematic in longitudinal animal studies [24], and should be minimized under the “as low as reasonably achievable” (ALARA) principle of radiation safety.

MRI presents an alternative molecular imaging modality free from ionizing radiation. However, molecular MRI exhibits lower sensitivity than PET [25], and requires use of contrast agent enhancement methods. As described in Section 1.1.4, MRI contrast agents have been developed with the ability to bind to target molecules and increase local MR signal [15,26]. These agents can be used to create molecular images, by subtraction of pre- and post-injection images. However, due to the time between pre- and post-injection

images, as well as the signal enhancement from any accumulation of unbound agent, these images are only qualitative. These limitations can be overcome by introducing a fast field-cycling (FFC) insert magnet to the MRI system.

The dreMR method exploits the properties of T_1 -dispersive contrast agents using an insertable FFC coil to provide images with signal proportional to local concentration of the agent [27]. These images are taken only post-injection and are therefore less prone to motion effects and have a greatly reduced time period between images. Furthermore, when activatable MR probes (see Section 1.1.4) are used dreMR is able to isolate signal proportional to local concentration of bound agent and suppress that of unbound. As dreMR relies only on standard MRI and a FFC coil this modality is free of the ionizing radiation in PET and, as we will see in the following section, inherently obtains images with all the anatomical information of an MRI scan.

1.3.1 The dreMR subtraction image

The most fundamental example of dreMR imaging is by a field compensated subtraction of two T_1 weighted images taken with opposite dreMR polarity. For each image, the magnetization is first tipped into the transverse plane with a 90° RF pulse to zero longitudinal magnetization. The dreMR insert FFC coil then applies a pulse $\pm\Delta B$ to the subject for the period of relaxation. After the magnetization is allowed to relax at the new field strength for some period Δt , the dreMR pulse ends and a second 90° RF pulse tips the new magnetization into the transverse plane where the image is quickly acquired before significant T_2 relaxation can occur.

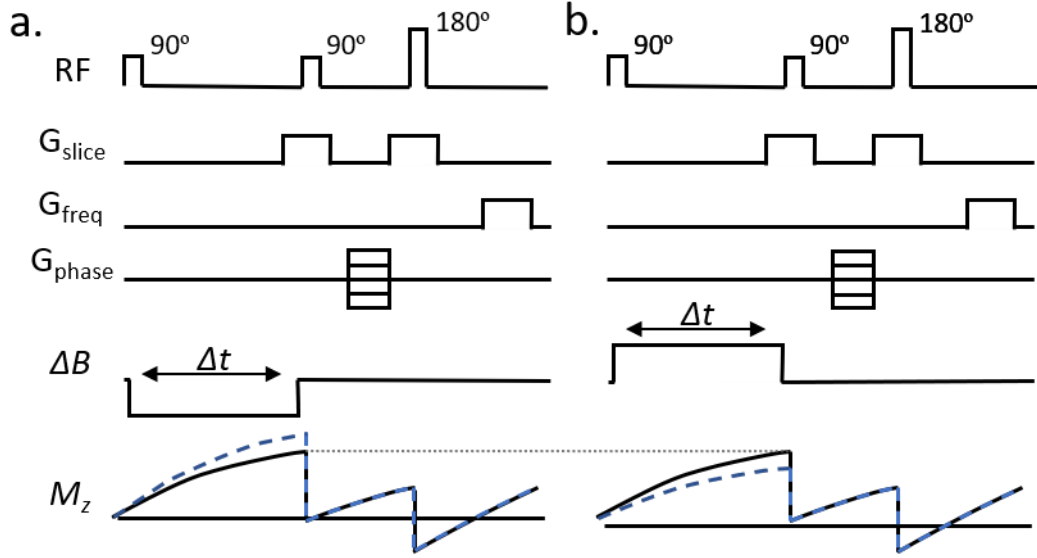


Figure 1.4. Pulse sequence for typical dreMR subtraction image. A $\pm\Delta B$ pulse is applied for a time Δt following a 90° RF pulse to zero longitudinal magnetization. A T_1 weighted spin-echo sequence follows. Longitudinal magnetization M_z is shown for (a) a $-\Delta B$ pulse and (b) a $+\Delta B$ pulse. The solid black line represents non-dispersive signal, while the dashed blue represents dispersive. The grey dotted line shows that non-dispersive signal is the same in both images. Figure adapted from [27].

The first image is taken with the insert subtracting from the main field for a total field $B_0 - \Delta B$, and the second is taken with the insert adding to the main field for a total field $B_0 + \Delta B$. Allowing longitudinal relaxation to occur at different field strengths produces two changes in the magnetization: a scaling of equilibrium magnetization according to Curie's law (Eq. (1.1)) and a change in longitudinal relaxation rate where T_1 dispersive agent is present. The resulting longitudinal magnetization after a dreMR pulse of duration Δt is then from the Bloch equation solution (Eq. (1.9)):

$$M_{z\pm} = M_0 \left(\frac{B_0 \pm \Delta B}{B_0} \right) (1 - e^{-\Delta t R_{1\pm}}) \quad 1.28$$

where M_0 is taken to be the equilibrium magnetization at the main field strength (B_0), and we have substituted the relaxation rate $R_{1\pm}$ for the time constant T_1 with \pm indicating the rate during the $\pm\Delta B$ pulse. Following the second 90° RF pulse and subsequent acquisition, the signal acquired (I_{\pm}) will be proportional to this magnetization (Eq. (1.28)) by some factor k .

The goal of dreMR is to isolate signal due to T_1 -dispersive agent and the dependence of equilibrium magnetization on relaxation field is therefore undesirable. This dependence can be removed through a simple field compensation factor applied to each image signal. When these factors are applied, the results can be differenced, with the only changes remaining being those in R_1 .

$$I_{sub} = \left(\frac{B_0}{B_0 - \Delta B}\right)I_- - \left(\frac{B_0}{B_0 + \Delta B}\right)I_+ \quad 1.29$$

When the signals (Eq. (1.28)) are substituted into the above equation, and the assumptions are made that T_1 -dispersion is linear in the range $B_0 \pm \Delta B$ and that $\Delta t R_1 < 0.2$ and $\Delta t \Delta R_1 < 0.5$ to ignore shading and nonlinear effects, the resulting subtraction gives:

$$I_{sub} \approx 2kM_0\Delta t\Delta R_1 \quad 1.30$$

where ΔR_1 is the change in relaxation rate under the applied pulse $\pm\Delta B$, and k is the proportionality constant between signal and longitudinal magnetization at the end of the dreMR pulse. This result depends only on the change in R_1 and not the value of R_1 itself, meaning signal from any non-dispersive tissue will be suppressed [27]. With the assumption of linear dispersion, the change in relaxation rate can be written as $\Delta B \cdot R'_1$ where R'_1 is the slope of the relaxation rate.

$$I_{sub} \approx 2kM_0\Delta t\Delta B \cdot R'_1 \quad 1.31$$

In the case of dispersive contrast agent, this result is proportional to concentration through the relaxivity definition (Eq. (1.10)). The dreMR subtraction method therefore leads to an image with signal proportional to concentration of dispersive contrast agent, enabling quantitative molecular imaging.

1.3.2 Existing dreMR hardware

As previously mentioned, the necessary field shifts for dreMR to be performed are enabled by a fast-field-cycling coil. This FFC coil is designed as an insertable subsystem to an existing scanner, fitting inside the gradient system and outside the RF system. The

FFC coil needs to supply a strong field shift on the order of hundreds of mT, and ramp on and off rapidly to prevent relaxation at multiple field strengths and allow quick application of RF pulses before and after the dreMR pulse.

To accomplish this, a resistive thick solenoid of greater than one radial windings (NR) is constructed from copper wire with inductance kept to a minimum for the desired field shift. To produce a high strength pulse, a large current must be driven through the coil leading to high power deposition. To combat this, FFC coils used in dreMR have been constructed using hollow copper wire with water coolant pumped through in parallel [28].

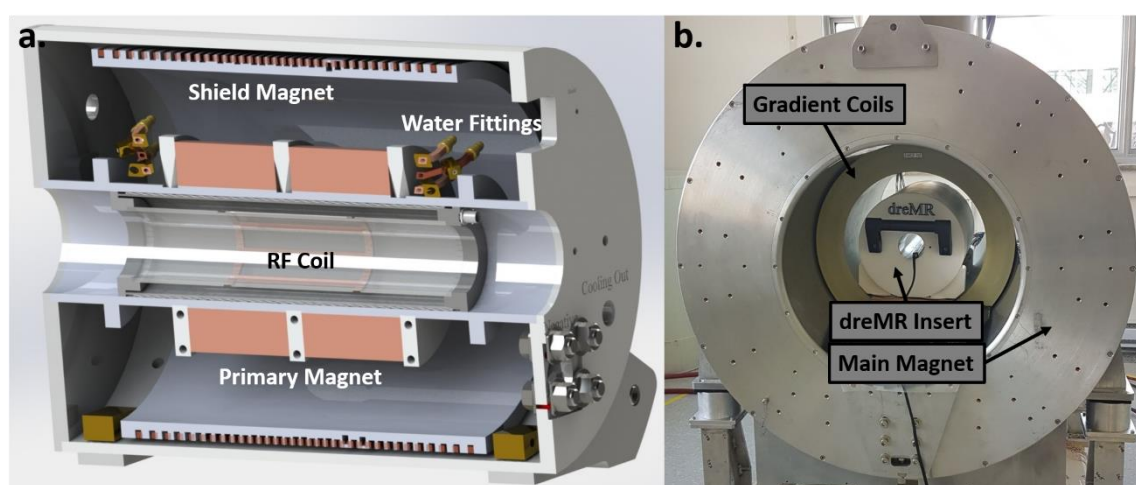


Figure 1.5. The dreMR insert coil (a) schematic showing primary split solenoid, shield layer, and water fittings, with RF birdcage within and (b) the insert positioned within a head-specific gradient and low-field main magnet.

As the field shift is not applied during RF pulses to prevent change to the Larmor frequency, it has previously been believed that the FFC coil does not require high homogeneity [27–30]. Accordingly, previous FFC insert coil designs have placed little importance on homogeneity, and exerted control by use of an axial gap or “split” in the thick solenoid [28,29,31–33]. This method provides only slight increase to field homogeneity at the cost of field efficiency; field shift produced per unit current.

The large and rapid field shifts though desirable within the imaging region will induce eddy currents upon the surfaces of the other scanner subsystems, most notably within the main magnet where joule heating poses the possibility of quenching the system. To minimize the field shift outside the FFC coil, an outer shield layer is included in the

design and connected in series with the primary solenoid [28,29,31–33]. The most recent designs for dreMR [28] have used the retroactive minimum energy shield outlined in section 1.2.2.

However, while shielding may adequately minimize forces and torques and induced heating, some small eddy currents remain. These currents will produce magnetic fields in the imaging region which persist beyond the dreMR pulse duration into the signal excitation and acquisition periods. This can lead to local variations in Larmor frequency, causing off-resonance pulses and dephasing of spins during acquisition. These remaining eddy currents can be compensated for using a dynamic frequency adjustment, or with the addition of a low power Helmholtz coil [28,34].

1.4 Thesis overview

Thus far, dreMR has been demonstrated for quantification and localization of agents [27,30,32], direct protein imaging [35], and measurement of tissue and agent T_1 -dispersion [36], but not yet in a clinical trial. A dreMR system for imaging humans would require a much larger diameter, which poses problems when inserting into the bore of a gradient and main magnet system. Previously, dreMR systems designed for humans included large outer diameters when shielded and exhibited field inhomogeneities on the imaging region of up to 20%, which was deemed acceptable [31,37]. Previous designs did not place great focus on field shift homogeneity as field shifts are not applied during excitation or acquisition [27–30]. It has similarly been argued that finite ramping times, which tend to increase with size of the coil, do not significantly contribute to images and the derivations of dreMR imaging assume the coil ramps to field instantaneously [27]. However, no formal study has been made to determine what effect, if any, such inhomogeneities and finite ramping times would produce in a dreMR image.

In addition to making dreMR viable for human imaging, there is also an interest in performing dreMR in a low-field system. Many of the Gadolinium based T_1 -dispersive contrast agents that dreMR exploits exhibit much higher dispersion at low field strengths than typical clinical values such as 1.5T [38]. It is expected that dreMR images at low field would produce higher contrast than those taken previously at 1.5T. Low field systems are

also inherently attractive for imaging as detailed in section 1.1.2.1. Furthermore, and specific to our group, we have recently acquired and prepared a compact 0.5T cryogen-free superconducting head-specific main magnet which provides easy access for such experiments. However, this magnet has a smaller bore than previously used 1.5T systems, which will further restrict allowable diameter for human dreMR systems and has the potential for stronger interaction with the dreMR insert given the reduced distance between the systems.

This thesis seeks to address the problems facing dreMR for imaging in humans and using low field systems. This is done by characterizing the effects of inhomogeneities and finite ramping times in dreMR imaging and improving dreMR coil design methodology. Chapter 2 will focus on analytic and simulation-based modeling of dreMR imaging with inhomogeneity and finite ramping times accounted for. The objectives are to establish what changes these effects produce in images compared to the ideal cases where they are not present, and to evaluate the significance of such changes. In this chapter a method is developed for determining minimum requirements on field homogeneity and ramping capabilities for a given situation, which should be used to inform future dreMR coil design studies.

In Chapter 3 a method for improved control of field shift inhomogeneity for dreMR coils is presented. This design method adds a close contact in-series shim layer referred to as a “correction coil” to the primary solenoid. This correction coil is formed from specifically placed windings calculated to reduce field inhomogeneities using the BEM and is coupled to calculations for the outer shield. The design method is able to provide a larger usable volume for imaging and control over positioning of said volume. This method is applied to a design of otherwise comparable features to the most recently constructed dreMR coil to see the improvement it is capable of. Both coil designs are used in simulated dreMR images following the methods of Chapter 2 to see how imaging can benefit from the new design method.

1.5 References

- [1] R.W. Brown, Y.-C.N. Cheng, E.M. Haacke, M.R. Thompson, R. Venkatesan,

- Magnetic Resonance Imaging: Physical Principles and Sequence Design, 2nd ed., Wiley Blackwell, Hoboken, NJ, 2014.
- [2] D.G. Nishimura, Principles of Magnetic Resonance Imaging, 1.1, Stanford University Press, Stanford, CA, 2010.
- [3] M. Sarracanie, C.D. Lapierre, N. Salameh, D.E.J. Waddington, T. Witzel, M.S. Rosen, Low-Cost High-Performance MRI, *Sci. Rep.* 5 (2015) 1–9. <https://doi.org/10.1038/srep15177>.
- [4] Y. Lvovsky, P. Jarvis, Superconducting systems for MRI-present solutions and new trends, *IEEE Trans. Appl. Supercond.* 15 (2005) 1317–1325. <https://doi.org/10.1109/TASC.2005.849580>.
- [5] A. Macovski, MRI: A charmed past and an exciting future, *J. Magn. Reson. Imaging.* 30 (2009) 919–923. <https://doi.org/10.1002/jmri.21962>.
- [6] A. Panther, G. Thevathasan, I.R.O. Connell, Y. Yao, C.N. Wiens, A.T. Curtis, G.A. Bindseil, T. Chad, P.J. Beatty, J.A. Stainsby, C.H. Cunningham, B.A. Chronik, C. Piron, A Dedicated Head-Only MRI Scanner for Point-of-Care Imaging, *Proc. Annu. Meet. Int. Soc. Magn. Reson. Med.* (2019) 3679.
- [7] L.L. Wald, P.C. McDaniel, T. Witzel, J.P. Stockmann, C.Z. Cooley, Low-cost and portable MRI, *J. Magn. Reson. Imaging.* 52 (2020) 686–696. <https://doi.org/10.1002/jmri.26942>.
- [8] C.Z. Cooley, P.C. McDaniel, J.P. Stockmann, S.A. Srinivas, S.F. Cauley, M. Śliwiak, C.R. Sappo, C.F. Vaughn, B. Guerin, M.S. Rosen, M.H. Lev, L.L. Wald, A portable scanner for magnetic resonance imaging of the brain, *Nat. Biomed. Eng.* 5 (2021) 229–239. <https://doi.org/10.1038/s41551-020-00641-5>.
- [9] P. Hermann, J. Kotek, V. Kubíček, I. Lukeš, Gadolinium(III) complexes as MRI contrast agents: Ligand design and properties of the complexes, *Dalt. Trans.* 9226 (2008) 3027–3047. <https://doi.org/10.1039/b719704g>.
- [10] M.R. Makowski, A.J. Wiethoff, C.H.P. Jansen, R.M. Botnar, Molecular imaging with targeted contrast agents, *Top. Magn. Reson. Imaging.* 20 (2009) 247–259.

<https://doi.org/10.1097/RMR.0b013e3181ea28b1>.

- [11] R.B. Lauffer, Paramagnetic Metal Complexes as Water Proton Relaxation Agents for NMR Imaging: Theory and Design, *Chem. Rev.* 87 (1987) 901–927.
<https://doi.org/10.1021/cr00081a003>.
- [12] C.Y. Yang, M.F. Tai, C.P. Lin, C.W. Lu, J.L. Wang, J.K. Hsiao, H.M. Liu, Mechanism of cellular uptake and impact of ferucarbotran on macrophage physiology, *PLoS One.* 6 (2011) 1–7.
<https://doi.org/10.1371/journal.pone.0025524>.
- [13] G.B. Toth, C.G. Varallyay, A. Horvath, M.R. Bashir, P.L. Choyke, H.E. Daldrup-Link, E. Dosa, J.P. Finn, S. Gahramanov, M. Harisinghani, I. Macdougall, A. Neuwelt, S.S. Vasanaawala, P. Ambady, R. Barajas, J.S. Cetas, J. Ciporen, T.J. DeLoughery, N.D. Doolittle, R. Fu, J. Grinstead, A.R. Guimaraes, B.E. Hamilton, X. Li, H.L. McConnell, L.L. Muldoon, G. Nesbit, J.P. Netto, D. Petterson, W.D. Rooney, D. Schwartz, L. Szidonya, E.A. Neuwelt, Current and potential imaging applications of ferumoxytol for magnetic resonance imaging, *Kidney Int.* 92 (2017) 47–66. <https://doi.org/10.1016/j.kint.2016.12.037>.
- [14] H. Nejadnik, P. Pandit, O. Lenkov, A.P. Lahiji, K. Yerneni, H.E. Daldrup-Link, Ferumoxytol Can Be Used for Quantitative Magnetic Particle Imaging of Transplanted Stem Cells, *Mol. Imaging Biol.* 21 (2019) 465–472.
<https://doi.org/10.1007/s11307-018-1276-x>.
- [15] P. Caravan, N.J. Cloutier, M.T. Greenfield, S.A. McDermid, S.U. Dunham, J.W.M. Bulte, J.C. Amedio, R.J. Looby, R.M. Supkowski, W.D.W. Horrocks, T.J. McMurry, R.B. Lauffer, The interaction of MS-325 with human serum albumin and its effect on proton relaxation rates, *J. Am. Chem. Soc.* 124 (2002) 3152–3162. <https://doi.org/10.1021/ja017168k>.
- [16] O.C. Richardson, O. Bane, M.L.J. Scott, S.F. Tanner, J.C. Waterton, S.P. Sourbron, T.J. Carroll, D.L. Buckley, Gadofosveset-based biomarker of tissue albumin concentration: Technical validation in vitro and feasibility in vivo, *Magn. Reson. Med.* 73 (2015) 244–253. <https://doi.org/10.1002/mrm.25128>.

- [17] G.N. Peeren, Stream function approach for determining optimal surface currents, *J. Comput. Phys.* 191 (2003) 305–321. [https://doi.org/10.1016/S0021-9991\(03\)00320-6](https://doi.org/10.1016/S0021-9991(03)00320-6).
- [18] R.A. Lemdiasov, R. Ludwig, A stream function method for gradient coil design, *Concepts Magn. Reson. Part B Magn. Reson. Eng.* 26 (2005) 67–80. <https://doi.org/10.1002/cmr.b.20040>.
- [19] M. Poole, R. Bowtell, Novel gradient coils designed using a boundary element method, *Concepts Magn. Reson. Part B Magn. Reson. Eng.* 31B (2007) 162–175. <https://doi.org/10.1002/cmr.b.20091>.
- [20] C.T. Harris, Optimization of a Boundary Element Approach To Electromagnet, *Sch. Grad. Postdr. Stud. Univ. West. Ontario.* (2013).
- [21] C.T. Harris, D.W. Haw, W.B. Handler, B.A. Chronik, Shielded resistive electromagnets of arbitrary surface geometry using the boundary element method and a minimum energy constraint, *J. Magn. Reson.* 234 (2013) 95–100. <https://doi.org/10.1016/j.jmr.2013.06.010>.
- [22] C.T. Harris, W.B. Handler, B.A. Chronik, Electromagnet design allowing explicit and simultaneous control of minimum wire spacing and field uniformity, *Concepts Magn. Reson. Part B Magn. Reson. Eng.* 41B (2012) 120–129. <https://doi.org/10.1002/cmr.b.21220>.
- [23] M.A. Pysz, S.S. Gambhir, J.K. Willmann, Molecular imaging: current status and emerging strategies, *Clin. Radiol.* 65 (2010) 500–516. <https://doi.org/10.1016/j.crad.2010.03.011>.
- [24] I.J. Hildebrandt, H. Su, W.A. Weber, Anesthesia and other considerations for in vivo imaging of small animals, *ILAR J.* 53 (2012) 17–26.
- [25] Z.Y. Chen, Y.X. Wang, Y. Lin, J.S. Zhang, F. Yang, Q.L. Zhou, Y.Y. Liao, Advance of molecular imaging technology and targeted imaging agent in imaging and therapy, *Biomed Res. Int.* 2014 (2014). <https://doi.org/10.1155/2014/819324>.
- [26] E.A. Waters, S.A. Wickline, Contrast agents for MRI, *Basic Res. Cardiol.* 103

- (2008) 114–121. <https://doi.org/10.1007/s00395-008-0711-6>.
- [27] J.K. Alford, B.K. Rutt, T.J. Scholl, W.B. Handler, B.A. Chronik, Delta relaxation enhanced mr: Improving activation - Specificity of molecular probes through R1 dispersion imaging, *Magn. Reson. Med.* 61 (2009) 796–802. <https://doi.org/10.1002/mrm.21933>.
- [28] C.T. Harris, W.B. Handler, Y. Araya, F. Martinez-Santesteban, J.K. Alford, B. Dalrymple, F. Van Sas, B.A. Chronik, T.J. Scholl, Development and optimization of hardware for delta relaxation enhanced MRI, *Magn. Reson. Med.* 72 (2014) 1182–1190. <https://doi.org/10.1002/mrm.25014>.
- [29] J.K. Alford, T.J. Scholl, W.B. Handler, B.A. Chronik, Design and construction of a prototype high-power B0 insert coil for field-cycled imaging in superconducting MRI systems, *Concepts Magn. Reson. Part B Magn. Reson. Eng.* 35 (2009) 1–10. <https://doi.org/10.1002/cmr.b.20132>.
- [30] U.C. Hoelscher, S. Lothar, F. Fidler, M. Blaimer, P. Jakob, Quantification and localization of contrast agents using delta relaxation enhanced magnetic resonance at 1.5 T, *Magn. Reson. Mater. Physics, Biol. Med.* 25 (2012) 223–231. <https://doi.org/10.1007/s10334-011-0291-6>.
- [31] C.T. Harris, W.B. Handler, T.J. Scholl, B.A. Chronik, A practical insert design for dreMR imaging in the human head, *Proc. 19th Sci. Meet. Int. Soc. Magn. Reson. Med.* (2011) 1839.
- [32] M. Bödenler, M. Basini, M.F. Casula, E. Umut, C. Gösweiner, A. Petrovic, D. Kruk, H. Scharfetter, R1 dispersion contrast at high field with fast field-cycling MRI, *J. Magn. Reson.* 290 (2018) 68–75. <https://doi.org/10.1016/j.jmr.2018.03.010>.
- [33] N. Chanet, G. Guillot, G. Willoquet, L. Jourdain, R.M. Dubuisson, G. Reganha, L. De Rochefort, Design of a fast field-cycling magnetic resonance imaging system, characterization and methods for relaxation dispersion measurements around 1.5 T, *Rev. Sci. Instrum.* 91 (2020). <https://doi.org/10.1063/1.5128851>.

- [34] U.C. Hoelscher, P.M. Jakob, Eddy current compensation for delta relaxation enhanced MR by dynamic reference phase modulation, *Magn. Reson. Mater. Physics, Biol. Med.* 26 (2013) 249–259. <https://doi.org/10.1007/s10334-012-0335-6>.
- [35] J. Alford, A.G. Sorensen, T. Benner, A. Chronik, B. Handler, J. Scholl, G. Madan, P. Caravan, Direct Protein Imaging of Inflammation in the Human Hand, *Proc. 19th Sci. Meet. Int. Soc. Magn. Reson. Med.* (2011) 0452.
- [36] Y.T. Araya, F. Martínez-Santesteban, W.B. Handler, C.T. Harris, B.A. Chronik, T.J. Scholl, Nuclear magnetic relaxation dispersion of murine tissue for development of T1 (R1) dispersion contrast imaging, *NMR Biomed.* 30 (2017) 1–10. <https://doi.org/10.1002/nbm.3789>.
- [37] C.T. Harris, J.K. Alford, W.B. Handler, T.J. Scholl, B.A. Chronik, Bo coil designs for in vivo delta relaxation enhanced MR in humans, *Proc. 18th Sci. Meet. Int. Soc. Magn. Reson. Med.* (2010) 1548.
- [38] Y. Wang, M. Spiller, P. Caravan, Evidence for weak protein binding of commercial extracellular gadolinium contrast agents, *Magn. Reson. Med.* 63 (2010) 609–616. <https://doi.org/10.1002/mrm.22214>.

Chapter 2

Characterization of magnetic field inhomogeneity and finite ramping period effects in dreMR

2.1 Introduction

The dreMR method at its most fundamental level is intended to produce quantitative molecular images by producing signal proportional to concentration of a T_1 dispersive contrast agent [1]. This is accomplished through combination of contrast agent choice, hardware design and pulse parameters, and post-processing. A number of assumptions are also made to derive this proportionality, some of which have not been addressed in detail by previous literature. Here, we will remove two of these assumptions individually – perfectly homogeneous field shifts, and instantaneous ramping – to determine their validity, and any restrictions to which point they can no longer be made.

2.1.1 The theory and assumptions of dreMR

In dreMR subtraction imaging [1], the goal is to measure two images collected identically, with the exception of the applied relaxation field strength during a pre-polarizing pulse. This is done by quickly tipping the pre-polarized magnetization into the transverse plane and acquiring the image rapidly before T_2 effects produce significant changes. That is, we attempt to measure the longitudinal magnetization present at the end of the pre-polarizing pulse (Eq. (2.1)). The general result being that these two images will only differ in the equilibrium magnetization by Curie's law (Eq (1.1)), which the signal is proportional to, and the relaxation rate of dispersive agent.

$$M_{z\pm} = M_0 \left(\frac{B_0 \pm \Delta B}{B_0} \right) (1 - e^{-\Delta t R_{1\pm}}) \quad 2.1$$

Here M_0 is taken to be the equilibrium magnetization at the main field strength (B_0), and $R_{1\pm}$ are the relaxation rates at the field strengths $B_0 \pm \Delta B$. In using this solution to the Bloch equations (Eq. (1.6)) we have made the assumptions that no longitudinal magnetization is present at time zero and, importantly to this chapter, that there is no time

dependence to the polarizing field. That is, that the field shift ramps on and off instantaneously.

Since the first of these field dependencies is simply a matter of scaling by the shifted field strength, it can easily be removed by the use of field compensation weightings applied to each image. Assuming a perfect 90° RF pulse was applied, the remaining changes are then exclusively due to dispersion and any signal remaining after subtraction will depend only on local dispersion. This weighted subtraction is then given by:

$$I_{sub} = \left(\frac{B_0}{B_0 - \Delta B} \right) kM_{z-} - \left(\frac{B_0}{B_0 + \Delta B} \right) kM_{z+} \quad 2.2$$

where k is a proportionality constant. The second assumption focused on in this chapter has now been made, by assuming that the field shift strength $\pm\Delta B$ determining the magnetization (Eq. (2.1)) is equal to the ideal field shift used in the field compensation weightings (Eq. (2.2)). That is, that the field shift produced by the dreMR hardware is perfectly homogenous and equal to the ideal field shift of the weightings.

Carrying out the expansion of this subtraction without any further assumptions gives the expression:

$$I_{sub} = kM_0(e^{-\Delta t \cdot R_{1+}} - e^{-\Delta t \cdot R_{1-}}) \quad 2.3$$

It is clear then that if no local dispersion occurs (i.e. $R_{1+} = R_{1-} = R_1$) the signal after a weighted subtraction will be zero. With instantaneous ramping and perfectly homogeneous field shifts, a dreMR subtraction image will perfectly cancel any non-dispersive signal, assuming none remained after the initial 90° RF pulse.

If an additional assumption is made that the dispersion relation is linear about B_0 with some slope R'_1 , and therefore the absolute change in relaxation rate from B_0 to $B_0 \pm \Delta B$ can be represented by ΔR_1 , the subtraction simplifies to:

$$R_{1\pm} \approx R_1 \pm \Delta B \cdot R'_1 = R_1 \pm \Delta R_1 \quad 2.4$$

$$I_{sub} \approx 2kM_0 \sinh(\Delta t \Delta R_1) e^{-\Delta t \cdot R_1} \quad 2.5$$

where R_1 is the total relaxation rate of the tissue and contrast agent together at B_0 . If pulse parameters are chosen so that $\Delta t \cdot \Delta R_1$ and $\Delta t \cdot R_1$ remain small, the dreMR subtraction can be further simplified giving:

$$I_{sub} \approx 2kM_0\Delta t\Delta B \cdot r'_1 \cdot [CA] \quad 2.6$$

where we have substituted R'_1 for the slope of the agent relaxivity r'_1 and the local concentration $[CA]$ (Eq. (1.10)) [2]. Thus, the result of a dreMR subtraction gives signal proportional to concentration of T_1 dispersive contrast agent, canceling any non-dispersive signal in the process [1].

2.1.2 Removing the instantaneous ramping assumption

While investigation has been made into compensating for eddy currents produced on a scanner bore for dreMR which otherwise produce image artifacts [3,4], these studies did not address the direct effect the ramping period has on an image. The derivations for dreMR in the past have assumed a perfectly square field shift pulse, solving the longitudinal Bloch equation with equilibrium magnetization scaled by the field shift [1].

$$\frac{dM_z}{dt} = R_{1\pm} \left[M_0 \left(\frac{B_0 \pm \Delta B}{B_0} \right) - M_z \right] \quad 2.7$$

However, because the dreMR insert coil carries some resistance and inductance, the system will take some time to ramp up to field and ramp back down, resulting in a pulse shape that is trapezoidal, and depends on time. The longitudinal Bloch equation then becomes:

$$\frac{dM_z}{dt} = R_1(B_0 \pm \Delta B(t)) \left[M_0 \left(\frac{B_0 \pm \Delta B(t)}{B_0} \right) - M_z \right] \quad 2.8$$

where relaxation rate is a function of field strength, $R_1(B_0 \pm \Delta B(t))$, due to the dispersion relation, and the absolute field shift as a function of time $\Delta B(t)$ is given by:

$$\Delta B(t) = \begin{cases} \eta \frac{V}{R} (1 - e^{-Rt/L}), & \text{for ramp up} \\ \Delta B, & \text{for flat top} \\ \Delta B - \eta \frac{V}{R} (1 - e^{-Rt/L}), & \text{for ramp down} \end{cases} \quad 2.9$$

Where we have used the equation for current in an RL circuit with resistance R , inductance L , a maximum supply voltage V , and the field efficiency of the dreMR coil η . The result of any given combination of these equations (Eq. (2.8 and 2.9)) is a linear first order ordinary differential equation (ODE), solvable with the proper choice of integrating factor.

2.1.3 Removing the homogenous field shift assumption

As a dreMR sequence does not apply the field shifting pulse during excitation or acquisition, and therefore does not affect the Larmor frequencies of spins in the subject, field shift inhomogeneities have been assumed to have little effect on the resulting images [1,4–8]. Previous hardware designs for animals have reported small regions of interest with up to 2% field inhomogeneity [4], and designs for human dreMR coils have considered up to 20% inhomogeneity to be acceptable [7,8]. However, none of these have explicitly addressed what effect field inhomogeneities have on a dreMR subtraction image.

To remove the assumption that the dreMR field shift is perfectly homogeneous, we allow the local magnetization at the end of a perfectly square pulse (Eq. (2.1)) to depend on the local field shift ΔB^* , which differs from the ideal field shift used in the field compensation weightings (Eq. (2.2)) by some inhomogeneity H given as the percent difference between the local field and the ideal field at the ROI center.

$$M_{z\pm} = M_0 \left(\frac{B_0 \pm \Delta B^*}{B_0} \right) (1 - e^{-\Delta t \cdot R_{1\pm}^*}) \quad 2.10$$

Here the relaxation rate $R_{1\pm}^*$ also depends on the inhomogeneous field shift, and we will again approximate the dispersion relation to be linear giving:

$$R_{1\pm}^* \approx R_1 \pm \Delta B^* \cdot R_1' = R_1 \pm \Delta R_1^* \quad 2.11$$

Inserting this magnetization (Eq. (2.10)) into the dreMR subtraction (Eq. (2.2)) will give a new expression accounting for field shift inhomogeneities.

2.2 Methods

2.2.1 Analytic finite ramping effects model

A number of assumptions will be made to simplify the ODE's describing a dreMR pulse with finite ramping. We begin by assuming the field strength ramps on and off linearly:

$$\Delta B(t) = \eta \frac{V}{R} \left(1 - e^{-\frac{Rt}{L}}\right) \approx \frac{\eta V}{L} t \quad 2.12$$

which holds so long as the power amplifier is capable of providing a far greater voltage than required for the desired current ($V_{max} \gg IL$ and IR). This will give perfectly trapezoidal dreMR pulses. The resulting coefficient is then defined as the coil's slew rate (ξ). If we maintain the previous assumption of dreMR that dispersion is linear, the Bloch equation for ramping the coil up to field becomes:

$$\frac{dM_z}{dt} \approx (R_1 \pm R_1' \xi t) \left[M_0 \left(\frac{B_0 \pm \xi t}{B_0} \right) - M_z \right] \quad 2.13$$

This ODE can be solved with an integrating factor approach, given in detail in Appendix A.1. If we assume that the time spent ramping will be small, ignoring terms of $O(t^2)$ and higher, we can reduce the solution to a linear growth of magnetization, with relaxation rate and equilibrium magnetization for the static field strength B_0 (Eq. (2.14)).

$$M_z(t) \approx M_z(0) + R_1 t (M_0 - M_z(0)) \quad 2.14$$

We can use the same approach for modeling the magnetization during a ramping down period. Applying the linear ramping and linear dispersion again to the Bloch equation with the new field gives the equation:

$$\frac{dM_z}{dt} \approx [R_1 \pm R_1' (\Delta B - \xi t)] \left[M_0 \left(\frac{B_0 \pm \Delta B \mp \xi t}{B_0} \right) - M_z \right] \quad 2.15$$

With the appropriate choice of another integrating factor, and continuing the assumption of small ramping time, the solution reduces to another linear growth of magnetization, this

time with relaxation rate and equilibrium magnetization for the field strength during the pulse $B_0 \pm \Delta B$ (Eq. (2.16)).

$$M_z(t) \approx M_z(0) + t \cdot R_{1\pm} \left[M_0 \left(\frac{B_0 \pm \Delta B}{B_0} \right) - M_z(0) \right] \quad 2.16$$

We now have expressions for longitudinal magnetization during the three periods of a dreMR field shifting pulse: the ramp up period (Eq. (2.14)), the flat-top period (Eq. (2.1)), and the ramp down period (Eq. (2.16)). If we start with the initial condition that the dreMR pulse immediately follows a 90° RF pulse (resulting in zero longitudinal magnetization at time zero) and propagate through our solutions, we find that after the full duration of the dreMR pulse the magnetization is given by:

$$M_{z\pm}(2\Delta t_r + \Delta t_f) \approx M_0 \Delta t_r R_1 + M_0 \left(\frac{B_0 \pm \Delta B}{B_0} \right) (\Delta t_r + \Delta t_f) R_{1\pm} \quad 2.17$$

where Δt_r is the time spent ramping on one end of a pulse, and Δt_f is the flat-top duration. Here we have continued the assumption that ramping times are small, as well as the assumption that flat-top duration is small from the original dreMR derivation, and therefore ignored terms of $O(\Delta t_r^2)$, $O(\Delta t_f^2)$, and $O(\Delta t_r \cdot \Delta t_f)$.

Inserting the final magnetizations into the weighted dreMR subtraction (Eq. (2.2)), expanding and simplifying results in the expression:

$$I_{sub} \approx 2kM_0\Delta B \left[\left(\frac{B_0}{B_0^2 - \Delta B^2} \right) R_1 \Delta t_r - R'_1 (\Delta t_r + \Delta t_f) \right] \quad 2.18$$

It is also convenient to express this result in terms of slew rate as it is a parameter that we can discuss coil designs in terms of.

$$I_{sub} \approx 2kM_0\Delta B \left[\left(\frac{B_0}{B_0^2 - \Delta B^2} \right) R_1 \left(\frac{\Delta B}{\xi} \right) - R'_1 \left(\left(\frac{\Delta B}{\xi} \right) + \Delta t_f \right) \right] \quad 2.19$$

Unlike the instantaneous ramping case, the resulting signal is not proportional to concentration of dispersive agent. There is now a difference of two terms, the first of which depends on the unenhanced relaxation rate R_1 meaning non-dispersive signal is not properly canceled, and the second of which is the ideal signal increased by the ramping period time.

This new relation implies three important changes to the dreMR image. Signal from non-dispersive tissue will remain in the image post subtraction, the signal will inaccurately measure concentration of dispersive agent, and the signal now depends on the sign of the dispersion relation R'_1 . The last of these changes stems from the fact that signal is an absolute value. When the dreMR subtraction was proportional to R'_1 , its sign had no effect as positive and negative relations resulted in the same absolute value. In the new relation, if R'_1 is negative (as it commonly is) the two terms will add together and contrast between dispersive agent and non-dispersive tissue will be less susceptible to ramping effects. However, in the rare cases where R'_1 is positive, the contrast between agent and tissue will be much more susceptible to these effects, and signal from contrast agent locations can even reach zero.

2.2.2 Analytic field inhomogeneity effects model

Modeling the effects of field shift inhomogeneities in a dreMR subtraction image is considerably less complicated and does not require new solutions to the Bloch equations, yet produces very similar results. We begin by substituting the inhomogeneous magnetizations (Eq. (2.10)) for a perfectly square dreMR pulse into the ideal field dreMR subtraction:

$$I_{sub} = \left(\frac{B_0}{B_0 - \Delta B} \right) kM_{z-}^* - \left(\frac{B_0}{B_0 + \Delta B} \right) kM_{z+}^* \quad 2.20$$

If we make the original dreMR assumptions once again that dispersion is linear and that pulse parameters are chosen so that $\Delta t \cdot \Delta R_1$ and $\Delta t \cdot R_1$ remain small and their second order terms can be ignored, the weighted subtraction gives:

$$I_{sub} \approx \frac{2kM_0\Delta t}{B_0^2 - \Delta B^2} [B_0(\Delta B - \Delta B^*)R_1 - \Delta B^*(B_0^2 - \Delta B^*\Delta B)R'_1] \quad 2.21$$

The general implications of this result are extremely similar to that of the finite ramping model (Eq. (2.19)). The subtraction again results in a difference of two terms, with the first representing a non-dispersive signal contribution. As with the finite ramping model, the sign of R'_1 will affect the image's susceptibility to field inhomogeneities.

However, unlike the ramping model, the first term can now be negative or positive as well, depending if the inhomogeneous field shift ΔB^* is greater or less than the ideal shift ΔB . As we will see in the following sections, the susceptibility of dreMR subtraction images to field inhomogeneities will increase when these terms have the same signs.

If we consider the signal from a non-dispersive tissue with no contrast agent present ($R'_1 = 0$), we see that it is proportional to the difference in the inhomogeneous field and the ideal field. As the absolute value of signal is what matters, this can be replaced by the percent inhomogeneity H of the field shift at that point.

$$I_{sub_0} \approx \frac{2kM_0B_0\Delta t}{B_0^2 - \Delta B^2} (\Delta B - \Delta B^*)R_1 \approx \frac{2kM_0B_0\Delta B\Delta t}{B_0^2 - \Delta B^2} R_1 \left(\frac{H}{100} \right) \quad 2.22$$

The result is also proportional to the relaxation rate at B_0 of the tissue, so it can be expected that high R_1 tissues like fat will produce the most signal under an inhomogeneous field shift.

2.2.3 Bloch simulations of finite ramping effects

In the derivation of the finite ramping dreMR subtraction (Eq. (2.18)) many assumptions were made to simplify the problem and produce an intuitive, understandable solution. However, through numerical simulation in MATLAB (R2020b, Mathworks, Natick, NA) a more accurate result can be found without the need for these assumptions.

The simulation follows an object-oriented layout, consisting of a “Sample” class, a “Pulse” class, and a “BlochDremr” class. For a given simulation the user supplies a Sample object with details of the discretized simulation domain including size and positions, background tissue T_1 values (**Table 2.1**), spatial contrast agent concentration, and the relaxivity data of the agent to be used. The user supplies a Pulse object with details of the dreMR pulse to be applied including amplitude, flat top duration, and slew rate. The Sample and Pulse objects are then passed along to a BlochDremr object as well as the main magnet field strength B_0 , and the simulations are carried out within.

Table 2.1. Tissue Longitudinal Relaxation Time Constants	
Tissue	T_1 (ms)
muscle	900
cerebrospinal fluid (CSF)	4500
grey matter (GM)	950
white matter (WM)	600
fat	250
blood	1200

Table 2.1. Background tissue longitudinal relaxation times. Adapted from Table 4.1 of [9].

The initial condition is maintained that the longitudinal magnetization has been nulled prior to the dreMR pulse, as well as the assumption of linear ramping (Eq. (2.12)) which allows us to discuss simulations in terms of slew rate. The ODEs for ramping the coil on and off given by the combinations of the Bloch and field shift equations (Eqs. (2.8) and (2.12)) are solved numerically using MATLAB's ode45 function which implements an explicit Runge-Kutta 4,5 method. For each simulation, the sample is subjected to a ramp-up period with ode45, propagated through the standard analytic solution in static field (Eq. (2.1)), and further propagated through a ramp-down period once more with ode45. The relaxation rate at some field strength is determined by linear interpolation of dispersive agent relaxivity data multiplied by the user set concentration, plus the relaxation rate of surrounding material/tissue (Eq. (1.10)). To complete a dreMR image the simulation is carried out with a positive and a negative pulse, and the weighted subtraction (Eq. (2.2)) is applied to the results.

To clearly visualize the effects that finite ramping time can have on dreMR images, a grid of simulations was carried out with various background tissues, concentrations of dispersive agent, and ramping times (**Figure 2.1**). Our agents were always simulated in the presence of blood as VivoTrax and Feraheme are blood pool agents and Ablavar only exhibits dispersion when bound to serum albumin in the blood [10–14]. The ramping times are presented relative to the pulse flat-top duration for a given grid. For each grid of simulations only one contrast agent is used, as a realistic image would not contain more than one agent, and the presence of multiple agents would confuse the normalization of results. These grids were also assembled for different values of B_0 to determine sensitivity at low field and regions where dispersion relations are positively correlated rather than the

typical negative correlation. The analytic model was also compared to simulation results for various slew rates and field shifts.

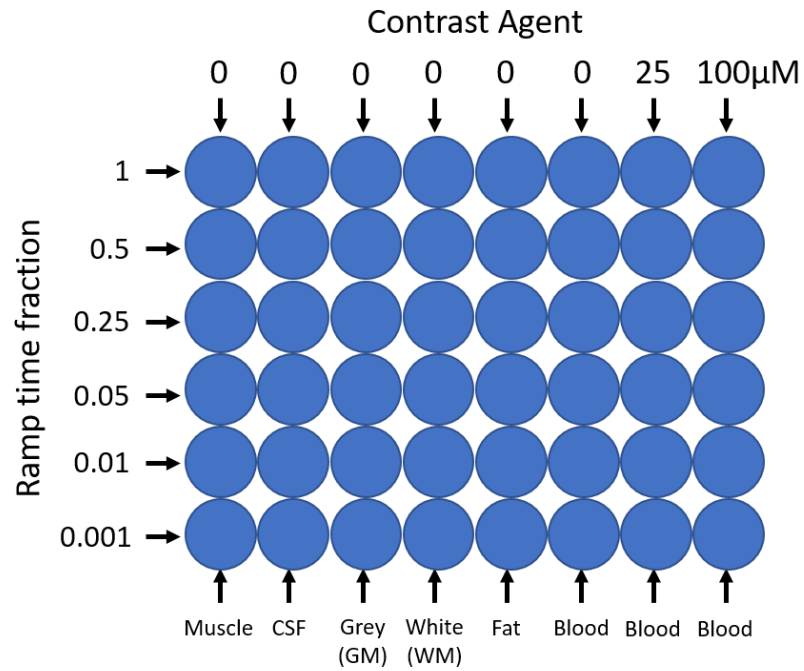


Figure 2.1. Grid layout for simulated dreMR subtraction imaging. Ramp time fraction increases vertically from bottom to top: 0.001, 0.01, 0.05, 0.25, 0.5, 1. Ramp time fraction defined as $2\Delta t_r / \Delta t_f$. Tissues and agent concentrations vary horizontally from left to right: muscle, CSF, GM, WM, fat, blood, blood + 25µM agent, blood + 100µM agent.

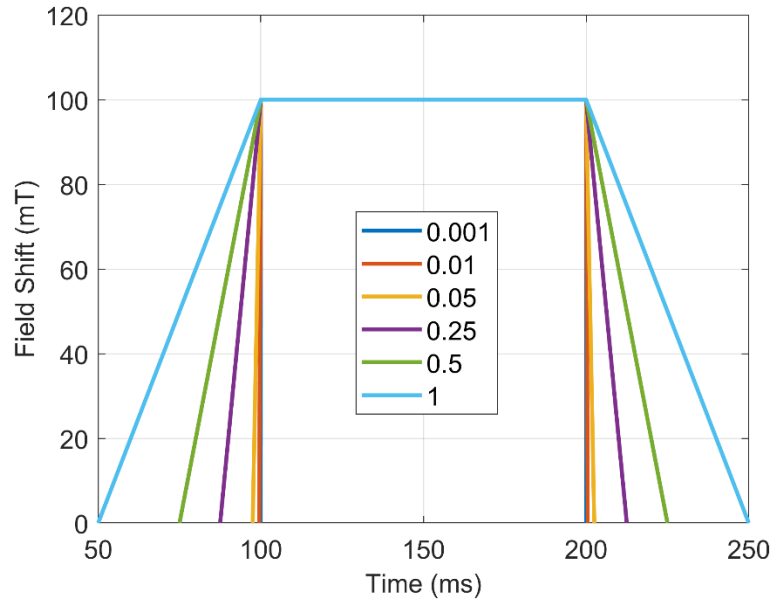


Figure 2.2. Trapezoidal dreMR pulses for finite ramping time grid simulations of **Figure 2.1**. Pulse shapes are given for ramp time fractions of: 0.001, 0.01, 0.05, 0.25, 0.5, 1.

2.2.4 Bloch simulations of field inhomogeneity effects

While the derivation of inhomogeneous dreMR subtraction used exact solutions to the Bloch equations, the standard dreMR approximations were made for relaxivity to be linear with field strength and higher order time effects to be ignored. While the equations resulting without these approximations would be overly complicated and not provide meaningful insight on inspection, they can easily be used in simulation to provide a visual representation of these effects.

To begin simulation the same Pulse and Sample objects are created following the methods of section 2.2.3. However, the slew rate is now set to be infinite, bypassing the ramping periods in simulation, and the dreMR pulse amplitude is set to an inhomogeneous value ΔB^* as compared to the ideal value ΔB used in the field compensation weights. This inhomogeneous field shift can be greater (ΔB_+^*) or less (ΔB_-^*) than the ideal shift and will be distinguished by:

$$\Delta B_{\pm}^* = \Delta B \left(1 \pm \frac{H}{100\%} \right) \quad 2.23$$

When the user creates the BlochDremr object and runs the simulation, the standard analytic Bloch solution for a static field (Eq. (2.10)) is used with the field shift ΔB_{\pm}^* . The results are then carried through the weighted subtraction with weights using the ideal shift value. Grids of these simulations are created similar to those of section 2.2.3, but with varying field shift inhomogeneity rather than ramping time (**Figure 2.3**). Again, each grid only contains one contrast agent and one background field strength B_0 , however they are now also each distinguished by whether the field inhomogeneity is greater or less than the ideal value. The analytic model was also compared to simulation results for various inhomogeneities and field shifts.

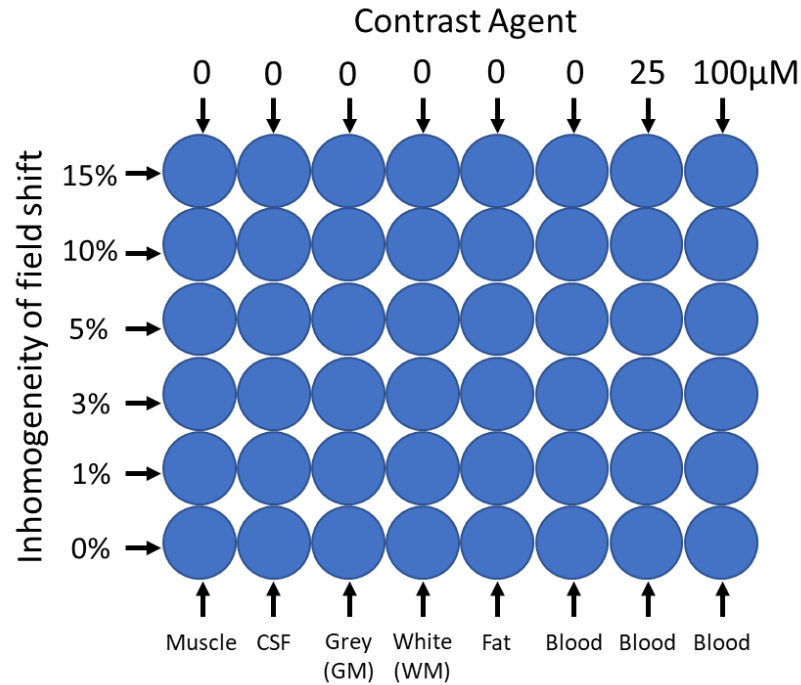


Figure 2.3. Grid layout for simulated dreMR subtraction imaging. Inhomogeneity increases vertically from bottom to top: 0%, 1%, 3%, 5%, 10%, 15%. Tissues and agent concentrations vary horizontally from left to right: muscle, CSF, GM, WM, fat, blood, blood + 25µM agent, blood + 100µM agent.

2.3 Results

2.3.1 Finite Ramping Effects Results

The grid simulations outlined in section 2.2.3 for finite ramping periods are shown in **Figure 2.4** for a main magnet field strength of 1.3T, a 100ms flat top duration, and a 100mT field shift. The main field strength of 1.3T was used rather than 1.5T to prevent extrapolation of relaxivity data under field shifts. These simulations were carried out for comparison with the agents VivoTrax, Feraheme, and Ablavar in its bound state. The simulation reveals that signal due to non-dispersive tissue is not properly canceled and increases as time spent ramping on and off increases. The non-dispersive signal is also higher for tissues with high R_1 values. We can see that the signal for dispersive agent is also increasing with ramping time.

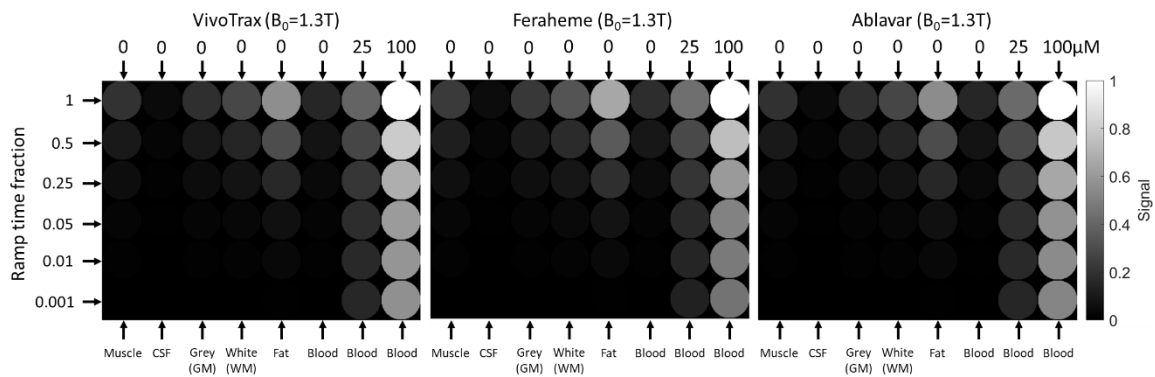


Figure 2.4. Finite ramp time grid simulations for various contrast agents. From left to right grids use the dispersive agents VivoTrax, Feraheme, and bound state Ablavar. Results normalized to highest values. Simulations at $B_0 = 1.3\text{T}$, $\Delta B = 100\text{mT}$, and a flat-top duration of 100ms.

Sensitivity to this effect was found to increase only slightly with lower main field strength. However, **Figure 2.5** shows the results of the grid simulation for Ablavar at low field ($B_0 = 0.3\text{T}$) where the agent's relaxivity becomes positively correlated with field strength. The common field strength of 0.5T cannot be used for Ablavar due to its local maximum in relaxivity at that strength. A field shift of 100mT with a flat top duration of 100ms was used once again. While the non-dispersive tissues exhibit the same behavior as at the higher field strength, absolute signal in the presence of Ablavar is now seen to

decrease with increasing ramp time, pass through a zero value, and begin increasing once more.

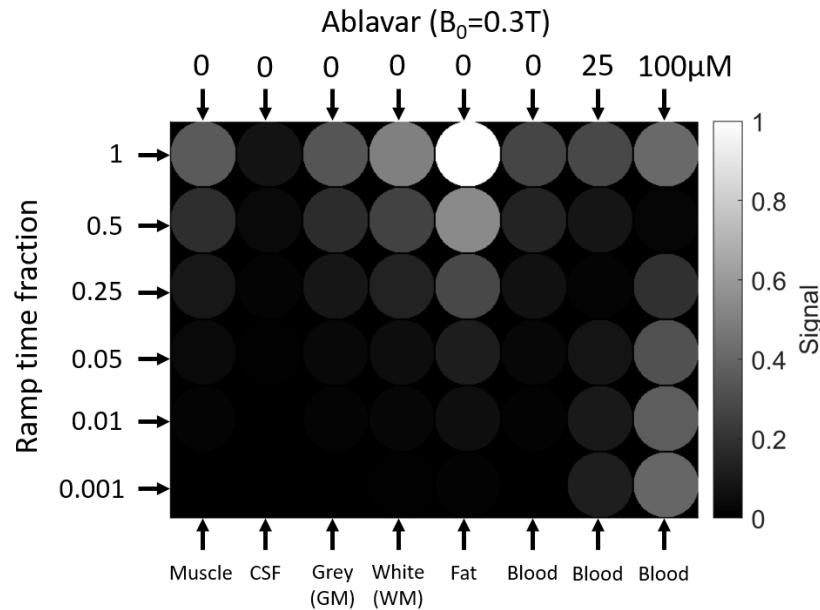


Figure 2.5. Finite ramp time grid simulation for bound state Ablavar. Results normalized to highest value. Simulations at $B_0 = 0.3T$, $\Delta B = 100mT$, and a flat-top duration of 100ms.

The analytic model for finite ramping time derived in section 2.2.2 (Eq. (2.18)) was compared to simulation results and the ideal dreMR subtraction (Eq. (2.6)) for varying slew rate (**Figure 2.6 (a)** and **(c)**) and field shift strength (**Figure 2.6 (b)** and **(d)**). A main field strength of 0.5T and a flat top duration of 50ms were used. A slew rate of 50T/s and a field shift of 0.1T were used when not varied. This comparison was made for blood both without dispersive agent and with 50 μM Feraheme. When no dispersive agent was present the model and simulation matched almost perfectly, while the ideal case of course predicts zero signal. In the presence of Feraheme the finite ramping model more closely fit simulation than the ideal model. This fit worsens with larger flat top durations, agent concentrations, and field shifts.

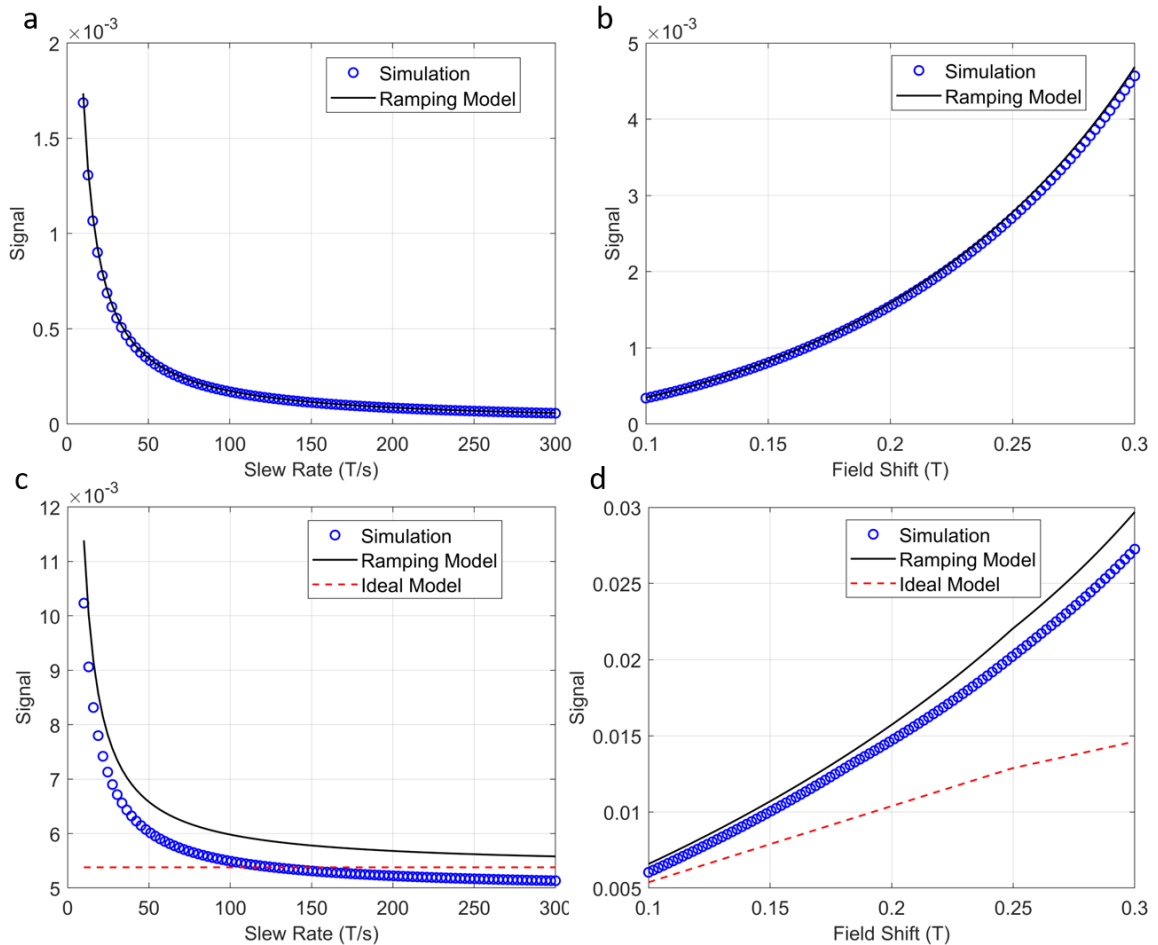


Figure 2.6. Finite ramp time simulation and model comparisons for (a) blood over varying slew rate, (b) blood over varying field shift strength, (c) blood and 50 μ M VivoTrax over varying slew rate, (d) blood and 50 μ M VivoTrax over varying field shift strength. Simulations at $B_0 = 0.5$ T, and a flat-top duration of 50ms. Slew rate of 50T/s and field shift of 100mT used when not varied.

2.3.2 Inhomogeneous Field Shift Effects Results

The grid simulations described in section 2.2.4 for inhomogeneous field shifts were applied for negative inhomogeneities ΔB_-^* (Figure 2.7) and positive inhomogeneities ΔB_+^* (Figure 2.8). A main magnet field strength of 1.3T, a 100ms flat top duration, and a 100mT ideal field shift were used once again. These were carried out for comparison with the agents VivoTrax, Feraheme, and Ablavar in its bound state. As with the finite ramping simulations, we can see that field inhomogeneities result in improper canceling of signal

from non-dispersive tissue, with remaining signal increasing with inhomogeneity. In the presence of negative inhomogeneities signal from dispersive agent was seen to increase with inhomogeneity. However, these signals were seen to decrease with inhomogeneity for positive inhomogeneities resulting in further loss of differentiation between non-dispersive tissue and contrast agent.

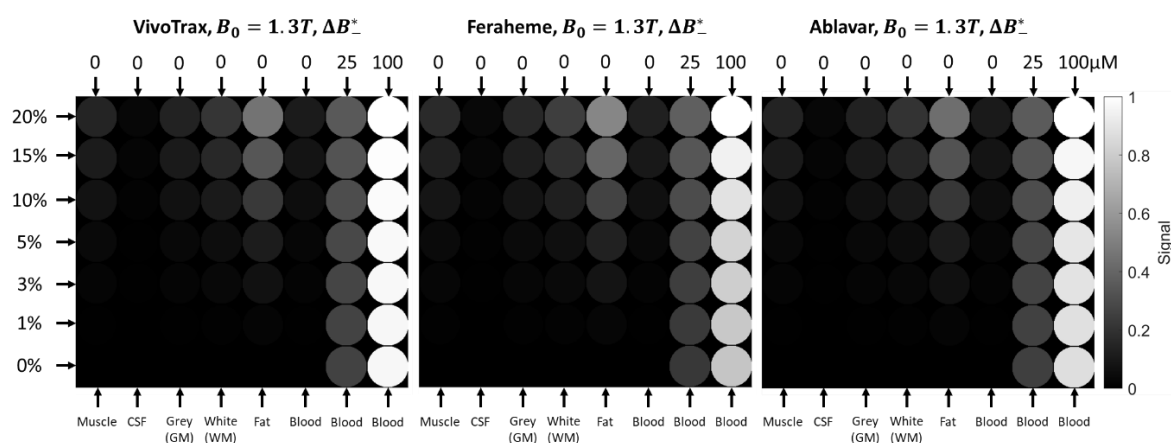


Figure 2.7. Negative inhomogeneity grid simulations for various contrast agents. From left to right grids use the dispersive agents VivoTrax, Feraheme, and bound state Ablavar. Results normalized to highest values. Simulations at $B_0 = 1.3\text{T}$, $\Delta B = 100\text{mT}$, and a flat-top duration of 100ms.

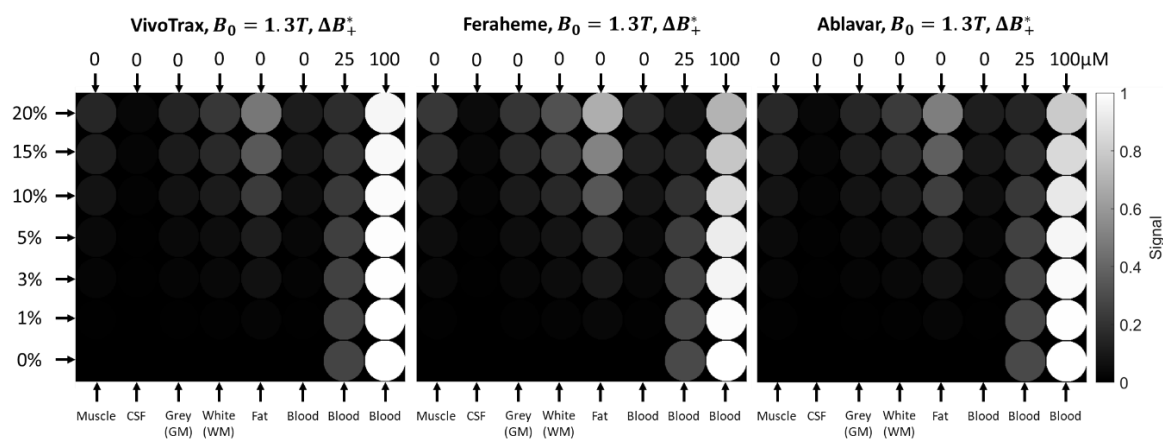


Figure 2.8. Positive inhomogeneity grid simulations for various contrast agents. From left to right grids use the dispersive agents VivoTrax, Feraheme, and bound state Ablavar. Results normalized to highest values. Simulations at $B_0 = 1.3\text{T}$, $\Delta B = 100\text{mT}$, and a flat-top duration of 100ms.

Sensitivity to inhomogeneities was found to increase at lower main field strengths. In particular, the behavior of Ablavar at low field strengths is again of interest as its

relaxivity becomes positively correlated with field strength below 0.5T. Grid simulations with a low field strength ($B_0 = 0.3T$) but otherwise same parameters as above are shown for Ablavar with negative inhomogeneities and positive inhomogeneities (**Figure 2.9**). We can see that sensitivity to inhomogeneities has greatly increased with the low field strength, and that the behavior of contrast agent signal has reversed for positive and negative inhomogeneities. While the agent signal now increases with increasing positive inhomogeneities, the same signal decreases with negative inhomogeneities even passing through zero and regrowing in the case of the lower concentration ($25\mu M$).

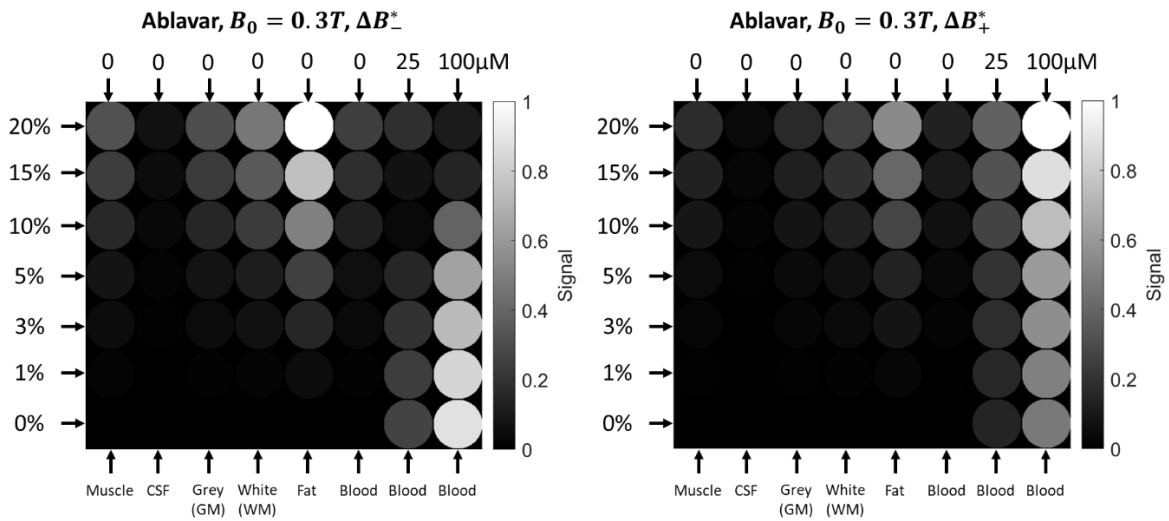


Figure 2.9. Inhomogeneous field shift grid simulations for bound state Ablavar at low field. Left figure uses negative inhomogeneities while the right uses positive. Results normalized to highest values. Simulations at $B_0 = 0.3T$, $\Delta B = 100mT$, and a flat-top duration of 100ms.

The analytic model for inhomogeneous field shifts derived in section 2.2.3 (Eq. (2.20)) was compared to simulation results and the ideal dreMR subtraction (Eq. (2.6)) for varying field shift inhomogeneity (**Figure 2.10 (a) and (c)**) and field shift strength (**Figure 2.10 (b) and (d)**). A main field strength of 0.5T and a flat top duration of 50ms were used, and only negative inhomogeneities were presented for simplicity. In the field shift strength figures an inhomogeneity of 10% was used. These comparisons were made for blood both without dispersive agent and with $50\mu M$ Feraheme. When no dispersive agent was present the model and simulation matched almost perfectly, while the ideal case of course predicts

zero signal. In the presence of Feraheme the inhomogeneous field shift model more closely fit simulation than the ideal model. This fit worsens with larger flat top durations, agent concentrations, and field shifts.

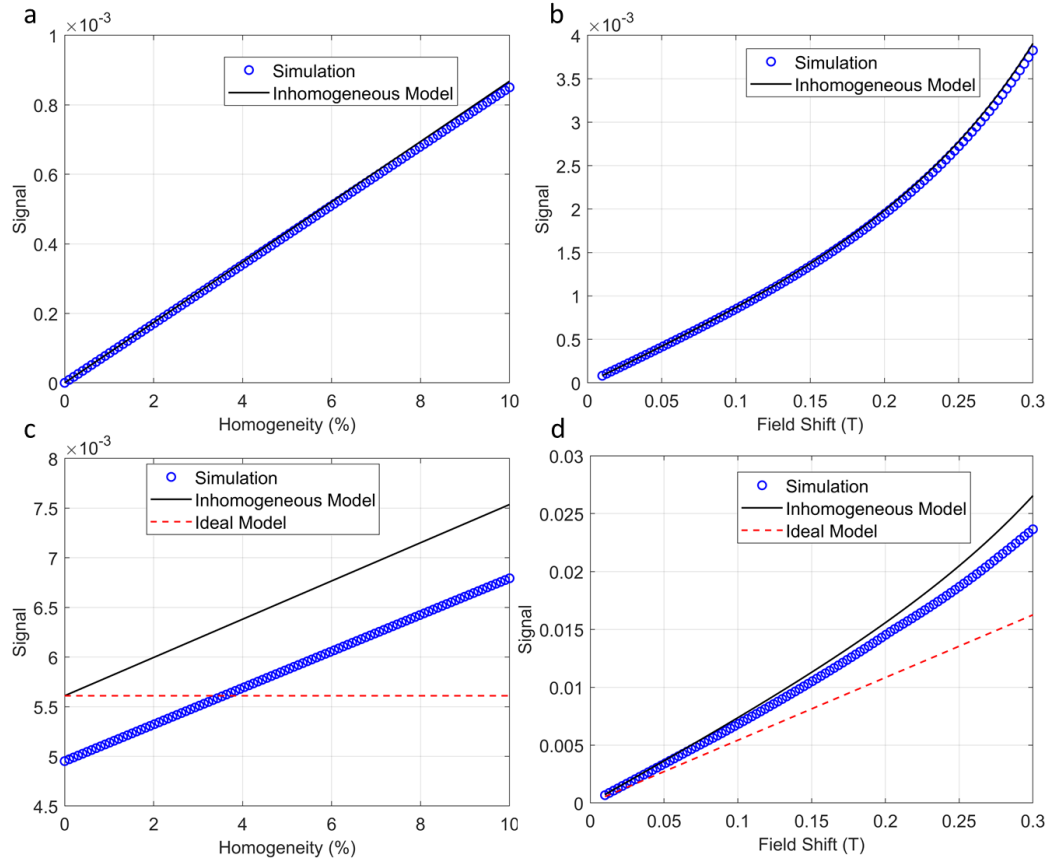


Figure 2.10. Inhomogeneous field shift simulation and model comparisons for (a) blood over varying inhomogeneity, (b) blood over varying field shift strength, (c) blood and 50 μ M VivoTrax over varying inhomogeneity, (d) blood and 50 μ M VivoTrax over varying field shift strength. Simulations at $B_0 = 0.5$ T, and a flat-top duration of 50ms. Inhomogeneity of 10% and field shift of 100mT used when not varied.

2.4 Discussion

2.4.1 Discussion of Finite Ramping Effects

In the derivation of the finite ramping model in section 2.2.1 it was predicted that a term in the resulting dreMR subtraction will remain independent of any dispersion relation,

depending only on the relaxation rate at the main field strength R_1 (Eq. (2.18)). We can see this is confirmed in our simulations where signal remains for non-dispersive tissue, with higher signal for higher R_1 tissues like fat. In fact, in the 1.3T examples of **Figure 2.4**, we can see that fat becomes indistinguishable from 25 μ M of any of our agents when the total ramping time reaches a quarter of the flat top duration. When the total ramping time is below at least 5% (0.05) of the flat top duration, the contrast agent largely becomes differentiable from fat. For a dreMR pulse of 100mT and 100ms this equates to a slew rate of at least 40T/s.

The behavior of Ablavar at low field was also predicted by the finite ramping model. At fields below ~ 0.5 T the dispersion relation of Ablavar becomes positive rather than negative. This means that the two terms of the model (Eq. (2.18)) are subtracting from one another, and of course we measure the absolute value of the result. For short ramping times the dispersive term dominates, but as ramping time increases the non-dispersive term grows faster resulting in an overall decrease in signal. Eventually the two terms become equal and the total signal is zero. As the ramping time increases past this point the non-dispersive term grows larger than the dispersive term, resulting in a return of signal. However, at this point we can no longer determine the concentration of the agent and it is almost impossible to locate even qualitatively.

At higher field strengths where dispersion for all agents was negative, the two terms of the model would add together, resulting in increase of all signals with ramping time (although proportionality to concentration is still lost). When an agent has a positive dispersion relation like Ablavar at low field, the difference of terms makes the image much more sensitive to ramping effects. In this example (**Figure 2.5**), we can see that to clearly differentiate between fat and Ablavar at low field we require the total ramping time to be less than 1% (0.01) of the flat top duration. For this 100mT, 100ms pulse this equates to a slew rate of at least 200 T/s.

While such a slew rate may be possible for small animal coils and safe for animal studies, it would be very difficult to design for in humans and could cause cardiac or peripheral nerve stimulation (PNS) [15]. The slew rate requirement can be lowered by increasing flat top duration, but this results in signal saturation and loss of concentration

proportionality. Using smaller field shifts will also allow for lower slew rate but will lose some contrast. It should also be noted that the results for Ablavar at low field are much more sensitive to field shift strength than the negatively correlated agents.

VivoTrax and Feraheme maintain similar results to **Figure 2.4** at low fields and with various field shift strengths. However, to minimize finite ramping effects we want to ramp the dreMR coil as fast as possible. In a smaller low field system, in particular our compact head-specific cryogen-free 0.5T superconducting magnet, distance between the insert coil and bore is reduced leading to higher amplitude eddy currents induced on the main magnet's surfaces. These eddy currents could potentially heat the system leading to a quench. To ensure dreMR operation is safe in the compact system for high slew rates, experiments were carried out with our current generation dreMR coil inside the low field magnet to monitor inside temperature during dreMR pulses as detailed in Appendix B.1. No significant heating of the low field system was measured during dreMR coil operation.

2.4.2 Discussion of Inhomogeneous Field Shift Effects

As with finite ramping, in the derivation of the inhomogeneous field shift model in section 2.2.2 it was predicted that a term in the resulting dreMR subtraction will remain independent of any dispersion relation, depending only on the relaxation rate at the main field strength R_1 (Eq. (2.21)). We can see this is again confirmed in our simulations where signal remains for non-dispersive tissue, with higher signal for high R_1 tissues like fat. We can also see that the sensitivity to field inhomogeneities is higher for positive inhomogeneities, which are decreasing signal from agent at 1.3T, than negative inhomogeneities which are increasing signal. This is because all three agents exhibit negative dispersion relations in this range resulting in a difference of terms in the model (Eq. (2.20)) when a positive inhomogeneity is present, and an addition of terms when a negative inhomogeneity is present. In the 1.3T examples of **Figure 2.7** and **Figure 2.8**, we can see that fat becomes indistinguishable from 25 μ M of any of our agents in the presence of a 10% negative inhomogeneity or a 5% positive inhomogeneity. We can also see that in either case it is best to limit inhomogeneities below 1% to suppress fat signals.

Similarly, at low field where Ablavar has a positive dispersion relation, the agent has an increased sensitivity to negative inhomogeneities which will result in a difference of terms while positive inhomogeneities result in an addition. Sensitivity for all agents to both types of inhomogeneities also increases at low field, likely due to the dispersive term (Eq. (2.20)) decreasing faster with B_0 than the non-dispersive. The non-dispersive term also grows faster with inhomogeneity than the dispersive, resulting in the signal from Ablavar crossing zero and loss of any usable concentration information at higher inhomogeneities. This will occur for any combination of dispersion relation and positive/negative inhomogeneities that results in a difference of terms. In the low field examples of **Figure 2.9**, we can see that fat becomes indistinguishable from 25 μ M Ablavar in the presence of a 3% negative inhomogeneity or a 5% positive inhomogeneity. We can also see that in either case it is again best to limit inhomogeneities below 1% to suppress fat signals.

2.5 Conclusions

Models accounting for finite ramping and inhomogeneous field shift effects in dreMR subtraction imaging were derived and were able to explain the behavior of simulated dreMR images. A simulation environment was established to inform design requirements based on desired dreMR pulse parameters, agents, and main field strengths. Both finite ramping and inhomogeneous field shifts were found to result in signal remaining from dispersion-free tissue, and a loss of proportionality to dispersive contrast agent concentration. These effects were shown to cause a loss of differentiation between contrast agent and high R_1 tissues such as fat.

Loss of differentiation due to finite ramping was shown to be greater for low field Ablavar. For VivoTrax, Feraheme, and 1.3T Ablavar slew rates of at least 40T/s are required for a typical dreMR pulse, while low field Ablavar requires at least 200T/s to differentiate from fat. However, many regions of interest may contain little to no fat, and in regions where fat is present prior images could be taken to determine its location. These results are also subject to pulse parameters and simulations should be run for the specific pulse sequence to be applied. It remains best practice to ramp to field as quickly as possible,

and Appendix B.1 shows that such high slew rate pulses would not cause main magnet safety concerns.

Loss of differentiation due to field inhomogeneities was worst when dispersion sign and inhomogeneity type (ΔB_{\pm}^*) results in a difference of terms (Eq. (2.20)) and worsens with lower field. In some cases, fat became indistinguishable at as low as 3%, and in all cases it is best to keep inhomogeneity below 1%. The effects of field inhomogeneities can be minimized in two ways. The first is to produce field maps of the imaging region for the specific dreMR coil in operation, and use these maps to inform accurate, spatially dependent field compensation weightings for the dreMR subtraction (Eq. (2.2)). This is a post-processing solution which would not eliminate inhomogeneity effects under patient/animal motion. The second is to eliminate the error at the source by developing an improved field inhomogeneity design method for dreMR coils. In practice a combination of these two solutions should be used.

2.6 References

- [1] J.K. Alford, B.K. Rutt, T.J. Scholl, W.B. Handler, B.A. Chronik, Delta relaxation enhanced mr: Improving activation - Specificity of molecular probes through R1 dispersion imaging, *Magn. Reson. Med.* 61 (2009) 796–802.
<https://doi.org/10.1002/mrm.21933>.
- [2] R.B. Lauffer, Paramagnetic Metal Complexes as Water Proton Relaxation Agents for NMR Imaging: Theory and Design, *Chem. Rev.* 87 (1987) 901–927.
<https://doi.org/10.1021/cr00081a003>.
- [3] U.C. Hoelscher, P.M. Jakob, Eddy current compensation for delta relaxation enhanced MR by dynamic reference phase modulation, *Magn. Reson. Mater. Physics, Biol. Med.* 26 (2013) 249–259. <https://doi.org/10.1007/s10334-012-0335-6>.
- [4] C.T. Harris, W.B. Handler, Y. Araya, F. Martinez-Santesteban, J.K. Alford, B. Dalrymple, F. Van Sas, B.A. Chronik, T.J. Scholl, Development and optimization of hardware for delta relaxation enhanced MRI, *Magn. Reson. Med.* 72 (2014)

- 1182–1190. <https://doi.org/10.1002/mrm.25014>.
- [5] J.K. Alford, T.J. Scholl, W.B. Handler, B.A. Chronik, Design and construction of a prototype high-power B₀ insert coil for field-cycled imaging in superconducting MRI systems, *Concepts Magn. Reson. Part B Magn. Reson. Eng.* 35 (2009) 1–10. <https://doi.org/10.1002/cmr.b.20132>.
- [6] U.C. Hoelscher, S. Lothar, F. Fidler, M. Blaimer, P. Jakob, Quantification and localization of contrast agents using delta relaxation enhanced magnetic resonance at 1.5 T, *Magn. Reson. Mater. Physics, Biol. Med.* 25 (2012) 223–231. <https://doi.org/10.1007/s10334-011-0291-6>.
- [7] C.T. Harris, J.K. Alford, W.B. Handler, T.J. Scholl, B.A. Chronik, Bo coil designs for in vivo delta relaxation enhanced MR in humans, *Proc. 18th Sci. Meet. Int. Soc. Magn. Reson. Med.* (2010) 1548.
- [8] C.T. Harris, W.B. Handler, T.J. Scholl, B.A. Chronik, A practical insert design for dreMR imaging in the human head, *Proc. 19th Sci. Meet. Int. Soc. Magn. Reson. Med.* (2011) 1839.
- [9] R.W. Brown, Y.-C.N. Cheng, E.M. Haacke, M.R. Thompson, R. Venkatesan, *Magnetic Resonance Imaging: Physical Principles and Sequence Design*, 2nd ed., Wiley Blackwell, Hoboken, NJ, 2014.
- [10] C.Y. Yang, M.F. Tai, C.P. Lin, C.W. Lu, J.L. Wang, J.K. Hsiao, H.M. Liu, Mechanism of cellular uptake and impact of ferucarbotran on macrophage physiology, *PLoS One*. 6 (2011) 1–7. <https://doi.org/10.1371/journal.pone.0025524>.
- [11] G.B. Toth, C.G. Varallyay, A. Horvath, M.R. Bashir, P.L. Choyke, H.E. Daldrup-Link, E. Dosa, J.P. Finn, S. Gahramanov, M. Harisinghani, I. Macdougall, A. Neuwelt, S.S. Vasanawala, P. Ambady, R. Barajas, J.S. Cetas, J. Ciporen, T.J. DeLoughery, N.D. Doolittle, R. Fu, J. Grinstead, A.R. Guimaraes, B.E. Hamilton, X. Li, H.L. McConnell, L.L. Muldoon, G. Nesbit, J.P. Netto, D. Petterson, W.D. Rooney, D. Schwartz, L. Szidonya, E.A. Neuwelt, Current and potential imaging

- applications of ferumoxytol for magnetic resonance imaging, *Kidney Int.* 92 (2017) 47–66. <https://doi.org/10.1016/j.kint.2016.12.037>.
- [12] H. Nejadnik, P. Pandit, O. Lenkov, A.P. Lahiji, K. Yerneni, H.E. Daldrup-Link, Ferumoxytol Can Be Used for Quantitative Magnetic Particle Imaging of Transplanted Stem Cells, *Mol. Imaging Biol.* 21 (2019) 465–472. <https://doi.org/10.1007/s11307-018-1276-x>.
- [13] P. Caravan, N.J. Cloutier, M.T. Greenfield, S.A. McDermid, S.U. Dunham, J.W.M. Bulte, J.C. Amedio, R.J. Looby, R.M. Supkowski, W.D.W. Horrocks, T.J. McMurry, R.B. Lauffer, The interaction of MS-325 with human serum albumin and its effect on proton relaxation rates, *J. Am. Chem. Soc.* 124 (2002) 3152–3162. <https://doi.org/10.1021/ja017168k>.
- [14] O.C. Richardson, O. Bane, M.L.J. Scott, S.F. Tanner, J.C. Waterton, S.P. Sourbron, T.J. Carroll, D.L. Buckley, Gadofosveset-based biomarker of tissue albumin concentration: Technical validation in vitro and feasibility in vivo, *Magn. Reson. Med.* 73 (2015) 244–253. <https://doi.org/10.1002/mrm.25128>.
- [15] Medical electrical equipment — Part 2-33: Particular requirements for the basic safety and essential performance of magnetic resonance equipment for medical diagnosis, *Int. Electrotech. Comm.* 03 (2010).

Chapter 3

An improved homogeneity design method for dreMR systems

This chapter is adapted from the currently unpublished paper: McCready MA, Handler WB, Chronik BA, *An improved homogeneity design method for fast field-cycling coils in molecular MRI*.

3.1 Introduction

Delta relaxation enhanced magnetic resonance is a powerful FFC method for quantitative molecular imaging. The dreMR method improves specificity between bound and unbound contrast agents and does not require imaging pre-injection [1]. An FFC insert coil is used to shift the magnitude of the main magnetic field of an MRI as part of the pulse preparation phase of the pulse sequence. Images are acquired following positive and negative shifts of ΔB and subjected to a field-compensated image subtraction. Using contrast agents with T_1 dispersion this subtraction can produce signal proportional to concentration of bound agent.

Thus far, dreMR has been demonstrated for quantification and localization of agents [1–3], and measurement of tissue and agent T_1 dispersion [4], but not yet in a clinical trial. Previous designs for the FFC insert coil have typically consisted of a thick resistive solenoid with an outer shield to counter inductive coupling with the main magnet [3,5–8]. Interaction with the main magnet cannot be entirely negated, leading to small eddy currents within the bore which create artefacts during image acquisition. These eddy currents can be compensated for using a dynamic frequency adjustment, or with the addition of a low power Helmholtz coil [7,9].

While improvements in FFC dreMR hardware have been focused on shielding, eddy current compensation, and switching mechanisms, little attention has been given to field shift homogeneity. It has previously been believed that the dreMR insert coil does not

require high homogeneity, as the system is only used in a pulse preparation phase and not during acquisition [1,2,5,7]. However, as we have seen in Chapter 2, field inhomogeneities can create significant errors in dreMR subtraction resulting in prediction of agent where none is present and incorrect measurements of agent concentration [10]. This effect severely limits the imaging region for a dreMR coil. We found that to mitigate these effects, in particular for low field imaging, inhomogeneities should generally be limited to $<1\%$.

A whole-body system for clinical FFC-MRI has been constructed with high homogeneity over the region of interest (ROI) [11]. However, this system is a full scanner rather than an insert coil, and is intended exclusively for low-field FFC imaging with a maximum field strength of 0.2 T. It was previously argued that a shielded insert dreMR coil with cylindrical geometry could not be made to a viable size for dreMR imaging in humans, and that a system with open geometry designed by the BEM would be required instead [12]. When such systems were designed for head and body imaging, they exhibited a 20% field inhomogeneity over the regions of interest, which was deemed to be acceptable [13]. Later, a cylindrical geometry head system was designed which achieved a 10-20% field inhomogeneity depending on the imaging region, but with a large outer diameter of $\sim 51\text{cm}$ [6]. As we determined in the previous chapter, inhomogeneities of this size would result in a loss of differentiation between dispersive agent and non-dispersive tissue, especially fat, white matter, and grey matter. While these designs were never constructed, the most recently constructed dreMR coil, which was designed for imaging small animals, provides a $<1.8\%$ inhomogeneity over an ROI occupying less than $1/3$ of the coil's 9cm inner diameter [7].

While inhomogeneity effects can be mitigated by detailed volumetric mapping of the coil's field and subsequent correction in post-processing, sub-voxel movement and diffusion of contrast agent in regions of large field inhomogeneity would still confound quantification. A better solution is to design the coil with field inhomogeneities sufficiently low that the effect is insignificant. Here, we will present an improved homogeneity design method, allowing for improved control over the size and location of the dreMR imaging ROI. This method will allow for maximization of usable volume within dreMR inserts allowing the future design of compact, homogeneous clinical dreMR coils.

3.2 Methods

3.2.1 Design overview

While previously used FFC coils were designed as a shielded, thick solenoid with a central split, our new design method will use a uniform thick solenoid with an inner layer of windings specifically placed to improve field homogeneity (**Figure 3.1**). This correction layer is designed using the BEM, typically applied to the design of gradient and shim coils [14–16]. The electromagnetic shield will also be designed with the BEM and its calculations coupled with those of the correction layer.

A similar application of the BEM has been made for FFC coils in NMR [17]. While this FFC-NMR design method uses an outer corrective layer designed by the BEM, these windings are designed to have a separate dynamic control rather than run in series with the main windings, with the purpose of correcting field drift and dynamic inhomogeneities caused by thermo-mechanical stress. In our FFC-MRI design method, the corrective windings are chosen to correct static inhomogeneities, allow for control of ROI location, and run in series with the main windings. Additionally, while the FFC-NMR design does not include any form of electromagnetic shielding, our new design method includes a BEM designed shield that runs in series with the rest of the magnet. One of the main advantages of our new design method is the coupling of shield and correction coil calculations allowing for simultaneous shielding and improved homogeneity.

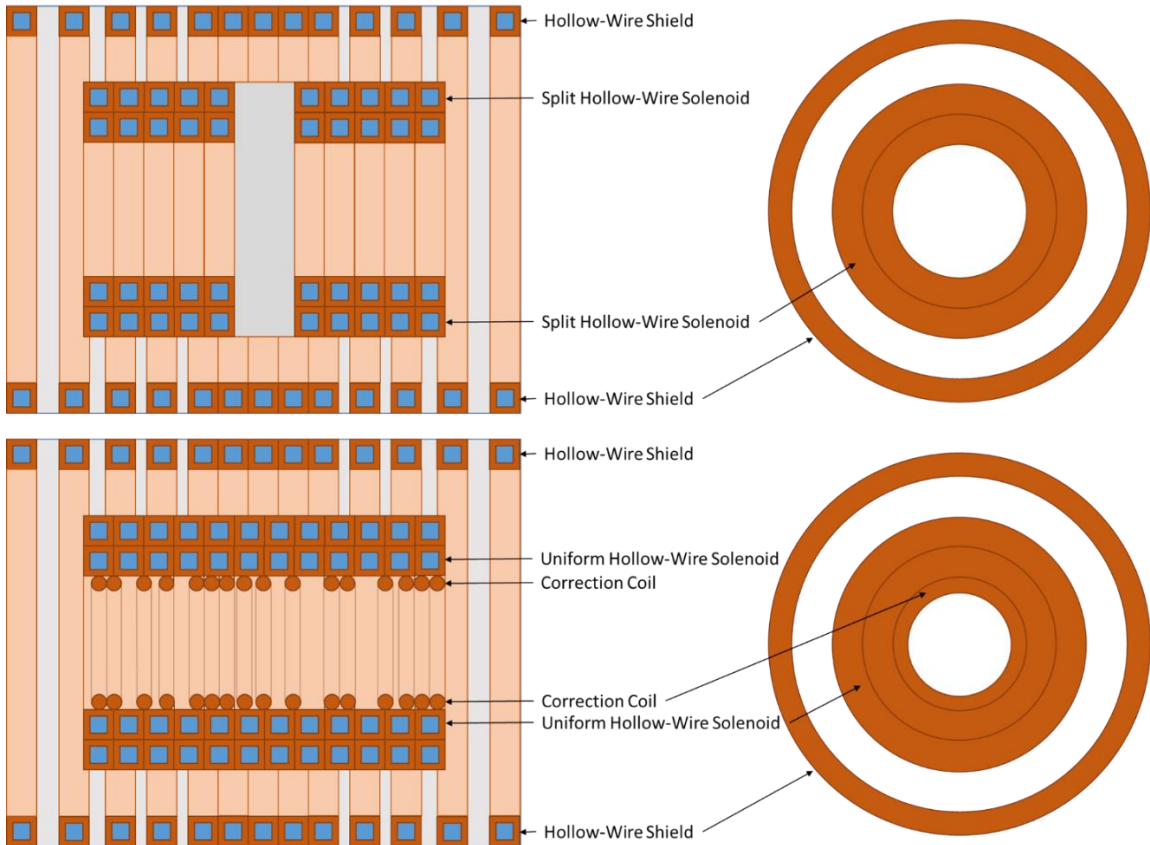


Figure 3.1. Cross sections of dreMR coil in YZ (**LEFT**) and XY (**RIGHT**) planes. (**TOP**) Previous dreMR coil designs consisting of axially split thick solenoid and an outer shield. (**BOTTOM**) New dreMR coil designs consisting of uniform thick solenoid, inner correction coil, and outer shield. In both designs the thick solenoid and shield use hollow wires pumped with water inside as coolant. The inner correction coil can also be made from hollow wire or cooled by proximity to the thick solenoid if finer solid wire is used. All layers are electrically connected in series.

3.2.2 Boundary element method

The BEM is a finite element method for finding the current density on a given surface that produces a desired field. An arbitrary surface geometry is discretized into a mesh of finite elements. A stream function, from which current density is obtained, is then calculated over the surface. This was done using piecewise linear shape functions and triangular mesh elements for which the stream function is given by:

$$\psi(\mathbf{r}) \approx \sum_{n=1}^N I_n \psi_n(\mathbf{r}) \quad 3.1$$

where $\psi(\mathbf{r})$ is the stream function, $\psi_n(\mathbf{r})$ is the set of basis functions described in [14], and I_n is the weighting coefficient of the stream function at node n which we solve for.

We can form a cost functional dependent on the stream function values to be minimized for the solution we require. In this work our corrective and shield windings will contribute little to the coil's total inductance. For this reason, we consider a minimum power functional to allow focus on reducing heating, with a field uniformity term to produce the desired field shape:

$$U = \frac{1}{2K} \sum_{k=1}^K [B_z(\mathbf{r}_k) - B_z^{tar}(\mathbf{r}_k)]^2 + \frac{\beta}{2} P \quad 3.2$$

Here, $B_z(\mathbf{r}_k)$ is the z-component of the magnetic field produced by our stream functions at target point k , $B_z^{tar}(\mathbf{r}_k)$ are our K target z-component field values, P is the power deposited in the BEM surfaces by the stream functions, and β is a chosen weighting between power and field uniformity terms. When an acceptable solution is acquired, the stream function values are contoured on their respective surfaces giving us the necessary wire patterns for winding the coils [15,16].

3.2.3 Improving dreMR homogeneity

Design of our next generation dreMR FFC coils begins with the choice of solenoid parameters. This includes number of radial (NR) and axial (NZ) windings, inner coil radius (r_i), and wire gauge. These choices will be the main factors in determining field shift strength (ΔB), slew rate (ξ), field efficiency, and weight. The design of thick solenoids can be optimized following the methods of [18].

From here, the correction coil and shield coil surfaces are chosen, and their meshes generated. This includes choosing the shield radius and axial length for both the shield and correction coils. As the problem has cylindrical symmetry, the mesh can be chosen to be made up of rings of nodes at the same z value which would, based on symmetry, necessarily have the same stream function value for each ring. The already programmed and implemented BEM previously detailed collapses the calculation of sets of nodes that will have the same stream function value to a single quasi node [12]. Previously this has been

done to treat all nodes on a common edge as having the same stream function, to stop nonphysical flow of current from a surface at an edge. This mechanism is used on the rings, which speeds up calculation by reducing the problem to one dimension. The wire gauges for the surfaces and the field target points are then chosen.

When all user decisions are made, the parameters are passed to our BEM implementation for winding placement of correction and shield coils. The BEM is first applied for a minimum energy design on the shield surface [19]. Here we solve for stream function values I_s^{sol} which shield only the chosen solenoid, minimizing the energy of a system containing themselves and the solenoid.

We then find the correction stream function values I_p which correct the field due to the solenoid and its shield values, as well as the coupled shield values I_s^{corr} which shield the correction coil without loss of homogeneity. This is done using the equation for the design functional (Eq. (3.2)) and the coupled shield values solved for in [19] resulting in the functional:

$$U = \frac{1}{2K} \sum_{k=1}^K [I_{pn} \tilde{c}_{pn}(\mathbf{r}_k) - B_z^{tar}(\mathbf{r}_k)]^2 + \frac{\beta}{2} I_{pn} I_{pm} \tilde{R}_{pnm} \quad 3.3$$

where \tilde{c}_{pn} and \tilde{R}_{pnm} are the coupled field and resistance matrices as defined in [19]. The target field values are chosen to offset the difference in field between the ROI center and each target point, and are given by:

$$B_z^{tar}(\mathbf{r}_k) = \left(B_z^{sol}(\mathbf{r}_0) + I_{sq}^{sol} c_{sq}(\mathbf{r}_0) \right) - \left(B_z^{sol}(\mathbf{r}_k) + I_{sq}^{sol} c_{sq}(\mathbf{r}_k) \right) \quad 3.4$$

where \mathbf{r}_0 is the ROI center. Substituting these targets into the design functional (Eq. (3.3)) and minimizing for I_p gives us the correction and coupled shield stream functions which will correct the field due to the solenoid and its shield values.

The two sets of shield values I_s^{sol} and I_s^{corr} are then scaled and added together to obtain values for a full shield I_s . The scaling factor λ is found by taking the ratio of I_s^{sol} contour spacing to I_s^{corr} contour spacing and applying to the values I_s^{corr} .

$$\lambda = \frac{I_s^{sol} \text{ contour spacing}}{I_s^{corr} \text{ contour spacing}}; \quad I_s^{corr} = \lambda I_s^{corr} \quad 3.5$$

The full shield coil contour spacing is then set to that of I_s^{sol} and the wire patterns obtained.

To allow for proper cooling and choice of a wire gauge, we must have explicit control of wire spacing in the resulting designs. In order to simultaneously control the wire spacing and field uniformity of designs an iterative weighting calculation is implemented [19]. While the individual shield calculations for the solenoid and correction coil and subsequent combination allows high field homogeneity without detriment to shielding, it complicates control of design wire spacing. Our desired wire spacing and uniformity can be achieved in the correction coil following exactly the methods of [20] using the iterative weight calculations. However, an additional outer iteration must be applied for the shield design after combination of I_s^{sol} and I_s^{corr} . As the shield coil uses a minimum energy method with no field targets, this iteration has no uniformity target and updates only relative power weights β . All weights begin with an initial value of one. The final solution is then contoured to produce the desired wire pattern. A summary of the design chain for our improved homogeneity method may be found in **(Figure 3.2)**.

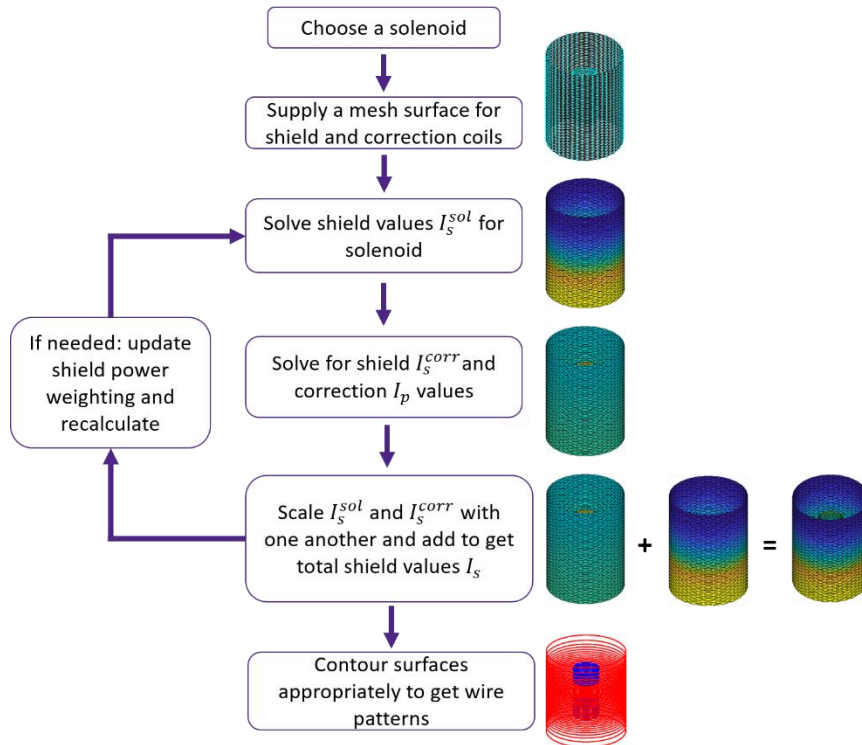


Figure 3.2. Design flow chart for the improved homogeneity design method. Beginning with choice of solenoid, generation of meshes, solving for solenoid shield, solving for correction coil and its shield, scaling, and combining shields, and contouring for wire patterns when the desired wires pacing is achieved. Steps 3-5 are iterated over, updating shield power weighting until reaching desired wire spacing.

3.2.4 Evaluation of Selected Designs

To demonstrate the improved design method, a dreMR coil was designed to the same size parameters as our current generation coil [13] with the new method. This coil is for small animal imaging, with an inner radius of 4.5cm and outer radius of 15cm, with a solenoid axial length of 18.5cm and a shield axial length of 31cm. The new design has no central axial split in the main solenoid and contains an inner correction coil while the previous design is a split solenoid with no correction coil. All windings were chosen to have an outer wire diameter of 5.3mm. The field inhomogeneity maps of both designs were simulated using a numerical Biot-Savart law calculator, and a simulated comparison of shielding performance was also made with the coils set to produce a field shift of 100mT.

In addition to improving homogeneity and increasing the size of imaging regions, the new design method should also be capable of moving the imaging region. As a proof of concept, a design is presented similar to those above in size, but with the imaging region center shifted 5cm down the positive z-axis. This coil again has an inner radius of 4.5cm and outer radius of 15cm, with a solenoid length of 18.5cm and a shield length of 31cm. The correction coil here uses 3.5mm wire and has only 4 radial layers for greater success in homogenizing the ROI. A shielded uniform solenoid of the same dimensions with no correction coil is used for comparison with the ROI-shifted design.

3.2.5 Image Simulation

To exhibit the improvement this design method can have on dreMR imaging, the methods of section 2.2.3 were employed to simulate dreMR images with inhomogeneous field shifts. Unlike the simulations of the previous chapter, an inhomogeneous field shift is not specified to a pulse object, but rather the ideal field shift value is supplied along with a coil design represented by discrete current elements. The current through these elements is then scaled such that the field produced at the center of the design's ROI is equal to the ideal field shift. The rest of the simulation domain is then subjected to the design's specific inhomogeneous field shift. Field maps were obtained using a numerical Biot-Savart calculator.

This simulation environment was applied for three domains. The first contained a uniform 160 μ M concentration of VivoTrax with a background T_1 value of 1.2s to simulate the presence of the agent in blood. The dreMR pulse parameters used a main field of 0.5T, dreMR pulses of 100mT, and a pulse duration of 100ms. The standard dreMR weighted subtraction [1] was then applied to the simulated magnetizations, and a percent difference test performed across the domain with comparison to the perfectly homogenous field case. The second domain used a background T_1 of 1.2s to simulate blood, a cylinder of fat with a T_1 value of 0.25s, and three cylinders of 25 μ M, 75 μ M, and 125 μ M VivoTrax each with background T_1 values of blood, with a main field of 0.5T.

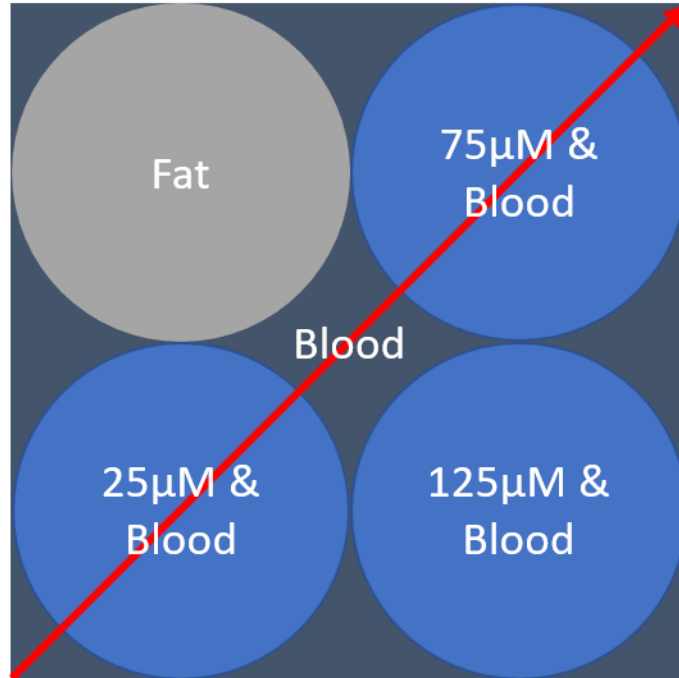


Figure 3.3. Domain for simulated dreMR subtraction imaging with coil design field maps. Background contains blood, grey circle contains fat, blue circles contain blood and VivoTrax or Ablavar in concentrations of $25\mu\text{M}$, $75\mu\text{M}$, and $125\mu\text{M}$. Red arrow denotes line profiles to be plotted.

The third domain again used a background T_1 of 1.2s to simulate blood, a cylinder of fat with a T_1 value of 0.25s, and this time three cylinders of $25\mu\text{M}$, $75\mu\text{M}$, and $125\mu\text{M}$ Ablavar and blood. Two simulations were produced on this domain, one with a main field of 0.3T and symmetric $100\text{mT} \pm \Delta B$ dreMR pulses, and one with a main field of 0.5T and asymmetric dreMR pulses of 0mT and -200mT. While we have not modeled asymmetric subtractions, we can expect them to produce similar images to the symmetric case. Here in the case of low field Ablavar images the asymmetric subtraction is more realistic as our low field system has a main field strength of 0.5T at which Ablavar relaxivity is at a local maxima, and symmetric field shifts would not satisfy the necessary linear condition in relaxivity.

A line profile across the simulated image of each domain was plotted for the designs and for a simulation using a perfectly homogeneous field shift. Percent differences were calculated between the simulations using the specific designs and the perfectly homogeneous case for all pixels containing contrast agent. Non-dispersive tissue pixels

were not included as these produce a signal of zero for a perfectly homogeneous shift, making a percent difference meaningless. The results of these percent difference tests were plotted as histograms normalized to the number of dispersive pixels. All simulations in this work were performed on custom code created in MATLAB (R2020b, Mathworks, Natick, MA).

3.3 Results

3.3.1 Comparison with previously constructed design

The newly designed dreMR coil was compared to the current generation design through simulation of their field homogeneity maps. **Figure 3.4** displays the homogeneity contour maps of the previous and new coil designs. **Figure 3.4 (a)** and **(b)** show homogeneity maps for the previous coil in the XY and XZ planes respectively. **Figure 3.4 (c)** and **(d)** show homogeneity maps for the newly designed coil in the XY and XZ planes respectively. We can see that the field homogeneity of the new design has vastly improved upon the previous, with the majority of the coil's volume falling under 1% and even 0.1% inhomogeneity as opposed to the previous design's 10%. Considering a spherical volume concentric with the coils, the new design can image on such a sphere of diameter 8.5cm with inhomogeneity <1%, while the previous design can only do so on a diameter of 5cm.

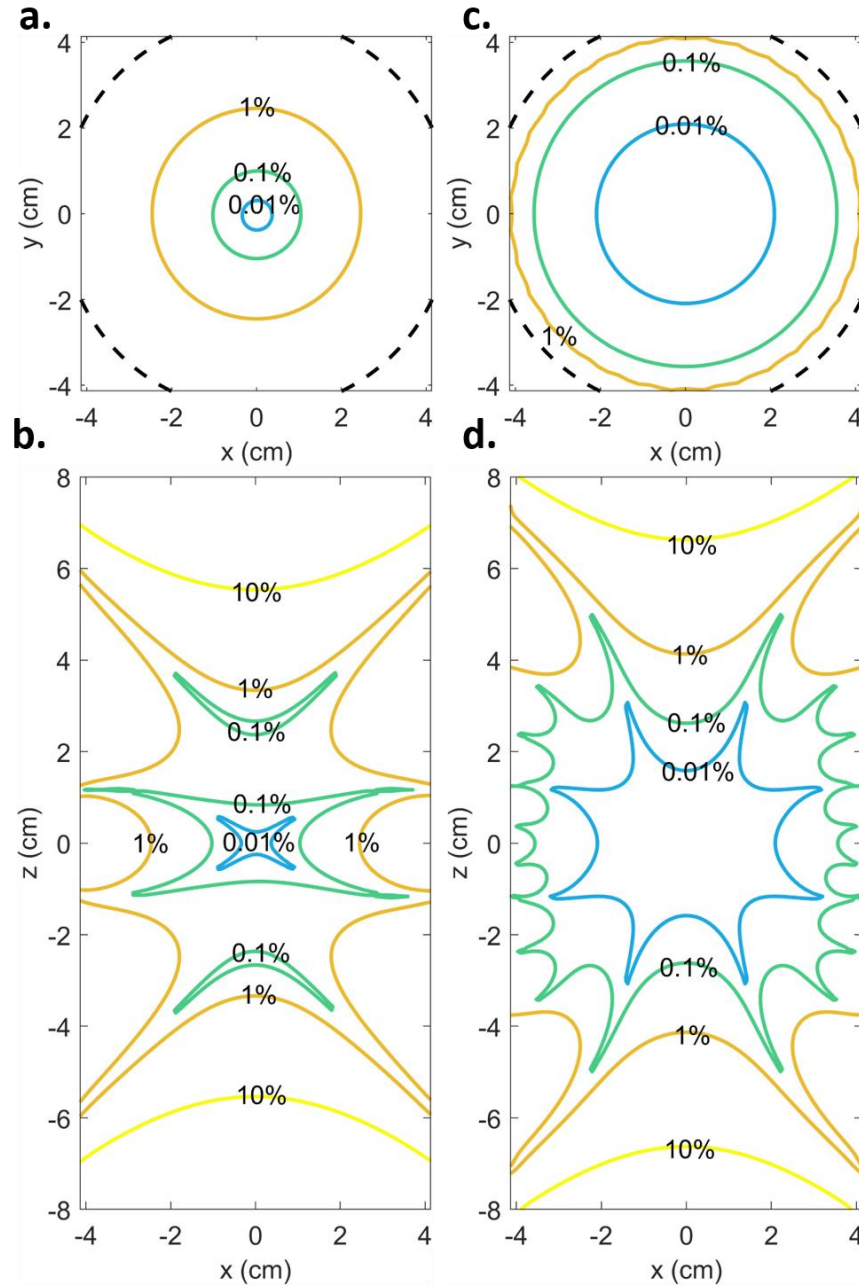


Figure 3.4. Inhomogeneity contour maps for (a) the previously constructed coil in the XY plane at $Z = 0$, (b) the previous coil in the XZ plane, (c) the newly designed coil in the XY plane at $Z = 0$, and (d) the new design in the XZ plane. Both coils have an inner radius of 4.6cm, represented by the dashed black line in the XY plane.

To compare the shielding performance of the two designs the total field strength of each design was plotted along the x-axis radially outwards from the center of the coils at $z = 0$. The field strength here exhibits the same behavior as any value along the z-axis, with the highest total values in this region. The inner and outer (shield) radii of the coils

are also denoted with vertical lines (**Figure 3.5**). We can see that the field drops off faster outside of the shield for the new design than the previous. The field for both coils drops to the order of μT within 10cm of the shield. A full comparison of coil parameters is made in **Table 3.1**.

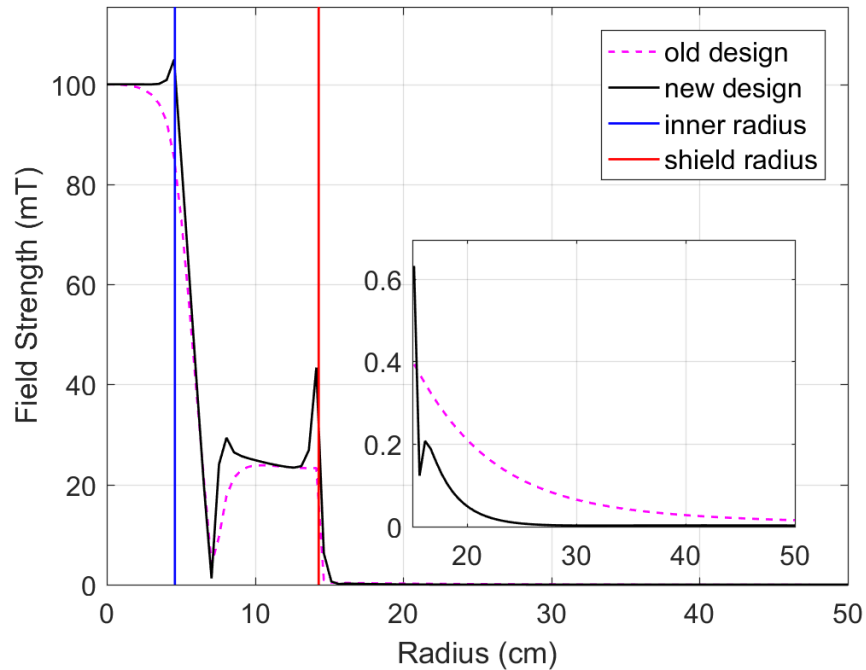


Figure 3.5. Simulated field strengths of the previously constructed coil (magenta dashed) and newly designed coil (black solid), against radius from their central axis in the $Z = 0$ plane. This is where the field produced by the system should be the strongest. Inner and outer (shield) radii are denoted by the blue and red lines respectively. A magnified plot is provided of field strength from 15cm to 50cm, with axes still in cm and mT.

Table 3.1. Geometric and Electromagnetic Parameters of Coil Designs

Parameters	Old Design Method	New Design Method
Inner Radius (cm)	4.6	4.6
Shield Radius (cm)	14.3	14.3
Radial Layers	6	6
Axial Windings	30	36
Gap Width (cm)	1.25	0
Solenoid Axial Length (cm)	18.5	18.5
Shield Axial Length (cm)	31.4	31.2
Resistance (m Ω)	80.3	103.4
Inductance (μ H)	1478	2112
Efficiency (mT/A)	0.90	1.05
DSV<1% ^a (cm)	5.0	8.5

Table 3.1. Geometric design parameters and resulting simulated electromagnetic properties of previously constructed coil design and coil designed with new method. ^aDSV<1% refers to the diameter of a spherical volume within which the inhomogeneity is less than 1%.

The coil designs were applied to simulated dreMR subtraction images to see the improvement the new method can have on an image. The resulting percent differences from a perfectly homogeneous field image across the domain of VivoTrax for the previously constructed and newly designed coils can be found in **Figure 3.6 (a)** and **(b)**. Histograms of these percent differences are given in fraction of pixels in **Figure 3.6 (c)** and **(d)**.

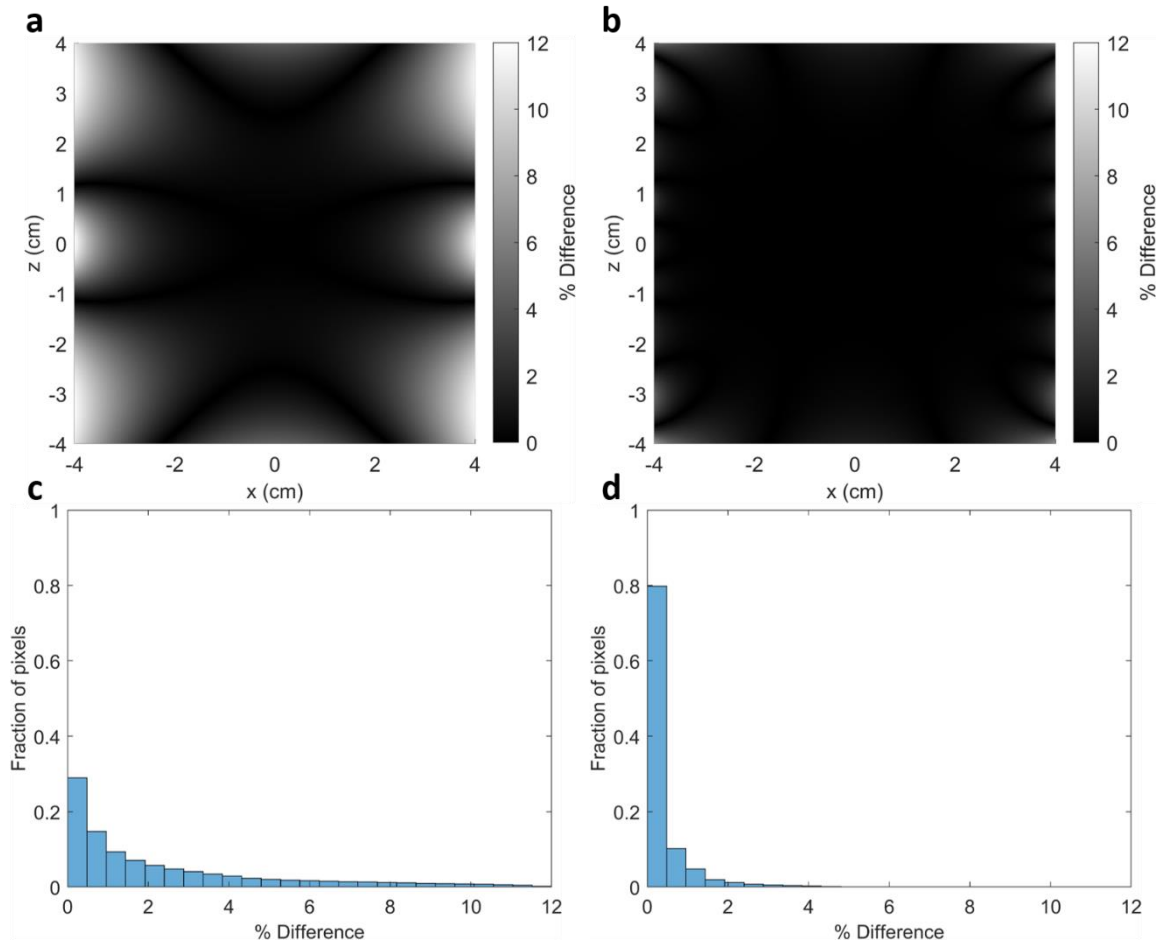


Figure 3.6. Percent differences of simulated dreMR subtraction images between coil design fields and ideal homogenous field in the XZ-plane. **(a)** Percent difference between simulated image with previously designed coil and with ideal field. **(b)** Percent difference between simulated image with newly designed coil and with ideal field. Histograms of percent difference with a perfectly homogeneous simulation given in fraction of pixels for **(c)** current generation design and **(d)** new design. Domain contains uniform $160\mu\text{M}$ VivoTrax with relaxivity data obtained from collaborators.

The result of a dreMR subtraction on the domain of VivoTrax, fat, and blood at a main field strength of 0.5T is shown in **Figure 3.7** for the two coil designs. Line profiles across the diagonal of the domain are shown in **Figure 3.7 (c)** and **(d)**. Histograms of percent difference between coil designs and a perfectly homogenous field shift are given as fraction of dispersive pixels in **Figure 3.7 (e)** and **(f)**. Using the current generation design, 40% of pixels had a percent error of $\leq 1\%$, 5% of pixels had a percent error of $\geq 10\%$,

and the maximum error was 22%. Using the new design, 93% of pixels had a percent error of $\leq 1\%$, no pixels had a percent error of $\geq 10\%$, and the maximum error was 5%.

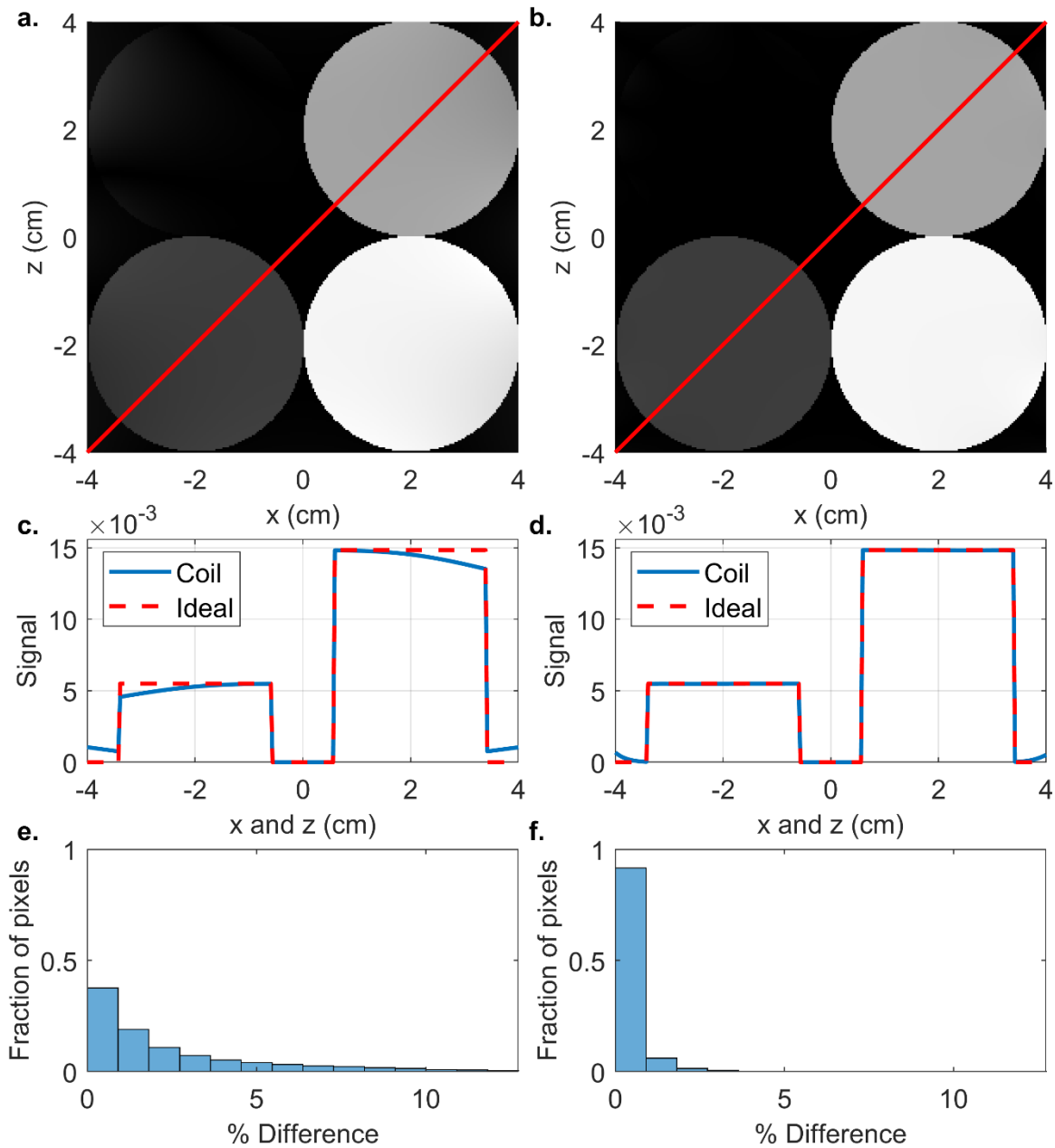


Figure 3.7. Simulated dreMR subtraction imaging with coil design field maps for (a) current generation dreMR coil design and (b) analogous design using the improved homogeneity method. VivoTrax agent used at $B_0 = 0.5\text{T}$, $\Delta B = 0.1\text{T}$, and a flat top duration of 100ms. Red arrow denotes line profiles plotted in (c) for current generation design and (d) for new design. Histograms of percent difference with a perfectly homogeneous simulation given in fraction of dispersive pixels for (e) current generation design and (f) new design.

The result of a symmetric dreMR subtraction on the domain of Ablavar, fat, and blood at a main field strength of 0.3T is shown in **Figure 3.8** for the two coil designs. Line profiles across the diagonal of the domain are shown in **Figure 3.8 (c)** and **(d)**. Histograms of percent difference between coil designs and a perfectly homogenous field shift are given as fraction of dispersive pixels in **Figure 3.8 (e)** and **(f)**. Using the current generation design, 15% of pixels had a percent error of $\leq 1\%$, 25% of pixels had a percent error of $\geq 10\%$, and the maximum error was 50%. Using the new design, 79% of pixels had a percent error of $\leq 1\%$, only 0.04% of pixels had a percent error of $\geq 10\%$, and the maximum error was 12%.

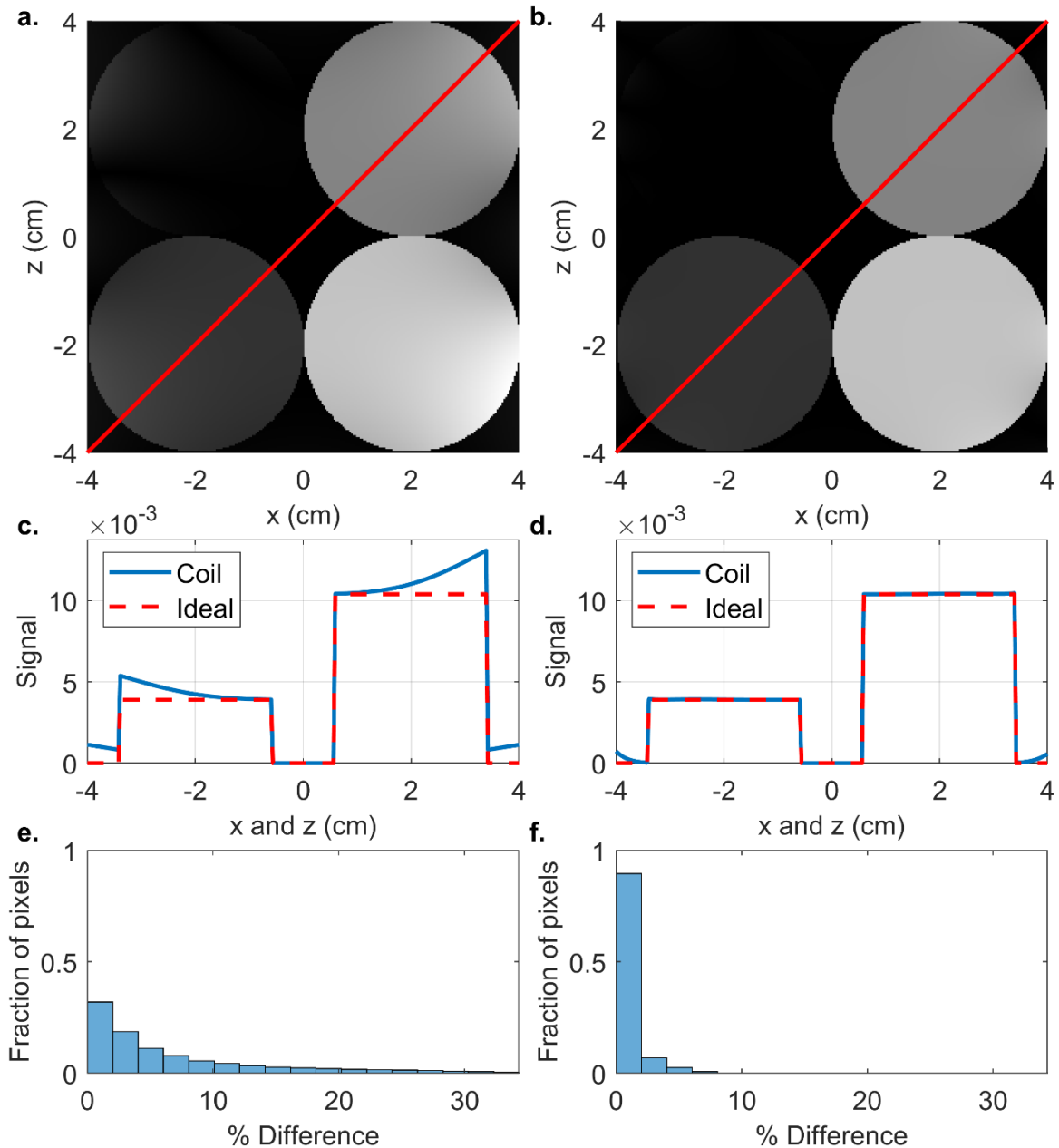


Figure 3.8. Simulated dreMR subtraction imaging with coil design field maps for (a) current generation dreMR coil design and (b) analogous design using the improved homogeneity method. Ablavar agent used at $B_0 = 0.3\text{T}$, $\Delta B = 0.1\text{T}$, and a flat top duration of 100ms. Red arrow denotes line profiles plotted in (c) for current generation design and (d) for new design. Histograms of percent difference with a perfectly homogeneous simulation given in fraction of dispersive pixels for (e) current generation design and (f) new design.

The result of an asymmetric dreMR subtraction on the domain of Ablavar, fat, and blood at a main field strength of 0.5T is shown in **Figure 3.9** for the two coil designs. Line profiles across the diagonal of the domain are shown in **Figure 3.9** (c) and (d). Histograms

of percent difference between coil designs and a perfectly homogenous field shift are given as fraction of dispersive pixels in **Figure 3.9 (e)** and **(f)**. Using the current generation design, 6% of pixels had a percent error of $\leq 1\%$, 48% of pixels had a percent error of $\geq 10\%$, and the maximum error was 114%. Using the new design, 63% of pixels had a percent error of $\leq 1\%$, only 3% of pixels had a percent error of $\geq 10\%$, and the maximum error was 26%.

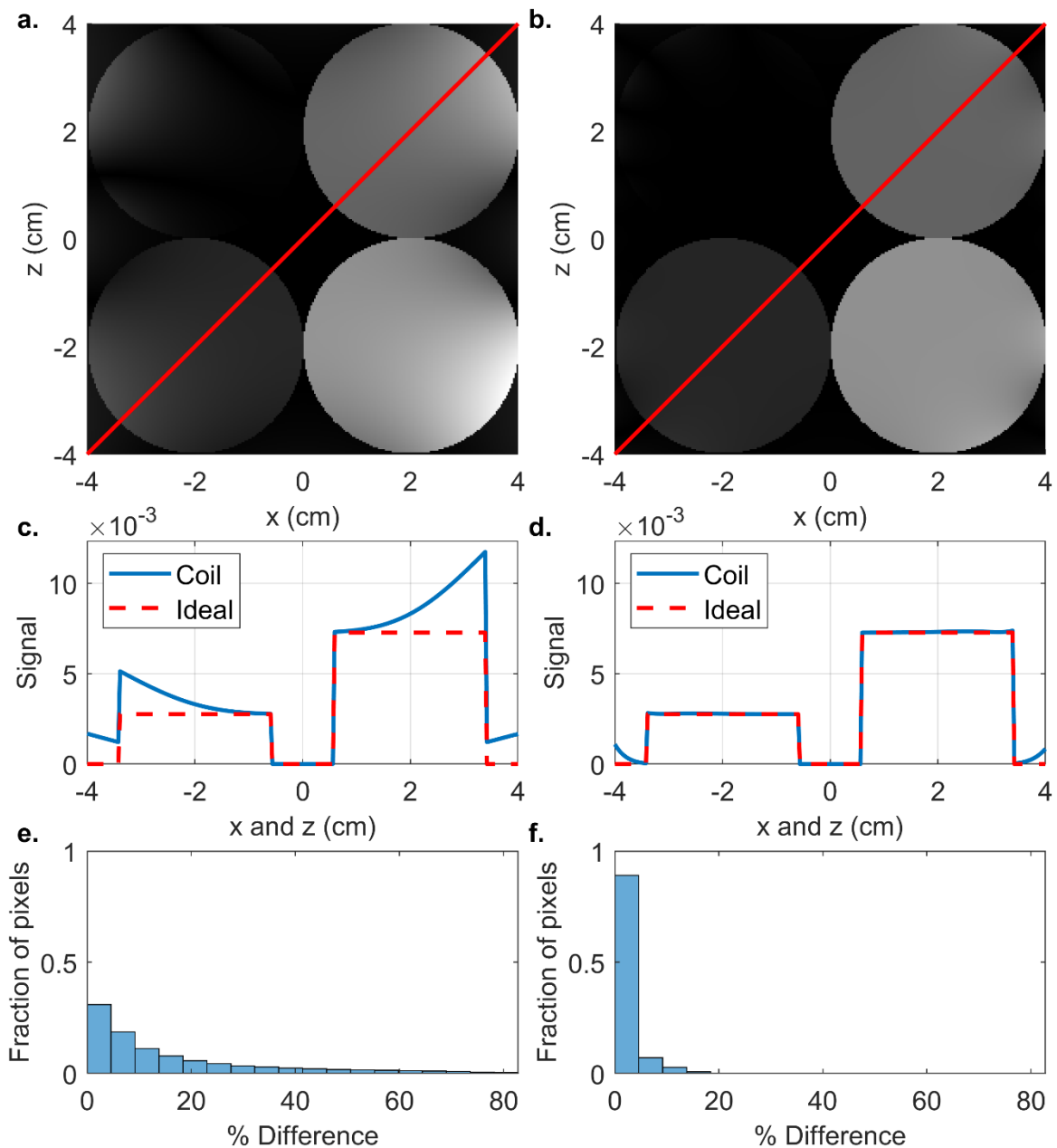


Figure 3.9. Simulated dreMR subtraction imaging with coil design field maps for **(a)** current generation dreMR coil design and **(b)** analogous design using the improved homogeneity method. Ablavar agent used at $B_0 = 0.5\text{T}$, with an asymmetric dreMR pulse $\Delta B = [0\text{T}, 0.2\text{T}]$, and a flat top duration of 100ms.

Red arrow denotes line profiles plotted in (c) for current generation design and (d) for new design. Histograms of percent difference with a perfectly homogeneous simulation given in fraction of dispersive pixels for (e) current generation design and (f) new design.

3.3.2 Explicit control of imaging region

To showcase the new design method's ability to move the ROI, a shielded uniform solenoid with and without a correction coil were designed and their field homogeneity maps compared. **Figure 3.10** shows the homogeneity contour maps of the ROI-shifted design and the shielded solenoid. Inhomogeneity here is calculated in reference to a point on the z-axis at $z = 5\text{cm}$. **Figure 3.10 (a)** and **(b)** show homogeneity maps for the shielded solenoid in the XY and XZ planes respectively. **Figure 3.10 (c)** and **(d)** show homogeneity maps for the ROI-shifted coil in the XY and XZ planes respectively. It can be seen that the correction coil design has far greater homogeneity in the ROI than the solenoid.

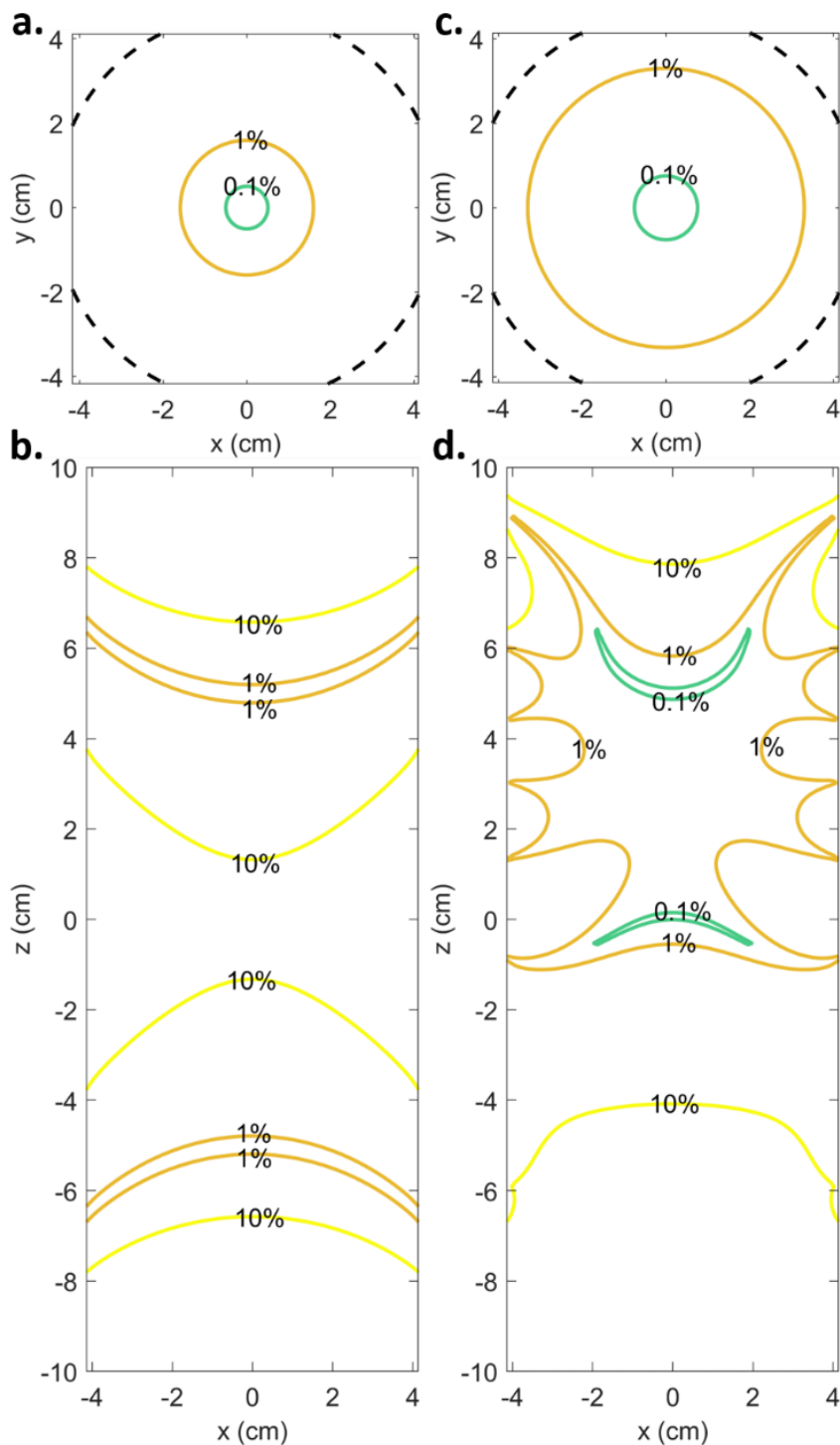


Figure 3.10. Inhomogeneity contour maps for (a) a simple shielded solenoid in the XY plane at $Z = 5\text{cm}$, (b) the shielded solenoid in the XZ plane, (c) the newly designed coil in the XY plane at $Z = 5\text{cm}$, and (d) the new design in the XZ plane. Both coils have an inner radius of 4.6cm , represented by the dashed black line in the XY plane.

3.4 Discussion

The improved design method was shown to greatly increase the field shift homogeneity of the imaging region and increase the available size of the imaging region. In the new example design provided, nearly the entire diameter of the coil can be imaged with <1% field inhomogeneity for the center plane. While the resistance increased by approximately 29% in the new design, the field efficiency also increased by approximately 17%, resulting in a 5.4% drop in power requirements. This has come at a cost to inductance and therefore slew rate, all due to the added windings filling the axial gap of the previous design and the introduction of the correction windings. While the shielding was not expected to improve for this design method, we can see that the field drops off quicker for our new design outside the shield than for the previous design. This may be specific to the design; however, the results do demonstrate that the new design method maintains adequate shielding.

In a simulation of dreMR subtraction imaging, the new coil was found to dramatically improve precision and accuracy when compared to the previous design. The percent difference calculated across a domain of uniform concentration VivoTrax was shown to reach values up to 12% for the previous design, and values up to 6.5% for the new design with the vast majority of the domain falling below 1%. For the domains of various agent concentrations and fat (**Figure 3.7**, **Figure 3.8**, and **Figure 3.9**) the new design greatly reduced the remaining signal due to fat, and closely matched the simulated results of a perfectly homogeneous field shift. The majority of dispersive pixels for these simulations fell under a <1% difference from the perfectly homogeneous case for the new design, while the majority fell over >1% for the current generation design with a significant portion falling over >10%.

The new design method was shown to allow for explicit control of imaging region, shifting the ROI by 5cm along the z-axis in the example design, and largely improving homogeneity in this ROI versus a simple shielded solenoid. While it is very difficult to expand the ROI along the z-axis away from the coil isocenter where field begins to decrease with $\sim 1/z^2$, the new design was able to greatly correct the field towards isocenter.

3.5 Conclusions

To improve specificity of dreMR images and compete with nuclear imaging modalities, we have mitigated imaging errors due to field shift inhomogeneities. This was done by improving field homogeneity at the design stage through use of the BEM. A field-corrective layer of windings was designed to correct field inhomogeneities of a primary solenoid and coupled with an outer shield to prevent interaction with external systems while maintaining high field homogeneity. All coil layers were designed to run in series.

While dreMR has been demonstrated in animal studies it has not yet been performed in a clinical study. To develop coils for human imaging we will need to not only increase imaging region sizes, but potentially design shifted coils for imaging the head without space for shoulders, or a knee without space for the upper thigh. Having explicit control over field homogeneity allows for designs with a shifted ROI, making dreMR or general FCC imaging of such areas possible. The improved design method was shown to greatly increase the ROI, improve accuracy of simulated images at low field, and control location of ROI. This design method will be useful for the construction of future generation dreMR coils and specifically the first clinical dreMR coils.

3.6 References

- [1] J.K. Alford, B.K. Rutt, T.J. Scholl, W.B. Handler, B.A. Chronik, Delta relaxation enhanced mr: Improving activation - Specificity of molecular probes through R1 dispersion imaging, *Magn. Reson. Med.* 61 (2009) 796–802.
<https://doi.org/10.1002/mrm.21933>.
- [2] U.C. Hoelscher, S. Lothar, F. Fidler, M. Blaimer, P. Jakob, Quantification and localization of contrast agents using delta relaxation enhanced magnetic resonance at 1.5 T, *Magn. Reson. Mater. Physics, Biol. Med.* 25 (2012) 223–231.
<https://doi.org/10.1007/s10334-011-0291-6>.
- [3] M. Bödenler, M. Basini, M.F. Casula, E. Umut, C. Gösweiner, A. Petrovic, D. Kruk, H. Scharfetter, R1 dispersion contrast at high field with fast field-cycling MRI, *J. Magn. Reson.* 290 (2018) 68–75.

<https://doi.org/10.1016/j.jmr.2018.03.010>.

- [4] Y.T. Araya, F. Martínez-Santesteban, W.B. Handler, C.T. Harris, B.A. Chronik, T.J. Scholl, Nuclear magnetic relaxation dispersion of murine tissue for development of T1 (R1) dispersion contrast imaging, *NMR Biomed.* 30 (2017) 1–10. <https://doi.org/10.1002/nbm.3789>.
- [5] J.K. Alford, T.J. Scholl, W.B. Handler, B.A. Chronik, Design and construction of a prototype high-power B0 insert coil for field-cycled imaging in superconducting MRI systems, *Concepts Magn. Reson. Part B Magn. Reson. Eng.* 35 (2009) 1–10. <https://doi.org/10.1002/cmr.b.20132>.
- [6] C.T. Harris, W.B. Handler, T.J. Scholl, B.A. Chronik, A practical insert design for dreMR imaging in the human head, *Proc. 19th Sci. Meet. Int. Soc. Magn. Reson. Med.* (2011) 1839.
- [7] C.T. Harris, W.B. Handler, Y. Araya, F. Martinez-Santesteban, J.K. Alford, B. Dalrymple, F. Van Sas, B.A. Chronik, T.J. Scholl, Development and optimization of hardware for delta relaxation enhanced MRI, *Magn. Reson. Med.* 72 (2014) 1182–1190. <https://doi.org/10.1002/mrm.25014>.
- [8] N. Chanet, G. Guillot, G. Willoquet, L. Jourdain, R.M. Dubuisson, G. Reganha, L. De Rochefort, Design of a fast field-cycling magnetic resonance imaging system, characterization and methods for relaxation dispersion measurements around 1.5 T, *Rev. Sci. Instrum.* 91 (2020). <https://doi.org/10.1063/1.5128851>.
- [9] U.C. Hoelscher, P.M. Jakob, Eddy current compensation for delta relaxation enhanced MR by dynamic reference phase modulation, *Magn. Reson. Mater. Physics, Biol. Med.* 26 (2013) 249–259. <https://doi.org/10.1007/s10334-012-0335-6>.
- [10] M.A. McCready, W.B. Handler, F. Martínez-Santesteban, T.J. Scholl, B.A. Chronik, Inhomogeneity and ramping effects in field-cycled quantitative molecular MRI, *Proc. 29th Sci. Meet. Int. Soc. Magn. Reson. Med.* (2021) 2744.
- [11] Broche LM, Ross PJ, Davies GR, MacLeod MJ, Lurie DJ, A whole-body Fast

- Field-Cycling scanner for clinical molecular imaging studies, *Sci. Rep.* 9 (2019) 1–11. <https://doi.org/10.1038/s41598-019-46648-0>.
- [12] C.T. Harris, Optimization of a Boundary Element Approach To Electromagnet, *Sch. Grad. Postdr. Stud. Univ. West. Ontario.* (2013).
- [13] C.T. Harris, J.K. Alford, W.B. Handler, T.J. Scholl, B.A. Chronik, Bo coil designs for in vivo delta relaxation enhanced MR in humans, *Proc. 18th Sci. Meet. Int. Soc. Magn. Reson. Med.* (2010) 1548.
- [14] R.A. Lemdiasov, R. Ludwig, A stream function method for gradient coil design, *Concepts Magn. Reson. Part B Magn. Reson. Eng.* 26 (2005) 67–80. <https://doi.org/10.1002/cmr.b.20040>.
- [15] G.N. Peeren, Stream function approach for determining optimal surface currents, *J. Comput. Phys.* 191 (2003) 305–321. [https://doi.org/10.1016/S0021-9991\(03\)00320-6](https://doi.org/10.1016/S0021-9991(03)00320-6).
- [16] M. Poole, R. Bowtell, Novel gradient coils designed using a boundary element method, *Concepts Magn. Reson. Part B Magn. Reson. Eng.* 31B (2007) 162–175. <https://doi.org/10.1002/cmr.b.20091>.
- [17] S. Kruber, G. Farrher, E. Anorado, New magnet design for fast-field-cycling nuclear magnetic resonance, *IEEE Lat. Am. Trans.* 11 (2013) 251–256. <https://doi.org/10.1109/TLA.2013.6502812>.
- [18] D.B. Montgomery, *Solenoid Magnet Design: The Magnetic and Mechanical Aspects of Resistive and Superconducting Systems*, WILEY-INTERSCIENCE, New York, 1969.
- [19] C.T. Harris, D.W. Haw, W.B. Handler, B.A. Chronik, Shielded resistive electromagnets of arbitrary surface geometry using the boundary element method and a minimum energy constraint, *J. Magn. Reson.* 234 (2013) 95–100. <https://doi.org/10.1016/j.jmr.2013.06.010>.
- [20] C.T. Harris, W.B. Handler, B.A. Chronik, Electromagnet design allowing explicit and simultaneous control of minimum wire spacing and field uniformity, *Concepts*

Magn. Reson. Part B Magn. Reson. Eng. 41B (2012) 120–129.
<https://doi.org/10.1002/cmr.b.21220>.

Chapter 4

Conclusions and future work

4.1 Thesis summary

Quantitative molecular imaging is a useful tool in assessment of disease treatment and progression. With use of the dreMR method, quantitative molecular images can be obtained from MRI without effects of ionizing radiation from nuclear imaging such as PET [1,2]. Thus far dreMR has only been performed in animals and phantoms, with the exception of one case where a broken finger was imaged [3]. Extending dreMR to clinical studies will require maximization of ROI relative to coil size, and increasing contrast generated per unit field shift. It is therefore also favourable to perform dreMR imaging with low field systems in the future where many of the agents used display higher dispersion [4]. The work presented in this thesis focused on removing the previously made assumptions of dreMR that the FFC insert coil ramps to field instantaneously and provides a perfectly homogeneous field shift. These factors were then discussed in the context of extension to low field and clinical imaging, and solutions posed in the form of feasibility of fast ramping and an improved homogeneity design method.

In Chapter 2 the standard dreMR subtraction model was rederived twice, once for finite ramping periods, and once for inhomogeneous field shifts. It was shown that both effects result in residual signal from non-dispersive tissue, and a loss of proportionality to dispersive agent concentration. A simulation environment was developed to predict the impact of these effects on dreMR imaging for a given dreMR pulse and coil design if desired. Such simulations may be used to inform insert coil design studies going forward as to the required slew rate and field homogeneity capabilities for a desired agent, pulse, and main field strength.

Development of dreMR coils for imaging humans will require larger designs and therefore higher inductances than previously constructed coils. The simulations of Chapter 2 will therefore be crucial to inform us of slew rate restrictions that must be met as we approach these limits. Our current gradient power amplifier is capable of ramping dreMR

coils at the necessary slew rates, and a study of induced heating with our compact main magnet determined that there is no danger of a quench with our current degree of shielding. The ability to reach slew targets will likely then be limited by PNS and cardiac stimulation in humans [5].

Another concern for developing human sized dreMR coils is the available space within the system. As the dreMR coil is an insert to the gradient system, its outer shield radius must fit within the gradient bore. At the same time, the dreMR system must fit the RF system and the patient comfortably within. This is further complicated by the field homogeneity requirements resulting from the work of Chapter 2. To image humans without inhomogeneity complications a large region of $<1\%$ inhomogeneity is necessary. Field inhomogeneities can be accounted for by detailed field mapping and post processing, or ideally at the source by an improved design method which also minimizes inhomogeneity impact on motion effects.

The simplest way to increase the ROI at the design stage is to construct a larger coil, but this of course isn't viable to fit within the gradient system and would also increase the coil's inductance. In Chapter 3, field homogeneity was improved at the design stage through use of the BEM. A field-corrective layer of windings was designed to correct field inhomogeneities of a primary solenoid and coupled with an outer shield to prevent interaction with external systems while maintaining high field homogeneity. All coil layers were designed to run in series. This new method was shown to greatly increase the usable ROI, reducing signal due to fat and removing inconsistencies in signal due to agent. It was also shown to allow for shifted ROI designs.

These improvements will increase specificity of dreMR images to compete with nuclear imaging modalities. They will also aid in the design of clinical dreMR coils by maximizing the available imaging volume. This will allow for the development of compact human sized coils with low inductance mitigating errors due to field inhomogeneities and finite ramping periods. With a clinical dreMR coil, dreMR could be used for diagnosis of disease, and assessment of disease treatment and progression, all without use of ionizing radiation.

4.2 Future work

4.2.1 Additional post-processing dreMR methods

As discussed in Chapter 2, one method for removing field shift inhomogeneity effects from dreMR images would be to use detailed field maps for the field compensation weightings. As the remaining non-dispersive signal and loss of proportionality to contrast agent arise from a difference in the field used for these weightings and the exact local field in some region, making these weights spatially dependent with the coil's real field map would ideally remove these errors. A field map for a prototype dreMR coil was previously measured using a 3-axis Hall probe (Senis AG, Model F3A) and rigid positioning apparatus [6]. These measurements should be repeated for one of the currently operating dreMR coils and used in image post-processing to validate the expected improvement. There will of course remain some error due to uncertainty in field mapping measurements and in a practical clinical imaging experiment patient motion would introduce inhomogeneity effects not accounted for by the field map. An improved design method for high homogeneity dreMR systems is therefore more desirable and should be combined with detailed field mapping.

Much of the loss of differentiation between dispersive agent and non-dispersive tissue in Chapter 2 occurred when high R_1 tissues were present such as fat, white matter, and grey matter. When these tissues are not present, the requirements for field inhomogeneity and slew rate for differentiation are much less stringent. A tissue atlas could then be used to determine whether a region is likely to contain certain high R_1 tissues. Such an approach may also lend itself to the use of artificial intelligence to determine whether a signal is coming from contrast agent or non-dispersive tissue as a part of image post-processing. While this could ease the design requirements, it would still be ideal to produce high homogeneity and rapid field shifts as the loss of proportionality to contrast agent concentration would not be corrected by this method.

4.2.2 Asymmetric dreMR pulses

In section 3.2.5 a more realistic simulation of dreMR imaging with Ablavar at low field was presented. Ablavar has been the flagship contrast agent of dreMR in the past thanks to its attractive ability to only exhibit T_1 dispersion when bound to the target molecule. However, at 0.5T bound Ablavar exhibits a local maximum in its relaxivity. A standard set of dreMR pulses for subtraction is symmetric. That is, the pulses are applied with the same magnitude but opposite polarity. Not only does this violate the linear relaxivity assumption at 0.5T for Ablavar but given the shape of the curve the relaxivity at $B_0 \pm \Delta B$ will be the same resulting in no signal from the agent after subtraction. Therefore, in order to perform dreMR subtraction with Ablavar in our low field system an asymmetric pulse structure must be used, where two pulses of the same polarity but different size are applied for subtraction (i.e. $\pm\Delta B_1$ and $\pm\Delta B_2$).

All derivations in this work and in previous work on dreMR followed use of symmetric dreMR pulses. While it is likely that asymmetric pulses will maintain the desired properties of dreMR and only slightly alter effects of inhomogeneities and ramping periods, the derivation of dreMR subtraction should be repeated for asymmetric pulses before experimentation. This will determine if any additional post processing needs to be applied for the use of such pulse sequences.

4.2.3 Extensions to design method

The implementation of the BEM allows for the extension of this design method to provide multiple layers (surfaces) for correction coils. Under slight adjustment, designs could be produced with not only an inner correction coil, but additional correction windings outside the primary solenoid. This would allow for finer control of field homogeneity as these outer windings would have less impact on the imaging region than the inner ones. While we have been able to adequately control homogeneity in the small coil designs of this work, such additional layers could prove useful in larger human coil designs.

The BEM is also used extensively in the design of gradient coil systems. Thus far, dreMR coils have been inserted within gradient systems and must be designed to fit within

their bore. This could be difficult when designing human sized coils for clinical dreMR imaging. A potential solution is to couple the design of dreMR and gradient systems into one combined system using the BEM. This would require accounting for torques and forces within the systems which the BEM is capable of.

This could be extended to allow the z-gradient and dreMR coil to apply pulses simultaneously during the pre-polarization period (Figure 4.1). While many z-gradients vary linearly from $-B_z$ to $+B_z$ across the ROI, passing through zero, offset gradients have been designed which produce a field of one sign in the ROI and do not pass through zero [7]. Such an offset z-gradient could be used to increase the dreMR field shift across the ROI and thereby reduce the number of windings required for the dreMR coil. This could in turn improve ramping speeds if the systems were run in parallel.

The addition of a linearly varying component would require detailed field mapping for realistic field compensation weightings, or could be accounted for in the design of the correction coil(s). A pattern mirroring that of the offset z-gradient could be used to produce a field with the opposite slope which when added to the z-gradient field would produce a flat homogenous field across the ROI. The stream function for such a design could be scaled and added to one chosen to correct the dreMR system field, similar to how the separate shield stream functions were calculated and added together in Chapter 3.

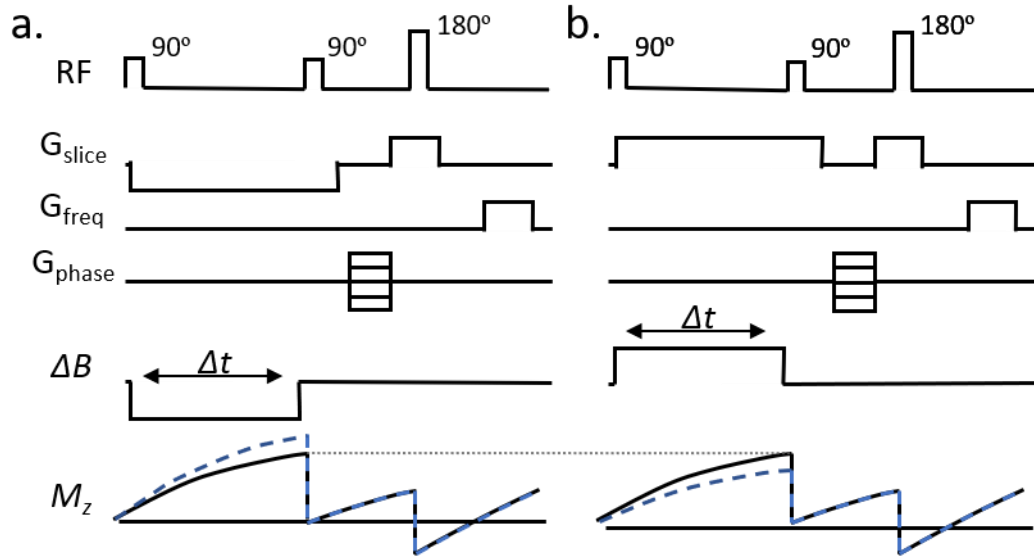


Figure 4.1. Gradient assisted pre-polarization dreMR subtraction pulse sequence. The slice select (z) gradient is applied simultaneously with the dreMR pulse and remains on for the slice selection during the second 90° RF pulse. The gradient is applied in the same direction as the dreMR pulse meaning the current must be reversed between the (a) $-\Delta B$ and (b) $+\Delta B$ images.

4.2.4 Design studies and construction of coils

The design method outlined in this thesis will be applied to a design study and used to construct future dreMR coils. The simulation environment developed in Chapter 2 can be used to inform this study for the desired use. Simulations will then be carried out in CST Studio Suite (Dassault Systèmes Simulia Corp., RI) using the model of our previous dreMR coil, and any potential new designs. These simulations will involve calculating the eddy currents induced on the surface of our 0.5T bore system, and ensuring that any new design does not produce greater eddy currents during ramping than our previous coil does for the case we measured the temperature of (Appendix B). This test will allow us to ensure our new design will not overheat the bore system and cause a quench. This will also allow us to find any necessary restrictions on the slew rate we can run a new design at.

Such design studies will be carried out first for a small animal coil to confirm the improvement on imaging. This coil can then be used for the first dreMR imaging experiments at 0.5T. If the coil performs as desired, design studies should be carried out

for the first human sized dreMR coils, the construction of which will finally push this powerful imaging method to clinical application.

4.3 References

- [1] J.K. Alford, B.K. Rutt, T.J. Scholl, W.B. Handler, B.A. Chronik, Delta relaxation enhanced mr: Improving activation - Specificity of molecular probes through R1 dispersion imaging, *Magn. Reson. Med.* 61 (2009) 796–802.
<https://doi.org/10.1002/mrm.21933>.
- [2] I.J. Hildebrandt, H. Su, W.A. Weber, Anesthesia and other considerations for in vivo imaging of small animals, *ILAR J.* 53 (2012) 17–26.
- [3] J. Alford, A.G. Sorensen, T. Benner, A. Chronik, B. Handler, J. Scholl, G. Madan, P. Caravan, Direct Protein Imaging of Inflammation in the Human Hand, *Proc. 19th Sci. Meet. Int. Soc. Magn. Reson. Med.* (2011) 0452.
- [4] Y. Wang, M. Spiller, P. Caravan, Evidence for weak protein binding of commercial extracellular gadolinium contrast agents, *Magn. Reson. Med.* 63 (2010) 609–616. <https://doi.org/10.1002/mrm.22214>.
- [5] Medical electrical equipment — Part 2-33: Particular requirements for the basic safety and essential performance of magnetic resonance equipment for medical diagnosis, *Int. Electrotech. Comm.* 03 (2010).
- [6] D.J. Martire, Optimization of Design Procedures for Delta Relaxation Enhanced Magnetic Resonance, *Sch. Grad. Postdr. Stud. Univ. West. Ontario.* (2018).
- [7] W.B. Handler, C.T. Harris, T.J. Scholl, D.L. Parker, K.C. Goodrich, B. Dalrymple, F. Van Sass, B.A. Chronik, New head gradient coil design and construction techniques, *J. Magn. Reson. Imaging.* 39 (2014) 1088–1095.
<https://doi.org/10.1002/jmri.24254>.

Appendices

A. Derivations of dreMR

The standard dreMR subtraction image is comprised of a field compensated difference of two T_1 weighted images pre-polarized at the field strengths $B_0 \pm \Delta B$ [1]. The signal in each image is proportional to the magnetization at the end of a dreMR pulse given by the solution to the longitudinal Bloch equation (Eq. (A.1)).

$$M_{z\pm} = M_0 \left(\frac{B_0 \pm \Delta B}{B_0} \right) (1 - e^{-\Delta t R_{1\pm}}) \quad 4.1$$

Here $M_{z\pm}$ is the longitudinal magnetization after the $\pm\Delta B$ pulse, Δt is the flat top duration of the pulse, and $R_{1\pm}$ is the longitudinal relaxation rate at the field strength $B_0 \pm \Delta B$. The resulting proportional signals are subjected to the dreMR field compensated subtraction (Eq. (A.2)).

$$I_{sub} = \left(\frac{B_0}{B_0 - \Delta B} \right) kM_{z-} - \left(\frac{B_0}{B_0 + \Delta B} \right) kM_{z+} \quad 4.2$$

When a T_1 dispersive agent is present with linear dispersion in the range of field shifts and the field shifts are instantaneous and perfectly homogeneous this results in a remaining signal proportional to concentration of dispersive agent [1]. In this appendix the previous derivation of dreMR will be repeated with finite ramping periods and inhomogeneous field shifts separately.

A.1. Derivation of dreMR with finite ramping periods

The field shift during the ramping period is given by the field efficiency of the coil (η) multiplied by the current for an RL circuit ramping up or down. If we make the safe assumption that the power amplifier is capable of providing a far greater voltage than required for the desired current ($V_{max} \gg IL$ and IR), the ramping current can be approximated as linear with time giving:

$$\Delta B(t) = \eta \frac{V}{R} \left(1 - e^{-\frac{Rt}{L}}\right) \approx \frac{\eta V}{L} t \quad 4.3$$

The time coefficient here $\eta V/L$ is the slew rate of the coil ξ . If we maintain that dispersion is linear within our range of field shifts the Bloch equation for longitudinal magnetization during the ramp-up period becomes:

$$\frac{dM_z}{dt} \approx (R_1 \pm R'_1 \xi t) \left[M_0 \left(\frac{B_0 \pm \xi t}{B_0} \right) - M_z \right] \quad 4.4$$

Here, R_1 is the local relaxation rate accounting for background tissue and dispersive agent at the main field strength B_0 , and R'_1 is the slope of the local relaxation rate in the range of the field shifts.

The ODE for this ramp up period (Eq. (A.4)) is first order linear, and can be solved by use of the integrating factor $\mu(t)$:

$$\frac{dM_z}{dt} \approx (R_1 \pm R'_1 \xi t) \left[M_0 \left(\frac{B_0 \pm \xi t}{B_0} \right) - M_z \right] \quad 4.5$$

Applying this integrating factor to our ODE and solving will result in a number of error functions which over complicate the results and remove any intuition they may give us for the behavior of the image. If we instead consider the eventual assumption that time spent ramping, and the second term of the exponent (Eq. (A.5)) will be small ($t \leq \Delta t_r \ll 1$) we can simplify $\mu(t)$ with a Taylor series to:

$$\mu(t) = \exp\left(R_1 t \pm \frac{1}{2} R'_1 \xi t^2\right) \approx e^{t R_1} (1 + R'_1 \xi t^2) \approx e^{t R_1} \quad 4.6$$

Applying this integrating factor to both sides of our Bloch equation (Eq. (A.4)), expanding, and continuing the assumption that ramping time is small results in the separable ODE:

$$\frac{d}{dt} \{M_z e^{R_1 t}\} \approx \frac{M_0}{B_0} (B_0 R_1 \pm \xi t R_1 \pm B_0 R'_1 \xi t) e^{t R_1} \quad 4.7$$

Integrating and rearranging then results in the general solutions:

$$M_z(t) \approx \frac{M_0}{B_0} \left[B_0 \pm \xi (B_0 R'_1 + R_1) \left(\frac{R_1 t - 1}{R_1^2} \right) \right] + C e^{-t R_1} \quad 4.8$$

where C is a constant of integration. Solving for C in terms of the initial condition and finally applying the assumption that ramping time is small to the exponential results in the solution:

$$M_z(t) \approx M_z(0) + R_1 t (M_0 - M_z(0)) \quad 4.9$$

This result is a linear growth of magnetization at the relaxation rate and equilibrium magnetization of the static main field strength B_0 .

Turning our attention to the ramp down period and maintaining linear dispersion and linear ramping, the Bloch equation for longitudinal magnetization becomes:

$$\frac{dM_z}{dt} \approx [R_1 \pm R'_1 (\Delta B - \xi t)] \left[M_0 \left(\frac{B_0 \pm \Delta B \mp \xi t}{B_0} \right) - M_z \right] \quad 4.10$$

Where the field with time is now of course $B_0 \pm (\Delta B - \xi t)$. The integrating factor here is given by:

$$\begin{aligned} \mu(t) &= \exp \left(\int (R_1 \pm R'_1 (\Delta B - \xi t)) dt \right) \\ &= \exp \left((R_1 \pm R'_1 \Delta B) t \mp \frac{1}{2} R'_1 \xi t^2 \right) \end{aligned} \quad 4.11$$

Using the definition that $R_{1\pm}$ is the approximate relaxation rate at the shifted field strength $(R_1 \pm R'_1 \Delta B)$ and the Taylor series approximation for small ramping time used in the previous integrating factor (Eq. (A.6)) we can obtain:

$$\mu(t) = \exp \left((R_1 \pm R'_1 \Delta B) t \mp \frac{1}{2} R'_1 \xi t^2 \right) \approx e^{t R_{1\pm}} \quad 4.12$$

Applying this integrating factor to both sides of our Bloch equation (Eq. (A.10)), expanding, and continuing the assumption that ramping time is small results in the separable ODE:

$$\frac{d}{dt} \{ M_z e^{t R_{1\pm}} \} \approx \frac{M_0}{B_0} \left[R_{1\pm} (B_0 \pm \Delta B) \mp \xi t (R_{1\pm} + R'_1 (B_0 \pm \Delta B)) \right] e^{t R_{1\pm}} \quad 4.13$$

Integrating and rearranging then results in the general solutions:

$$M_z(t) \approx \frac{M_0}{B_0} \left\{ (B_0 \pm \Delta B) \pm \xi [R_{1\pm} + R'_1(B_0 \pm \Delta B)] \left(\frac{t \cdot R_{1\pm} - 1}{R_{1\pm}^2} \right) \right\} + C e^{-t \cdot R_{1\pm}} \quad 4.14$$

where C is a constant of integration. Solving for C in terms of the initial condition and finally applying the assumption that ramping time is small to the exponential results in the solution:

$$M_z(t) \approx M_z(0) + t \cdot R_{1\pm} \left[M_0 \left(\frac{B_0 \pm \Delta B}{B_0} \right) - M_z(0) \right] \quad 4.15$$

Much like the ramp-up result, this result is a linear growth of magnetization. However, it now uses the relaxation rate and equilibrium magnetization of the field strength during shift $B_0 \pm \Delta B$.

We now use these solutions to propagate through a full trapezoidal dreMR pulse. The initial condition is applied that longitudinal magnetization is nulled following a 90° RF pulse. The magnetization is then allowed to grow during the ramp up period for a duration Δt_r giving:

$$M_z(\Delta t_r) \approx M_0 \Delta t_r R_1 \quad 4.16$$

Propagating this solution through the standard longitudinal Bloch equation for a flat-top dreMR pulse (Eq. (A.1)) for a flat-top duration Δt_f and ignoring terms of $O(\Delta t_r^2)$, $O(\Delta t_f^2)$, $O(\Delta t_r \cdot \Delta t_f)$, and higher gives:

$$M_z(\Delta t_r + \Delta t_f) \approx M_0 \Delta t_r R_1 + M_0 \left(\frac{B_0 \pm \Delta B}{B_0} \right) \Delta t_f R_{1\pm} \quad 4.17$$

Applying the ramp down period solution to this result for another Δt_r and continuing to ignore nonlinear terms in time gives the final magnetization:

$$M_z(2\Delta t_r + \Delta t_f) \approx M_0 \Delta t_r R_1 + M_0 \left(\frac{B_0 \pm \Delta B}{B_0} \right) (\Delta t_r + \Delta t_f) R_{1\pm} \quad 4.18$$

If we now apply the standard field compensated dreMR subtraction (Eq. (A.2)) to the final magnetizations and simplify we get the result shown in Chapter 2:

$$I_{sub} \approx 2kM_0\Delta B \left[\left(\frac{B_0}{B_0^2 - \Delta B^2} \right) R_1 \Delta t_r - R_1' (\Delta t_r + \Delta t_f) \right] \quad 4.19$$

A.2. Derivation of dreMR with inhomogeneous field shifts

As shown in Chapter 2, we define some inhomogeneous field shift ΔB^* which we allow the magnetization to grow under giving the result:

$$M_{z\pm} = M_0 \left(\frac{B_0 \pm \Delta B^*}{B_0} \right) (1 - e^{-\Delta t \cdot R_{1\pm}^*}) \quad 1$$

where $R_{1\pm}^*$ is the relaxation rate during the inhomogeneous field shift (at $B_0 \pm \Delta B^*$). If we apply the weighted dreMR subtraction (Eq. (A.2)) to these magnetizations we will have different field shift values for the field compensation weights than the actual values used within the magnetization.

$$I_{sub} = \left(\frac{B_0}{B_0 - \Delta B} \right) kM_{z-}^* - \left(\frac{B_0}{B_0 + \Delta B} \right) kM_{z+}^* \quad 2$$

If we assume once more that relaxivity is linear with field strength, and use the definition that ΔR^* is the inhomogeneous change in longitudinal relaxation rate ($R_1' \Delta B^*$) then we can express the dreMR subtraction as:

$$I_{sub} \approx kM_0 \left[\left(\frac{B_0 - \Delta B^*}{B_0 - \Delta B} \right) (1 - e^{-\Delta t R_1} e^{\Delta t \Delta R^*}) - \left(\frac{B_0 + \Delta B^*}{B_0 + \Delta B} \right) (1 - e^{-\Delta t R_1} e^{-\Delta t \Delta R^*}) \right] \quad 3$$

Assuming $\Delta t \cdot R_1$ and $\Delta t \cdot \Delta R^*$ are small to ignore second order and higher terms allows us to simplify the expression to:

$$I_{sub} \approx \frac{2kM_0\Delta t}{B_0^2 - \Delta B^2} [B_0(\Delta B - \Delta B^*)R_1 - \Delta B^*(B_0^2 - \Delta B^*\Delta B)R_1'] \quad 4$$

The first term in this expression is independent of any dispersion and will appear for non-dispersive tissue. As signal is absolute, the difference in ideal and inhomogeneous field

shift can be written as inhomogeneity (H) which the non-dispersive signal is proportional to.

$$I_{sub0} \approx \frac{2kM_0B_0\Delta t}{B_0^2 - \Delta B^2} (\Delta B - \Delta B^*) R_1 \approx \frac{2kM_0B_0\Delta B\Delta t}{B_0^2 - \Delta B^2} R_1 \left(\frac{H}{100} \right) \quad 5$$

B. Operation of dreMR insert in compact low-field system

The following section is adapted from the peer-reviewed conference abstract [2]: McCready, M.A., Handler, W.B., Chronik, B.A. Measuring induced heating of low-field superconducting system during field-cycling pulse sequences. Proc. 29th Sci. Meet. Int. Soc. Magn. Reson. Med. (2021) 2483.

Delta relaxation enhanced magnetic resonance (dreMR) is a field-shifting quantitative molecular imaging method. The dreMR method is expected to produce higher contrast images at low-fields. Our low-field system has a small bore and may interact more strongly with the dreMR system causing a quench. No investigation of induced heating within the bore has been carried out for dreMR. Here, we investigate this interaction with our 0.5T superconducting system and find that dreMR pulse sequences do not cause significant heating in the magnet. We therefore state that dreMR is safe to carry out in such systems without quenching the magnet.

B.1. Measuring induced heating of low-field superconducting system during field-cycling pulse sequences

INTRODUCTION: Current medical imaging trends show a growing need for quantitative molecular imaging in preclinical studies. Thus far, positron emission tomography (PET) has been the prevailing method but has an associated radiation dose resulting in undesirable effects in longitudinal studies [3]. Delta relaxation enhanced magnetic resonance (dreMR or “dreamer”) is a contrast-enhanced MRI method for quantitative molecular imaging. dreMR uses a B_0 insert coil to shift the strength of the static field in a pulse preparation

phase of a pulse sequence. Using contrast agents with longitudinal relaxivity (r_1) dispersion, images taken at different field strengths can be subtracted, resulting in signal proportional to the concentration of these agents [1]. Many of these agents have high dispersion relations at low field, and it is expected that dreMR will therefore produce higher contrast images at such fields. To take advantage of this, we are currently preparing dreMR insert for use in a 0.5T cryogen-free superconducting magnet situated within our lab. This system has a smaller bore than previous scanners dreMR has been used with, so it is possible that coupling between the insert and the magnet will be higher and cause temperature-related stability issues or a quench due to induced eddy-current heating. While investigation has been made into compensating for eddy currents produced on a scanner bore for dreMR [4], this was with a focus on preventing image artifacts and not preventing a quench. Here we present an investigation into the heating of a 0.5T, compact, cryogen-free superconducting magnet for various dreMR pulse parameters.

METHODS: To investigate eddy-current induced heating in our 0.5T magnet, a previously constructed dreMR coil [5] was inserted at isocenter (**Figure 4.2**) and driven with a gradient power amplifier capable of a 900A peak current. Pulse parameters included ramp time, flat-top duration, pulse amplitude, and repetition time. Parameters of each pulse can be seen in Table B.1. These parameters were chosen to be extremes, intended to heat the 0.5T magnet more than a practical dreMR pulse sequence. Flat-top duration was varied to allow ramp-up eddy-currents to decay before ramping down. Pulse amplitude and ramp time were varied to change amplitude of induced eddy-currents. Repetition time was chosen to prevent overheating of the dreMR system and allow induced eddy-currents to decay. Each pulse sequence was run for approximately 5 minutes, until heating in the dreMR coil began to plateau. Temperature of the dreMR insert was measured through a National Instruments DAQ system connected to a thermocouple in contact with the shield coil, and output to a custom LabView program. Temperature of the 0.5T magnet was measured using a set of 9 temperature probes integrated with the coils of the system.

RESULTS: Temperature measurements for the superconducting magnet and the dreMR insert can be found in **Figure 4.3**. The pulses in this figure correspond to the parameters of

Table B.1. The simulated field strength of the dreMR insert in the superconducting bore for both pulse amplitudes is shown in **Figure 4.4**.

DISCUSSION: Looking at the temperature measurements in **Figure 4.3**, it can be seen that no significant heating was caused in the superconducting system by dreMR pulse sequences. Periods where the dreMR coil was running resulted in an increase in noise in the magnet’s temperature probes, but no perceivable upward trend. We can say with confidence that dreMR imaging may be carried out with a smaller, low-field system without danger of quenching the magnet. Future dreMR coils will be designed to shield as well as, if not better than, our current coil as seen in **Figure 4.4**.

CONCLUSION: The dreMR technique does not cause significant heating of a small-bore superconducting magnet. Images may be taken using dreMR with this low-field magnet without concern of a quench. Such low-field images are expected to exhibit higher contrast than previous 1.5T dreMR images, and further improve this quantitative molecular imaging modality.

Table B.1. dreMR Pulse Sequence Parameters						
Parameters	Pulse 1	Pulse 2	Pulse 3	Pulse 4	Pulse 5	Pulse 6
Ramp Time (ms)	5	5	2.5	1.3	1.3	1.3
Flat-Top (ms)	400	100	100	100	100	200
Repetition Time (ms)	2000	2000	2000	2000	1000	1000
Amplitude (V)	4	7	7	7	7	4
Amplitude (mT)	450	790	790	790	790	450

Table B.1. Pulse sequence parameters for driving dreMR insert coil during experiment. Pulses are trapezoidal, with equal time for ramping up and down. Pulses are numbered chronologically as they appear in **Figure 4.3**.



Figure 4.2. The dreMR insert coil (white) placed within our 0.5T cryogen-free superconducting magnet, so that their isocenters coincide. A gradient coil (green) is present but was not used during this experiment.

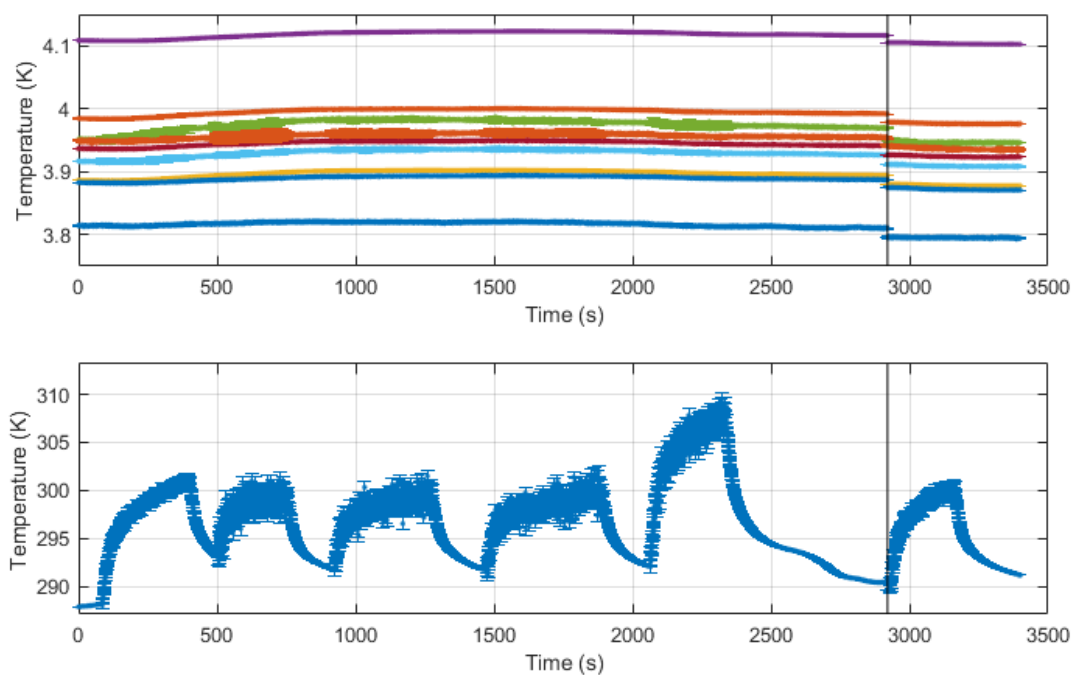


Figure 4.3. (TOP) Temperature profiles for multiple coils within the superconducting magnet. (BOTTOM) Temperature profile for our shield thermocouple within the dreMR insert. Each pulse corresponds to a set of parameters in Table B.1. Noise in superconducting temperatures increases during dreMR pulse sequences. A black vertical line denotes where a prolonged break was taken before returning to the experiment. No pulses were applied during the time that was removed.

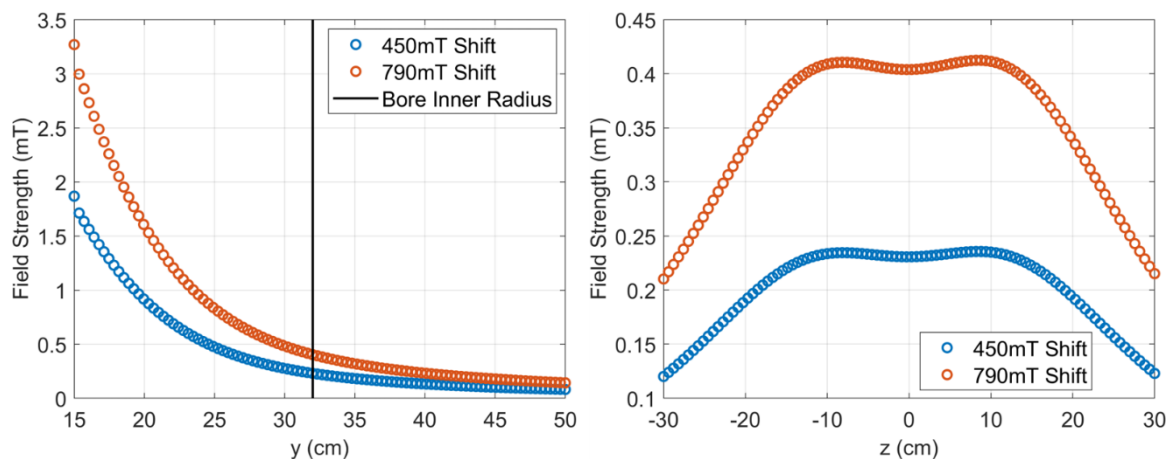


Figure 4.4. (LEFT) Field shift strength outside the dreMR coil for the two pulse amplitudes used during the experiment. Field decays due to distance and the active shield coil (at 15cm). A black vertical line denotes the inner radius of the superconducting magnet. **(RIGHT)** Field shift strength within the superconducting magnet at a radius of 64cm, across twice the length of the dreMR system. All values simulated using a numerical Biot-Savart Law calculator in MATLAB with our dreMR insert design.

C. References for appendices

- [1] J.K. Alford, B.K. Rutt, T.J. Scholl, W.B. Handler, B.A. Chronik, Delta relaxation enhanced mr: Improving activation - Specificity of molecular probes through R1 dispersion imaging, *Magn. Reson. Med.* 61 (2009) 796–802. <https://doi.org/10.1002/mrm.21933>.
- [2] M.A. McCready, W.B. Handler, B.A. Chronik, Measuring induced heating of low-field superconducting system during field-cycling pulse sequences, *Proc. 29th Sci. Meet. Int. Soc. Magn. Reson. Med.* (2021) 2483.
- [3] I.J. Hildebrandt, H. Su, W.A. Weber, Anesthesia and other considerations for in vivo imaging of small animals, *ILAR J.* 53 (2012) 17–26.
- [4] U.C. Hoelscher, P.M. Jakob, Eddy current compensation for delta relaxation enhanced MR by dynamic reference phase modulation, *Magn. Reson. Mater. Physics, Biol. Med.* 26 (2013) 249–259. <https://doi.org/10.1007/s10334-012-0335-6>.
- [5] C.T. Harris, W.B. Handler, Y. Araya, F. Martinez-Santesteban, J.K. Alford, B.

Dalrymple, F. Van Sas, B.A. Chronik, T.J. Scholl, Development and optimization of hardware for delta relaxation enhanced MRI, *Magn. Reson. Med.* 72 (2014) 1182–1190. <https://doi.org/10.1002/mrm.25014>.

Curriculum Vitae

Matthew McCready

Education:

- Doctor of Philosophy in Electrical Engineering** Sept 2021 – Present
Stanford University, Stanford, California
- Master of Science in Physics** Sept 2019 – June 2021
University of Western Ontario, London, Ontario
Thesis title: “A novel design methodology accounting for ramping and field inhomogeneities in dreMR imaging”
Supervisor: Dr. Blaine A. Chronik
- Honours Bachelor of Science in Physics** Sept 2015 – Apr 2019
Honors Specialization in Physics, Minor in Advanced Physics, *with distinction, Gold Medal*
University of Western Ontario, London, Ontario
Thesis title: “Photoconductivity and memristive properties of oxoverdazyl radical memory devices”
Supervisor: Dr. Giovanni Fanchini

Awards and Honours:

- | | |
|--|-----------------------|
| NSERC Postgraduate Scholarship – Doctoral | Sept 2021 – Aug 2024 |
| Stanford Electrical Engineering Department Fellowship | Sept 2021 – June 2022 |
| ISMRRM Trainee Educational Stipend | May 2020 |
| NSERC Canada Graduate Scholarship – Master’s | Sept 2020 – Aug 2021 |
| Ontario Graduate Scholarship (Declined) | Sept 2020 – Aug 2021 |
| Western Graduate Research Scholarship | Sept 2019 – Aug 2021 |
| ISMRRM Trainee Educational Stipend | Aug 2020 |
| ISMRRM Magna Cum Laude Merit Award | Aug 2020 |
| Ontario Graduate Scholarship | Sept 2019 – Aug 2020 |
| The Raymond Compton Dearle Gold Medal | Jun 2019 |
| Donald R. Hay Prize | Jun 2019 |
| Dean’s List University of Western Ontario | Sept 2015 – Apr 2019 |
| S.R. Valluri Scholarship in Mathematical/Theoretical Physics | Oct 2018 |
| NSERC Undergraduate Student Research Award | May 2018 – Aug 2018 |
| UWO In-Course Scholarship Year III | Sept 2017 |
| NSERC Undergraduate Student Research Award | May 2017 – Aug 2017 |
| The Western Scholarship of Excellence | Sept 2015 |
| Bruce Power Post-Secondary Scholarship | Sept 2015 |

Publications

“Redox Polymers Incorporating Pendant 6-Oxoverdazyl and Nitronyl Nitroxide Radicals”

Michael Anghel, Francois Magnan, Sara D. Catigan, Matthew A. McCready, et al. Journal of Polymer Science, vol. 58, no. 2, Aug. 2020, pp. 309–319., doi:10.1002/pol.20190082.

Peer-reviewed Conference Abstracts

International Society of Magnetic Resonance in Medicine (Poster) 15 – 20 May 2020

Made virtual due to COVID-19

M.A. McCready, W.B. Handler, B.A. Chronik, “Measuring induced heating of low-field superconducting system during field-cycling pulse sequences”

International Society of Magnetic Resonance in Medicine (Poster) 15 – 20 May 2020

Made virtual due to COVID-19

M.A. McCready, W.B. Handler, F. Martinez-Santesteban, T.J. Scholl, B.A. Chronik, “Inhomogeneity and ramping effects in field-cycled quantitative molecular MRI”

Imaging Network Ontario Symposium (Power Pitch) 23 – 24 Mar 2021

Made virtual due to COVID-19

M.A. McCready, W.B. Handler, B.A. Chronik, “Inhomogeneity and ramping effects in delta relaxation enhanced magnetic resonance”

International Society of Magnetic Resonance in Medicine (Oral) 8 – 14 Aug 2020

International Convention Centre Sydney, Sydney, Australia. Made virtual due to COVID-19

M.A. McCready, W.B. Handler, B.A. Chronik, “Improving Homogeneity in Delta Relaxation Enhanced Magnetic Resonance Using Boundary Element Method”

Received *Magna Cum Laude Merit Award* for abstract

Imaging Network Ontario Symposium (Poster) 26 – 27 Mar 2020

Chestnut Residence & Conference Center, Toronto, Ontario. Made virtual due to COVID-19

M.A. McCready, W.B. Handler, B.A. Chronik, “An increased homogeneity design method for delta relaxation enhanced magnetic resonance systems”

LHSC Oncology Research and Education Day (Poster) 8 Jun 2018

Best Western Plus Lamplighter Inn & Conference Centre, London, Ontario

M.A. McCready, D. Goldman, N.E. Power, E. Wong, “Computer Simulation of Adaptive Metabolic Response to Anti-angiogenic Treatment in Renal Cell Carcinoma”

Other Conference Presentations

Physics Undergraduate Conference (Poster) 14 Mar 2019

Dept. of Physics and Astronomy, University of Western Ontario, London, Ontario

M.A. McCready, D. Singh, G. Fanchini, “Optoelectronic switchability in P6OV resistive memory devices”

Fallona Family Research Showcase (Poster)

12 Apr 2018

University of Western Ontario, London, Ontario

M.A. McCready, D. Goldman, N.E. Power, E. Wong, "Computer Simulation of Adaptive Metabolic Response to Anti-angiogenic Treatment in Renal Cell Carcinoma"

Teaching Assistant Experience**Introductory Physics II (Physics 1301/1401/1029)**

Jan 2021 – April 2021

*Dept. of Physics and Astronomy, University of Western Ontario, London, Ontario***Waves and Oscillations (Physics 2110)**

Sept 2020 – Dec 2020

*Dept. of Physics and Astronomy, University of Western Ontario, London, Ontario***Senior Physics Laboratory (Physics 3900)**

Jan 2020 – Apr 2020

*Dept. of Physics and Astronomy, University of Western Ontario, London, Ontario***Introductory Physics I (Physics 1301/1401)**

Sept 2019 – Dec 2019

*Dept. of Physics and Astronomy, University of Western Ontario, London, Ontario.***Research Experience:****xMR Research Laboratories – Blaine Chronik**

Sept 2019 – Aug 2021

*Dept. of Physics and Astronomy, University of Western Ontario, London, Ontario***Carbon-Based Nano-Optoelectronics Group – Giovanni Fanchini**

Sept 2018 – Apr 2019

*Dept. of Physics and Astronomy, University of Western Ontario, London, Ontario***xMR Research Laboratories – Blaine Chronik**

Jan 2018 – Aug 2018

*Dept. of Physics and Astronomy, University of Western Ontario, London, Ontario***Oncology Physics Lab – Eugene Wong**

May 2017 – Aug 2017

Dept. of Physics and Astronomy, University of Western Ontario, London, Ontario